

# **Simulating fully-integrated hydrological dynamics in complex Alpine headwaters**

Thornton, J.M.<sup>1</sup>, Therrien, R.<sup>2</sup>, Mariéthoz, G.<sup>3</sup>, Linde, N.<sup>4</sup> and Brunner, P.<sup>1</sup>

<sup>1</sup>Centre for Hydrogeology and Geothermics, University of Neuchâtel, Switzerland

<sup>2</sup>Department of Geology and Geological Engineering, University of Laval, Canada

<sup>3</sup>Institute of Earth Surface Dynamics, University of Lausanne, Switzerland

<sup>4</sup>Institute of Earth Sciences, University of Lausanne, Switzerland

This is a non-peer reviewed pre-print submitted to *EarthArXiv* on 26 February 2021.

The manuscript was submitted to *Water Resources Research* on 4 December 2020.

Corresponding author: J.M. Thornton ([james.thornton@unine.ch](mailto:james.thornton@unine.ch))

## **Key Points:**

- An integrated model of two adjacent steep, snow-dominated, geologically complex Alpine headwaters was developed and calibrated automatically
- Spatio-temporal dynamics and dependencies between snow, surface water, groundwater, and evapotranspiration processes are explicitly captured
- Such a simulation approach provides a basis for integrating novel datasets and generating more reliable climate change impact projections

1 **Abstract**

2 Hydrological climate change impact assessments in mountainous areas still frequently rely upon highly simplified  
3 approaches. Fully-integrated surface-subsurface codes would appear to hold far greater potential to represent the  
4 distinctive regimes of steep, geologically complex headwaters. However, their application in mountainous terrain has  
5 thus far been predominantly limited to crystalline catchments in western North America, leaving their utility in Alpine  
6 contexts untested. Here, a model of two adjacent calcareous Alpine headwaters is presented that accounts for 2D  
7 surface flow, 3D variably-saturated groundwater flow, and evapotranspiration. An energy balance-based  
8 representation of snow dynamics contributes high-resolution forcing data, whilst a sophisticated 3D geological model  
9 helped inform the subsurface structure. In the first known attempt to calibrate an integrated, catchment-scale model in  
10 mountainous terrain automatically, numerous uncertain parameters were estimated. The salient features of the  
11 hydrological regime were ultimately satisfactorily reproduced; over an independent 11-month evaluation period, a  
12 Nash-Sutcliffe efficiency of 0.73 was attained at the principal streamflow gauge. The visualization of forcings and  
13 simulated responses further confirmed the model's broad coherence. Closely replicating the somewhat contrasting  
14 groundwater level signatures observed in close proximity to one another was more elusive, presumably due to  
15 unresolved local subsurface heterogeneity. Finally, the impacts of various model simplifications on key predictions  
16 were assessed. Overall, our work demonstrates the feasibility and numerous attractions of applying integrated models  
17 – especially those that allow the stream network to evolve freely – in complex mountain systems, although certain  
18 outstanding challenges remain to be overcome if their global uptake is to increase.

19

20 **Key words:** *Alpine; integrated hydrological modelling; snow; geology; calibration; spatio-temporal*

21 **1. Introduction**

22 Mountainous water resources hold considerable societal importance (Immerzeel et al., 2020; Viviroli et al., 2020).  
23 However, in the European Alps as elsewhere, two key hydrological system components – namely the glaciers and  
24 snowpacks – are declining rapidly in the face of ongoing warming (Beniston et al., 2018). In light of these profound  
25 changes, reliable projections of Alpine hydrological systems are urgently required to implement sound mitigation and  
26 adaptation measures. Yet Alpine hydrological systems are extremely complex; considerable elevation gradients and  
27 rugged topography drive pronounced spatio-temporal variability in meteorological conditions, water stored in solid  
28 form is released on highly contrasting timescales, and inherently complex bedrock architectures can influence  
29 groundwater flow patterns and by extension broader hydrological system functioning (e.g. via subsurface flows across  
30 topographic divides). Furthermore, contemporaneous changes in other system components, including forests and  
31 permafrost, could modulate more direct, climate-driven hydrological changes (e.g. Evans et al., 2015). The notoriously  
32 limited quantity and spatial representativeness of environmental data that can typically be obtained in such  
33 environments presents further complications.

34  
35 Despite this high system complexity (but also perhaps partly because of limited data), most hydrological climate  
36 change impact assessments in mountainous areas continue to rely on “box-type” conceptual hydrological models (e.g.  
37 Jenicek et al., 2018; Wagner et al., 2017). Because the parameters of these models have very limited physical meaning,  
38 constraining them to plausible ranges is difficult. Consequently, whilst streamflows (which are traditionally the only  
39 data involved in calibration) can often be replicated well, care may be required when making interpretations or drawing  
40 inferences with respect to internal physical dynamics (e.g. Staudinger et al., 2017). Implicitly, this is precisely what  
41 is done when such tools are used in climate impact assessments. Indeed, such models are often especially challenged  
42 when the forcing conditions differ from those of the calibration period, as they likely would under such circumstances  
43 (Duethmann et al., 2020). In addition, when such models are only lumped or partially-distributed, distributed  
44 observations cannot be easily incorporated, nor the impacts of inherently spatial phenomena (e.g. vegetation change)  
45 considered (Speich et al., 2020). Finally, the suitability of the empirical, index-based snow modelling schemes that  
46 commonly feature in such models to reproduce complex Alpine snow dynamics is questionable (Warscher et al.,  
47 2013). Ultimately, the validity of resultant predictions may not be guaranteed.

48  
49 More physically-based approaches exist. For instance, WaSiM (Schulla, 2017), TOPKAPI-ETH (Ragetti et al., 2014),  
50 and WEB-DHM-S (Shrestha et al., 2015) were all developed specifically for mountainous applications. Generally,  
51 topography is discretized regularly and the 1D soil water balance solved independently for each cell before routing  
52 functions are applied to generate streamflow hydrographs at specified points along predefined stream networks.  
53 Advanced “full-physics”, multi-layer energy balance snowpack models – such as the semi-distributed (Hydrological  
54 Response Unit; HRU)-based Cold Regions Hydrology Model (CRHM) and the fully distributed Alpine3D (Lehning  
55 et al., 2006) – have also been extended to be able to generate streamflow estimates (e.g. DeBeer and Pomeroy, 2017;  
56 Brauchli et al., 2017). However, all of these more physically-based codes still rely on simple, non-mechanistic  
57 representations of groundwater storage and streamflow generation involving, for instance, lumped groundwater  
58 reservoirs (with either linear or non-linear storage-discharge relationships), and the neglect of lateral subsurface  
59 flows (Gallice et al., 2016; Fatichi et al., 2015). In these regards, they suffer many similar limitations as their simpler  
60 counterparts, leaving them no better placed to account for local geological influences; considerable mismatch certainly  
61 therefore exists between the sophistication of snow and (near) surface representation on the one hand, and the  
62 simplified representation of subsurface processes on the other. Whilst such simulation approaches may be appropriate  
63 in certain settings, for instance where soils are fairly homogenous, bedrock fairly homogenous or even impermeable,  
64 and few sizable permeable unconsolidated deposits present, elsewhere this may not be the case. It is also worth  
65 remarking that even highly advanced snow models like Alpine3D overlook some potentially important processes, such  
66 as the gravitational redistribution of snow from steep slopes (whose omission can produce undesirable artefacts in  
67 steep, rugged terrain; Freudiger et al., 2017), and – as with other distributed tools – are highly contingent upon the  
68 availability of good quality of meteorological forcing data (Förster et al., 2014).

69 In the broader literature, partial differential equation-based, spatially distributed, fully-integrated (or fully-coupled)  
70 surface-subsurface models are becoming increasingly popular, with reported applications now spanning a considerable  
71 range of environmental settings, research questions, and spatial scales (Ala-aho et al., 2015; Hwang et al., 2018; Jaros  
72 et al., 2019; Maxwell et al., 2015; Smerdon et al., 2007; Sulis et al., 2011; Tolley et al., 2019). Such codes are capable  
73 of mechanistically simulating most potentially relevant hydrological processes, including 2D surface flow, 3D  
74 variably-saturated groundwater flow, and evapotranspiration, in a physically-based, distributed, transient, and  
75 internally coherent fashion. Consequently, runoff generation can arise from any combination of possible mechanisms  
76 (infiltration or saturation excess, groundwater discharge), removing the need for the imposition of a strong prior  
77 conception. In contrast to traditional groundwater models, recharge is computed internally. Besides these generic  
78 benefits, several features of integrated models would appear to make them especially well-suited to the simulation of  
79 distinctive Alpine hydrological regimes.

80  
81 Firstly, they are capable of ingesting 3D information regarding the arrangement of subsurface formations, and so  
82 should enable any influence that complex Alpine geologies exert on broader catchment dynamics to be explicitly  
83 represented. Secondly, they can simultaneously account for surface water flows, which are important with respect to  
84 flood risk and sediment transport in steep terrain. Perhaps their greatest attraction, though, related to the free, bi-  
85 directional exchange between the surface and subsurface domains that they allow. In contrast to most hydrological  
86 models, require fixed stream locations to be defined *a priori*, some fully-integrated codes, such as HydroGeoSphere  
87 (HGS; Aquanty Inc., 2016), even allow the stream network to evolve dynamically in accordance with physical laws  
88 as a function of the boundary conditions and surface and subsurface properties prescribed. This is important because  
89 many headwater torrents and streams are intermittent (Durighetto et al., 2020; Van Meerveld et al., 2019) and/or  
90 demonstrate strong variability in “losing” and “gaining” patterns more broadly, with ecological (amongst other)  
91 implications. These integrated codes should therefore be well placed to replicate such dynamics.

92  
93 Some studies seeking to exploit contemporary numerical models in mountainous contexts – including some integrated  
94 ones – have begun to emerge. Thus far, efforts have predominantly been focused on catchments underlain by  
95 crystalline and other low permeability/storage bedrock types that are encountered widely across western North  
96 America, where high water-tables are relatively high. In an early contribution, Gleeson and Manning (2008) conducted  
97 a series of synthetic experiments using HGS to unravel the influence of topography and hydrogeological properties  
98 on regional (i.e. inter-watershed) three-dimensional (3D) groundwater flow in idealized crystalline mountainous  
99 terrain. Although completely understandable given their aims, a number of real-world complexities were neglected,  
100 including “evapotranspiration, the role of the orographic effects on precipitation, the seasonal effects of snow  
101 accumulation and melting, ...transient conditions, such as perched ground-water conditions...[and] the role of alpine  
102 glaciers or permeable surficial geology units” (Gleeson and Manning, 2008; p. 4).

103  
104 The first more detailed, distributed, catchment-scale representations of real mountain systems in which bedrock was  
105 not simply treated as impermeable emerged shortly thereafter: Huntington and Niswonger (2012) simulated the  
106 hydrology of three watersheds in the eastern Sierra Nevada, U.S., under future climate scenarios using GSFLOW  
107 (Markstrom et al., 2008), concluding that marked decreases in summertime stream discharge are likely. Voeckler et  
108 al. (2014) used MIKE SHE (Graham & Butts, 2005) to demonstrate that a reasonable proportion of annual precipitation  
109 in a small headwater catchment in British Columbia, Canada, recharged the bedrock aquifer, calling into question the  
110 then-prevailing assumption that deep groundwater is a negligible water budget component in crystalline mountain  
111 catchments. Note that GSFLOW and MIKE SHE provide loosely coupled representations of surface-subsurface flows  
112 in which information is passed iteratively between the domains, in contrast to a single set of combined equations being  
113 solved (as in “globally implicit” fully-integrated models; see Maxwell et al., 2014).

114  
115 Later, fully-integrated models were used to simulate a few 2D transects in hypothetical (Markovich et al. 2016) and  
116 real (Pribulick et al. 2016) mountain catchments. In the latter example, in the Upper Colorado River Basin, U.S., the  
117 simulated responses of each transect were also highly contrasting, highlighting that such transect simulations provide

118 little insight into dominant processes and/or changes at catchment scale. 3D integrated models of real mountain basins  
119 naturally account for spatial variability in catchment properties and processes more explicitly, and their more  
120 development and application is accelerating. Ala-aho et al. (2017) established a 3D fully-integrated HGS model to  
121 develop insights into the spatio-temporal contributions of groundwater to runoff generation in very small (3.2 km<sup>2</sup>)  
122 headwater in the Scottish Highlands. Penn et al. (2016) altered vegetation parameters in a ParFlow.CML model to  
123 assess the hydrological impacts of mountain pine beetle-induced tree mortality in another Coloradoan headwater –  
124 that of the Big Thompson River, while Carroll et al. (2019) developed a GSLOW model of the entire East River,  
125 Colorado, finding groundwater to be an important and stable contributor to mountain streamflow. Finally, Maina &  
126 Siirila-Woodburn (2020) investigated hydrological responses following fire dynamics in a Californian watershed  
127 spanning a considerable elevational range using ParFlow.CLM.

128  
129 Whilst these examples attest to much recent progress, the uptake of integrated models in mountainous areas elsewhere  
130 remains extremely limited, and their utility in steep, snow-dominated, geologically complex Alpine terrain is currently  
131 entirely untested. Being geologically younger and more widely sedimentary, the European Alps generally exhibit  
132 higher topographical, geological, and hydrological process complexity than mountainous basins of the Western U.S.  
133 and Canada. Simply whether integrated models can be successfully applied in Alpine systems remains unclear. Some  
134 of the assumptions used previously – either justified by the study sites' characteristics or simply expedient – may no  
135 longer hold. For instance, certain studies simply assumed bedrock to be impermeable (i.e. a no-flow boundary was  
136 imposed at its upper surface; Ala-aho et al., 2017; Camporese et al., 2019). Alternatively, single bedrock zones with  
137 homogeneous hydraulic conductivity (Markovich et al., 2016; Voeckler et al., 2014) or a few sub-parallel geological  
138 layers (Huntington & Niswonger, 2012) have been considered sufficient, although Engdahl and Maxwell (2015) did  
139 employ a fuller representation. Even where bedrock flow was permitted, domains were typically limited vertically to  
140 only a few tens of meters below the surface, potentially limiting groundwater circulation depth; although hydraulic  
141 conductivity may indeed decline strongly with depth in crystalline settings (Welch & Allen, 2014), field evidence for  
142 deep flows increasingly exists even here (Frisbee et al., 2017). In contrast, in calcareous parts of the Alps specifically,  
143 sequences of limestones, shales, and marls have been folded and faulted into complex arrangements. In these regions,  
144 groundwater flowpaths can be deep, with patterns strongly influenced aquifer-aquitard interface geometries besides  
145 topography (Thornton et al., 2018). Consequently, integrated models here should ideally be informed by 3D  
146 representations of structural geology. Datasets possessing the requisite attributes for hydrological/hydrogeological  
147 modelling have traditionally been severely lacking, but the situation is improving (e.g. Thornton et al., 2018).

148  
149 In addition, in contrast to the application of Ala-aho et al. (2017), for instance, in which the small catchment size made  
150 it appropriate to apply spatially uniform forcing, in moderately sized, extremely steep and rugged catchments, forcing  
151 datasets that are highly resolved in space and time (i.e. 10s – 100s of meters at most, depending on the domain area,  
152 and at an hourly time-step) would also ideally be applied. However, running complex integrated models with such  
153 highly resolved spatially distributed, transient boundary conditions remains unusual. As such, the potential benefit of  
154 applying highly temporally resolved forcings to such models remains largely unexplored. It is worth highlighting here  
155 that in contrast to other model classes, integrated codes generally lack convenient pre-processing routines to correct  
156 meteorological station data as necessary (e.g. for precipitation undercatch) and spatially interpolate it, whilst reanalysis  
157 products are generally too coarse and unreliable to be applied directly in small, rugged headwaters. Code limitations  
158 can also come into play; GSFLOW, for instance, runs exclusively on a daily time-step.

159  
160 As already mentioned, representing snow dynamics is another important task in such terrain, given the dominant  
161 influence that snow exerts on both annual Alpine streamflow and groundwater recharge. Specifically, accurate snow  
162 simulations are crucial if spatio-temporal patterns of meltwater arrival at the land surface are to be captured. However,  
163 limited and uncertain meteorological data and process variability and complexity constitute major impediments.  
164 Interestingly, despite being highly advanced in most regards, and perhaps belying their origins in the groundwater  
165 modelling community, integrated models generally offer only empirical snow melt approaches (with the exception of  
166 ParFlow.CLM which implements an energy-balance scheme). Voeckler et al. (2014), for example, as well as recent

167 applications in non-mountainous but snow-influenced settings (Cochand et al., 2019; Schilling, Park et al., 2019)  
168 involved temperature-index schemes, whilst Ala-aho et al. (2017) neglected snow processes altogether. No integrated  
169 surface-subsurface codes are known to incorporate snow redistribution processes. Far more so than with 3D geological  
170 modelling, intensive efforts are ongoing to ameliorate snow simulations, for example using physics-based, multi-  
171 layered snow models (Brauchli et al, 2017), more hybrid physical-empirical models conditioned on various snow  
172 observations (Thornton et al., under revision), and other similar efforts (e.g. Griessinger et al., 2019; Schattan et al.,  
173 2020). However, these advancements have yet to be combined with coupled or integrated descriptions of surface-  
174 subsurface flow dynamics.

175  
176 Lastly, integrated models are notoriously computationally intensive. Long runtimes (often days to weeks; Miller et al.  
177 2018) can confound formal automated calibration and uncertainty analyses, which require many forward iterations  
178 (von Gunten et al., 2014). Reflecting this, of all the mountainous integrated modelling studies discussed hitherto, only  
179 Ala-aho et al. (2017) attempted automated calibration, with others relying on – if anything – manual calibration and/or  
180 simple sensitivity analyses (see also Foster and Maxwell, 2019). Nonetheless, because “mountains do not give up their  
181 secrets easily” (Klemeš, 1990), the importance of calibration is arguably higher than elsewhere. Calibration can  
182 additionally provide opportunities for subsequent uncertainty analyses.

183  
184 In this context, with a view to evaluating the general utility of integrated flow models in complex Alpine settings, the  
185 present paper seeks to develop, calibrate, and apply a fully-integrated model of two steep, adjacent, snow-dominated,  
186 and geologically-complex Swiss headwaters. Given the study region’s characteristics, emphasis is placed on ensuring  
187 that the model structure employed is as suitable as possible. It this contains fewer simplifying assumptions than  
188 previous integrated mountain models. All of the aspects listed above that were omitted in the early synthetic study of  
189 Gleeson and Manning (2008) are now incorporated. More specifically, the following outstanding research questions  
190 are addressed:

- 191
- 192 1. How feasible is the development and application of integrated models in complex Alpine terrain in which  
193 structural simplifications are minimized?
  - 194 2. To what extent can such models be calibrated automatically using streamflow and groundwater level time-  
195 series?
  - 196 3. What does making subsequent structural simplifications reveal about the degree of model complexity  
197 required in such settings?

198 The simplifications referred to in the final question pertain to both subsurface representation and spatio-temporal  
199 forcing data resolution. Whilst commonly made in modelling mountainous catchment, their effects remain largely  
200 untested.

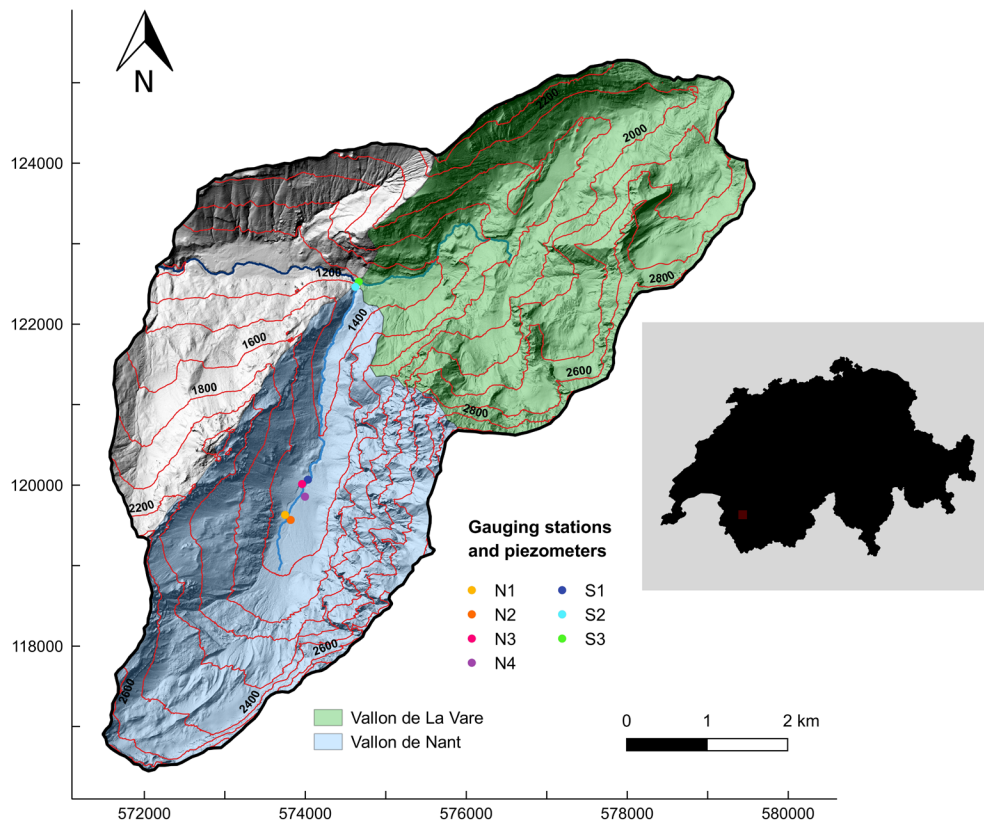
## 201 **2. Methods**

### 202 2.1. Study area and field instrumentation

203 The ~37 km<sup>2</sup> study area is centered upon two adjacent headwater catchments in the western Swiss Alps – the Vallon  
204 de Nant and the Vallon de La Vare (Figure 1; see also Thornton et al., under revision). Elevations range from 950 m  
205 to over 3,050 m a.s.l, slopes are steep, and the topography rugged. Land cover is varied; with increasing elevation,  
206 dense forest gives way to open alpine pastures and then sparsely vegetated regions of unconsolidated rock and bedrock  
207 outcrops/cliffs. Debris flows and avalanches occur frequently, especially in the upper parts. Aside from in the valley  
208 bottoms, soils are generally thin or non-existent, and small glaciers persist in the highest sheltered, north-facing  
209 sections. Permafrost mapping using the method of Deluigi et al. (2017) indicates that while some can be expected at  
210 the highest elevations – an assessment corroborated by a geophysical survey (Giaccone et al., 2019) – it is unlikely to  
211 be extensive. In places, various unconsolidated Quaternary sediments thought likely to function as aquifers overly the  
212 bedrock.

213 The area receives annual precipitation  $\geq 1400$  mm, approximately 40% of which falls as snow. Snowmelt dominates  
 214 total annual streamflow and also contributes significantly to groundwater recharge. Given the catchment's elevational  
 215 range, its hydrological regime will probably be highly sensitive to air temperature shifts. Intense convective storms in  
 216 summer are a further noteworthy feature of the region's meteorology. The surface hydrology of the Vallon de Nant is  
 217 characterized by numerous temporary torrents, whose discharge responds rapidly to rainfall and snowmelt. Streams  
 218 and other surface water features are less conspicuous in the upper part of the Vallon de La Vare, which is probably  
 219 explained by it having more permeable near-surface bedrock types. The area remains in a highly natural state, making  
 220 it rare in the context of the European Alps. Indeed, the Vallon de Nant has been a designated Natural Reserve since  
 221 1969. Whilst this is an attraction, the associated lack of long-term, systematic hydrometeorological observation and  
 222 severely restricted vehicular access represented daunting challenges to the development of our holistic, data-hungry  
 223 model.

224  
 225 Geologically, the region lies within the Nappe de Morcles; the lowest of a series of large nappe thrust folds that  
 226 together constitute the Helvetic Nappes. Alternating sequences of fairly permeable and – in places – probably  
 227 karstified limestones are interspersed with much lower permeability marls and shales (Badoux, 1971). These Mesozoic  
 228 sequences have been folded and faulted into complex arrangements by tectonic forces, such that the geometries of the  
 229 various (non-planar) aquifer-aquitard interfaces are expected to strongly influence groundwater flow patterns. As  
 230 alluded to above, the two sub-catchments actually lie within different zones of the first order fold structure. Thornton  
 231 et al. (2018) provide further information on the area's bedrock geology and known or hypothesized hydrological /  
 232 hydrogeological functioning, which helped inform the catchment delineation.



233  
 234  
 235 **Figure 1.** The study area and its situation within Switzerland. Stream discharge (S1-S3) and groundwater level (N1-  
 236 N4) measurement station locations are indicated. Elevation (in meters) is represented using contours, whilst the  
 237 background hillshade map provides an impression of the steepness and ruggedness of the surface topography.  
 238 Coordinates are in the projected CH1903 system (m).

239 Because some precipitation falling within the topographical catchment of the Vallon de Nant on the north-western  
240 ridge is known to drain north-westerly through the subsurface to a spring (Le Rippaz), thereby bypassing the gauging  
241 station S2, to prevent the possible introduction of spurious boundary effects, the model domain was extended  
242 downstream of the limits of the two gauged sub-basins (see also Ameli et al., 2018). Some incident precipitation on  
243 the eastern cliffs of the Vallon de Nant may be similarly transported south-easterly across the topographic divide and  
244 ultimately emerge several kilometers away at a spring near Saillon, in the Rhône Valley (see Figure S6). However,  
245 for practical reasons (model runtimes and data availability), the domain was not extended to encompass this entire  
246 area.

247  
248 The installation of a concrete weir downstream of Pont de Nant (S2 in Figure 1, see also Figure S1a) has placed a key  
249 role in opening up the area for quantitative hydrological investigations. Such gauging stations are rare on low-order  
250 Alpine streams, especially upstream of any anthropogenic influences. Automatic water level measurements were  
251 combined with a salt-dilution derived rating curve (Ceperley et al., 2018) to generate a fairly complete record of hourly  
252 discharge from April 2016 onwards. In addition to the “bypassing” mentioned above, substantial subsurface flow  
253 beneath gauging stations in some headwater streams can mean that measured surface streamflows do not represent  
254 total output fluxes across these section. However, this phenomenon understood to be insignificant here. (In any case,  
255 as an integrated model is used, observed streamflows can be compared with simulated surface fluxes). Shifting  
256 streambed configurations immediately upstream of the regular cross-section do however undermine the temporal  
257 consistency of the record somewhat, with potential biases and/or uncertainties afflicting estimates at both high and  
258 low flows. Stream water level measurements were also made at two additional locations, S1 and S3, but the resultant  
259 discharge series are not only shorter here but also more uncertain (due to lack of permanent, fixed cross-sections).  
260 None of the three streamflow gauging stations are situated at the outlet of the entire simulated domain; S1 is an internal  
261 site within the Vallon de Nant, whilst S2 is located further down L’Avançon de Nant, just above its confluence with  
262 Le Richard. The flow of Le Richard, which (at least partially) drains the Vallon de La Vare, is measured at S3.

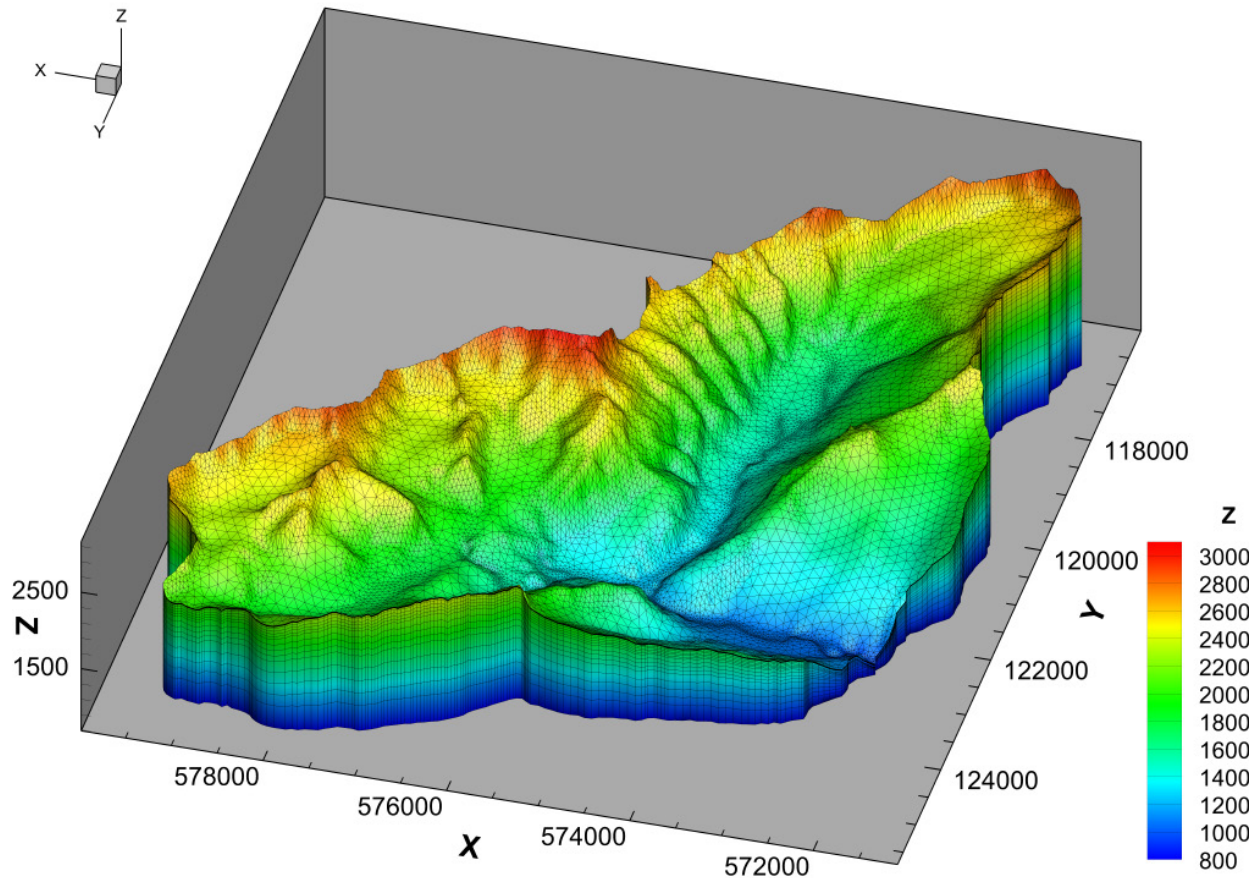
263  
264 To complement the stream discharge observations and provide some insight into internal hydrological processes, four  
265 small-diameter, relatively shallow (up to 6.5 m deep) groundwater piezometers (or observation wells) were installed  
266 in the vicinity of the large alluvial fan system in the central part of the Vallon de Nant (N1-N4 in Figure 1; see also  
267 Figure S1). The piezometers were screened over at least their lower halves, and were equipped with the pressure  
268 loggers in June 2017. They yield half-hourly observations, although at three of the four sites, groundwater levels fell  
269 below the piezometer base elevations for considerable periods.

## 270 2.2. Model setup

271 HGS (Aqunty Inc., 2016) is a fully-integrated simulator that simultaneously solves the diffusion wave approximation  
272 to the Saint-Venant equations for shallow 2D surface flow and a modified form of Richards’ equation for 3D variably-  
273 saturated subsurface flow. The coupling between these domains was conceptualized here using the first-order-  
274 exchange method (Ebel et al., 2009). Although some formations are expected to be karstified and soil macropores are  
275 also likely to be present, the subsurface was treated as an Equivalent Porous Media (EPM). As such, parameters must  
276 be considered effective at the elemental scale. Interception and evapotranspiration are simulated according to  
277 Kristensen and Jensen (1975) as a function of atmospheric demand (i.e. potential evapotranspiration;  $ET_p$ ), surface  
278 and near-surface moisture conditions, and vegetation properties. HGS was chosen over possible alternatives on  
279 account of its support for (partially, in this case) unstructured finite element meshes, which allow better representation  
280 of the study area’s complex topography and other physical features than regular discretisation scheme, as well as the  
281 freedom it permits with respect to the evolution of the stream network. The steps taken to define the model’s structure  
282 are described below.

## 283 1.2.1. Finite element mesh generation

284 A 2D triangular mesh was initially generated by employing the techniques of multi-level optimization and Delaunay  
 285 refinement in the Algomesh software (HydroAlgorithmics, 2016). Accounting for the extension described above, the  
 286 catchment boundary and theoretical stream poly-lines were generated via a terrain analysis. The swissALTI<sup>3D</sup> Digital  
 287 Terrain Model (DTM), which has a horizontal resolution of 2 m, was employed. These vectors represented the primary  
 288 constraints for the surface mesh generation. To capture the morphology of the incised mountain watercourses, nodes  
 289 were spaced at approximately 20-25 m intervals along the streamlines, with separation increasing with distance from  
 290 the riparian areas. The mesh was also refined in very steep areas. Nodes were placed at precisely the same locations  
 291 as the *in situ* observation points. To minimize any potential biases that can be induced in such terrain if low-order  
 292 streams and ridges are smoothed out (Wang et al., 2018), it was necessary that the resultant surface mesh (Figure S2)  
 293 be fairly finely resolved. It is comprised of 11,349 nodes (22,077 triangular elements). Surface node elevations were  
 294 then extracted directly from the DTM; the presence of topographically closed basins in the limestone landscape of the  
 295 Vallon de La Vare meant that usual terrain pre-processing steps (Käser et al., 2014) were unsuitable. Thereafter, the  
 296 mesh was extruded vertically in 23 layers, giving a 3D mesh comprised of 272,376 nodes (507,771 prismic elements)  
 297 (Figure 2). (Note: HGS automatically adds an extra node sheet at the surface under the “dual nodes” approach applied;  
 298 Aquanty Inc., 2016).  
 299



300  
 301  
 302 **Figure 2.** The partially-unstructured 3D prismic mesh. The Z-variable denotes elevation in meters above sea level  
 303 (a.s.l.). The surface mesh was locally refined close to the streams and in very steep areas. Discretization in the vertical  
 304 plane was finest near the surface and coarsened with depth. Coordinates are in the projected CH1903 system (m).  
 305

306 Vertical resolution was highest near the surface, with sheets created 0.25, 0.5, 1.0, 2.0, 4.0, and 6.0 m depths. This  
 307 approach sought to ensure that near-surface wetting / drying fronts could be captured, and that there were both layers

308 that coincided with the assumed soil thicknesses (see the next subsection) and nodes at approximately the same depths  
309 as the *in situ* groundwater pressure transducers. The next three layers were spaced at 5 m intervals, except within the  
310 major unconsolidated feature extents (see Supplementary Text S1); there, the lowermost of these three layers  
311 corresponds to the estimated feature bases (i.e. depth to bedrock in all apart from the Nant alluvial fan), with the  
312 remaining two layers “stretched” such that they were equally distributed between that and the 6.0 m layer. The spacing  
313 between the 14 remaining lower, sub-parallel layers at 20 m and increased with depth until the constant specified base  
314 elevation of 800 m a.s.l was reached. The decision to represent such an extensive vertical range and employ relatively  
315 high vertical resolution was driven by the nature of the regional geology (i.e. the folded and faulted sequences of  
316 hydraulically contrasting formations, including some thin layers); deep flowpaths are considered possible here.  
317 Although some loss of structural information is inevitable as the pre-existing spatially continuous 3D geological model  
318 is resampled or transferred onto the layered partially-unstructured mesh (again, see the next subsection), the relatively  
319 fine vertical resolution sought to minimize this. That said, some compromise was required to keep the computation  
320 demands manageable; before settling on the final mesh, several alternatives were developed and tested with a view to  
321 achieving an appropriate balance between the representation of physical features, good numerical convergence, and  
322 the total number of nodes/elements.

### 323 *1.2.1. Definition of surface and subsurface zones*

324 The overall intention was to constrain the model’s structure as tightly as possible before proceeding to consider certain  
325 associated parameter values. A land cover map developed from swisstopo data (see Figure S3) was used to define the  
326 surface and evapotranspiration zones (i.e. spatial regions assigned uniform parameter values). Because the resolution  
327 of the map exceeded that of the mesh, all faces were assigned to a distinct zone according to the dominant land cover  
328 class within each (Tables S1 and S2). A map of estimated permafrost extent in both consolidated and unconsolidated  
329 sediments developed using the methodology of Deluigi et al. (2017) was superimposed upon this classification (i.e.  
330 permafrost presence or absence was treated as a sub-category in the zonation scheme). Because permafrost presence  
331 in rock walls (i.e. consolidated sediments) depends strongly on air temperatures and can therefore generally be  
332 determined with high confidence, the underlying permafrost map represented it binarily. As predicting the spatial  
333 distribution of permafrost occurrence in unconsolidated sediments is much more demanding, permafrost occurrence in  
334 unconsolidated sediments was represented probabilistically. For the purposes of the model, only pixels with  
335 probabilities > 0.5 were treated as permafrost, however.

336  
337 Subsurface zones were defined according to three information sources. The first is a 3D model of bedrock geology  
338 that represents 18 distinct formations and their associated features like major faults and secondary folds (Thornton et  
339 al., 2018; Figure S4). Geological datasets with the requisite attributes for spatially explicit subsurface flow modelling  
340 have traditionally been severely lacking in the Alps, and it was unclear at the outset of that study whether developing  
341 such a representation would even be possible. This is now demonstrably the case in even the most complex Alpine  
342 settings, and more generally the potential that exists to augment the wealth of high-quality (if decades old) geological  
343 information that exists is high. To transfer the bedrock information on the mesh, identifiers of the geological formation  
344 present (see Table S3) at each element centroid were extracted. As with the land cover map and previously mentioned,  
345 some information loss during this process was inevitable.

346 Estimated volumes of five unconsolidated Quaternary features likely to host important aquifers constituted the second  
347 subsurface information source. A simple geomorphometrical method was applied, complemented in one formation –  
348 the main alluvial fan aquifer (Nant) – by inferences from geophysics (see Supplementary Text S1). The formation  
349 identifiers of any elements whose centroids fell within one of the five unconsolidated feature volumes were  
350 overwritten with those of the respective Quaternary formation (this reassignment being necessary because all elements  
351 were initially assigned an identifier from the bedrock model, the bedrock model being “filled” to the surface). Beyond  
352 the extents of these major unconsolidated formations where bedrock did also not outcrop according to surficial  
353 geological maps, a generic “moraine”/cover layer with an assumed thickness of 2 m was defined to represent the thin  
354 superficial hillslope cover present.

355 The third information source is a very simple assumed soil depth map (Figure S5) that was prepared in the absence of  
356 any more detailed information on the spatial distribution of soil depths and their associated textural or hydraulic  
357 properties – the existing “official” spatially distributed soil data (OFAG, 1980) being dated and of questionable  
358 suitability. Soils were considered to form a single, homogenous zone, and the same “overwriting” process as  
359 previously was applied attribute the appropriate elements. Whilst volumetrically the soil zone is very small compared  
360 to the unconsolidated and consolidated geological formations, being situated at the surface, in such simulations (as in  
361 reality), it is likely to exert a disproportionately strong hydrological influence (via its influence on the partitioning of  
362 incident liquid water into runoff and infiltration).

363 In total, 24 distinct subsurface zones were defined. The main remaining structural uncertainties relate to the soil and  
364 unconsolidated aquifer volumes.

### 365 1.2.3. Boundary conditions

366 Given the complexity and importance of snow processes at the steep and rugged study site, the representation of snow  
367 dynamics required careful consideration. Currently, HGS offers only a simple temperature-index snow module, and  
368 moreover provides no capabilities for pre-processing meteorological station data. Therefore, forcing datasets that were  
369 previously generated externally (but specifically with a view to being used in this model) were applied (Thornton et  
370 al., under revision). For the snow component, a spatially distributed energy balance-based model was used to derive  
371 hourly snowmelt inputs at 25 m resolution. The model additionally accounted for gravitational snow redistribution  
372 from steep slopes was established and several uncertain parameters were optimized with respect to two complementary  
373 types of snow observations – snow extent maps derived from Landsat 8 imagery, and reconstructed snow water  
374 equivalent (SWE) time-series at two station locations. Commensurate datasets pertaining to glacier melt, rain falling  
375 on snow / ice free surfaces, and  $ET_p$  (using the Penman-Monteith method) datasets were also produced (Thornton et  
376 al., under revision).

377 These datasets were compiled to produce gridded representations of i) “all liquid water arriving at the land surface”  
378 (i.e. snowmelt, ice melt, firn melt, and rain), and ii)  $ET_p$  over the period 1 October 2014 to 30 September 2019 (and  
379 therefore partially coinciding with the *in situ* streamflow and groundwater level data. They were additionally  
380 aggregated to daily and monthly values, enabling to be applied flexibly as “rain” and “potential evapotranspiration”  
381 boundary conditions respectively across these frequencies.

382 To allow water to leave the domain, a “critical depth” boundary condition was applied to all surface boundary nodes.  
383 This condition forces the flow depth at these locations to be equal to the critical depth, i.e. the depth at which for a  
384 given discharge, specific energy is minimal (Froude number = 1). The base and sides of the domain were treated as  
385 “no flow” boundaries (i.e. flow across these faces is assumed negligible).

### 386 1.2.4. Initialization

387 The initialization of catchment-scale integrated models can be time-consuming and challenging (Ajami et al., 2015).  
388 Beginning from a prescribed set of initial conditions, one must run the given model using either steady or recursive  
389 transient forcing data until a state of equilibrium (or “dynamic equilibrium”, in transient cases) is attained. Traditional  
390 options for the initial conditions are a water table that is coincident with the surface (a so-called “wet start”), a  
391 completely dry domain (a “dry start”), or a water table configured to some shallow but arbitrary constant depth beneath  
392 the surface (e.g. 1-5 m; Seck et al., 2015). In HGS, an initial water table surface can also be generated as a function  
393 of elevation, which theoretically enables concepts such as the Topographic Wetness Index (TWI; Beven & Kirkby,  
394 1979) to be applied. However, the annual mean water table distribution here was expected to take a complex form,  
395 being influenced not only by topography but also by geology. For example, unsaturated zones beneath mountain ridges  
396 may be thick. As such, one of the aforementioned approaches would likely have resulted in very lengthy simulation  
397 times being required to approach (dynamic) equilibrium.

398 A customized initial water table was therefore generated by interpolating, in 3D, surface coordinates ( $x,y,z$ ) sampled  
 399 along normally perennial streams, springs, and wetland locations (i.e. where the water table is at / near the surface). As  
 400 the hydrological regime under consideration here is highly transient, the model (with the initial parameter estimates)  
 401 was then initialized by applying the forcing data corresponding to the 2014/2015 hydrological year at monthly  
 402 frequency recursively. When the simulated surface water hydrographs and groundwater levels at the various  
 403 observation points ceased to demonstrate marked inter-annual trends, the process was considered complete.

### 404 2.3. Calibration strategy and historical runs

405 Many of the model's parameters are highly uncertain, at least at model elemental scales (if not more fundamentally),  
 406 with those relating to the inaccessible mountain subsurface being essentially unknown. Some form of calibration was  
 407 required. Whilst manual trial-and-error procedures are applied in the integrated modelling literature, this approach is  
 408 unobjective and would regardless have been confounded here by the large number of parameters involved (which is  
 409 itself a function of the complex geology and diverse land cover). An automated approach was therefore pursued.  
 410

411 Based on a combination of lithological descriptions (for the bedrock formations), relevant previous studies, and  
 412 informed judgement, an initial parameterization scheme was devised. A subset of parameters numbering 46 in total  
 413 were then identified as calibration targets (see Tables S1 to S3). The model was linked with PEST\_HP (v17) (Doherty,  
 414 2020) – a code-independent, gradient-based parameter estimation tool that employs the Levenberg-Marquardt (L-M)  
 415 algorithm to minimize an objective function (in a least-squares sense). As model outputs are generally non-linear with  
 416 respect to varied parameter values, calibration is an iterative process. Being a gradient-based method, the L-M  
 417 algorithm may converge to local minima. Nevertheless, its efficiency in terms of the total number of forward runs  
 418 required is a critical quality when seeking to optimize such computationally intensive models. For every PEST model  
 419 run (i.e. parameter set proposed), a “re-initialization period” beginning on 1 October 2014 (approximately 18 months  
 420 before the first available observations) was simulated to try to equilibrate the system state to the new parameters. All  
 421 available hourly (mean) streamflow measurements and half-hourly (instantaneous) groundwater level measurements  
 422 from 9 April 2016 (i.e. the start of measurements at S2) until 31 October 2017 contributed to the objective function.  
 423 As already highlighted, data coverage was not continuous throughout this period at all sites. Following a split-sample  
 424 strategy, the remaining observations (i.e. those from November 2017 to September 2018 inclusive) were retained for  
 425 independent evaluation.  
 426

427 The objective function (OF) developed is expressed in Eq. 1:  
 428

$$\begin{aligned}
 OF = & \sum_{i=1}^{20409} [wGWL(GWL_{sim} - GWL_{obs})^2] + \sum_{i=1}^{13184} [wQS_2(QS_{2sim} - QS_{2obs})^2] \\
 & + \sum_{i=1}^{60533} [wQS_{1,3}(QS_{1,3sim} - QS_{1,3obs})^2]
 \end{aligned}
 \tag{Eq. 1}$$

429  
 430 where  $wGWL$ ,  $wQS_2$ , and  $wQS_{1,3}$  are the relative weights that were assigned to each “observation group”, i.e. the  
 431 groundwater levels, the streamflows at S2, and the streamflows at S1 and S3, respectively. Here,  $wGWL = 0.38$ ,  
 432  $wQS_2 = 5.50 \times 10^{-5}$ , and  $wQS_{1,3} = 9.00 \times 10^{-5}$ .  $GWL_{sim}$  and  $GWL_{obs}$ ,  $QS_{2sim}$  and  $QS_{2obs}$ , and  $QS_{1,3sim}$  and  $QS_{1,3obs}$  are the  
 433 corresponding simulated and observed values at N1-4, S2, and S1 and S3, respectively.  
 434  
 435

436 Given the contrasting number, magnitudes, and units of observations within the different groups, as well as the  
 437 unknown degree of initial mismatch, the final observation weights could only be determined after running the model  
 438 once with the initial parameters. This was done with PEST's PWTADJ1 utility. Normally, the goal would be to  
 439 approximately equilibrate the contributions of the respective observation groups to the OF. However, whilst the

440 streamflow measurements (being spatially integrated) and groundwater level measurements (being spatially explicit)  
441 can generally be considered complementary (Paniconi & Putti, 2015), in complex unconsolidated settings such as  
442 those under consideration here, groundwater levels can be heavily influenced by extremely local phenomena. As such,  
443 it was realized that it would be essentially impossible for our model to reproduce the distinct groundwater responses  
444 that were observed within close proximity to one another without introducing sub-zone heterogeneity in material  
445 properties/parameters, which lay beyond the present scope. Therefore, to prevent the calibration process potentially  
446 magnifying this model deficiency, the groundwater levels were only assigned modest weights such that their combined  
447 contribution to the initial objective function was around 11%. In other words, most emphasis was placed on  
448 streamflows, whilst each observation group maintained at least some “visibility” to the process.  
449

450 As Ala-aho et al. (2017) also found, various model simplifications were found to be necessary to facilitate the  
451 automated calibration of the model. The first, that the re-initialization and calibration periods described above were  
452 relatively short, is not really a simplification, since the availability of the observational data and a desire to maintain  
453 an independent evaluation period dictated this. However, the feasibility of the calibration overall obviously increases  
454 as the length of the period that must be simulated iteratively (i.e. re-initialization plus calibration period) decreases.  
455 That said, given the pronounced seasonality of these catchments’ hydrological regimes, it was considered crucial that  
456 the calibration period exceeded one year.  
457

458 Runtimes were found to increase substantially with the temporal frequency at which the forcing data were applied.  
459 Therefore, in one major simplification, the calibration runs were undertaken using monthly frequency (but still  
460 distributed, 25 m) forcing data. Perhaps slightly surprisingly, the simulated seasonal dynamics are not extremely  
461 sensitive to whether monthly or daily forcings are applied (Figures S13 and S14), which provides some justification  
462 for this strategy. In another simplification aimed at reducing runtimes, the unsaturated zone (pressure head–saturation,  
463 and saturation–relative hydraulic conductivity) relationships for all subsurface zones, except the soil, were represented  
464 as tabular data with a small number of data points and made less non-linear. The poorly understood nature of these  
465 relationships in consolidated, potentially fractured, and/or karstified bedrock justifies this. For the soil, the van  
466 Genuchten parameters (van Genuchten, 1980) listed in Table 1 were applied. The slope term in the surface water flow  
467 equations was assumed equal to the topographic slope, and thereby also linearized, and the HGS model’s convergence  
468 criteria were relaxed for calibration (Newton absolute =  $1 \times 10^{-3}$  m, Newton residual = 500 m) before being re-tightened  
469 for the subsequent runs with optimized parameters (Newton absolute =  $1 \times 10^{-3}$  m, Newton residual = 150 m). The latter  
470 settings led to a mean mass balance error, expressed as a percentage of liquid water input, of  $\approx 5\%$ . Finally, the  
471 “coupling length” parameter for all surface zones except the streambed was set to a somewhat higher (and fixed) value  
472 (0.1 m) than ordinarily; values closer to zero are generally recommended to approximate the Continuity of Pressure  
473 (COP) approach, but typically increase runtimes (Liggett et al., 2012). Sensitivity tests revealed that model outputs of  
474 interest were not substantially affected by this choice. To mimic the enhanced surface–subsurface disconnection that  
475 the fine layer of silty streambed sediments that was often observed in the field could induce, the streambed zone  
476 coupling length was fixed to the higher value of 1.0 m.  
477

478 The calibration runs were carried out on a Windows machine (Intel(R) Xeon(R) CPU E-2699 v4 @ 2.20 GHz, 64.0  
479 GB RAM, 44 cores with 12 agents running in parallel, i.e. not using the entire resource). Each instance of HGS was  
480 also distributed across two cores. As a result of the process, the OF was reduced to 0.60 of its original value (although  
481 the degree of reduction obtained depends on the initial values selected). The optimized model was then run in two  
482 different configurations: i) for the full four-year simulation period with daily frequency forcing, and ii) for the final  
483 two-year period with hourly frequency forcing. The latter enabled the impact of forcing frequency on the simulated  
484 hydrological responses to be further investigated.  
485

## 486 2.4. Systematically simplifying the full model

487 Next, a series of sensitivity experiments were undertaken to assess the impacts that making various structural  
 488 simplifications – some of them common in the existing mountainous integrated modelling literature (e.g. due to lack  
 489 of data, or perhaps to reduce runtimes) – might have on key model predictions of interest in such terrain. To achieve  
 490 this, streamflow and groundwater level outputs generated in these experiments are considered with respect to those  
 491 generated by the “full complexity” model described above. The key characteristics of each configuration are listed  
 492 below.

493  
 494 *Scenario A. Subsurface entirely impermeable, no ET:* This extremely simple scenario assumes that the subsurface is  
 495 entirely impermeable (i.e. no infiltration or groundwater processes can occur), and that no water is returned to the  
 496 atmosphere via *ET*. As such, all incident liquid water at the land surface (i.e. rainfall + snowmelt + ice melt) directly  
 497 flows freely over the surface according to the discretized topography and surface parameters.

498  
 499 *Scenario B. Limited (30 m) vertical extent:* This scenario involves running the full integrated surface-subsurface model  
 500 (with *ET*) but limiting the vertical extent (or watershed “thickness”) to a uniform 30 m below the surface. As explained  
 501 in the Introduction, such a setup is presently fairly common (e.g. Foster & Maxwell, 2019), although the impacts on  
 502 simulated hydrological dynamics remain unclear (Condon et al., 2020).

503  
 504 *Scenario C. Spatially uniform forcing:* Catchment-scale integrated models are sometimes forced with spatially-  
 505 uniform (i.e. catchment-averaged) meteorological boundary conditions (e.g. Ala-aho et al., 2017). This could be  
 506 because distributed meteorological/snowmelt data are unavailable, in which case measurements made at a single  
 507 meteorological station within or near a given study catchment may be considered representative of conditions across  
 508 it. Alternatively, a given catchment may only correspond to a single downscaled pixel of reanalysis products (which  
 509 must often be relied up in the absence of *in situ* data) or climate model projections. Clearly, in very small and/or fairly  
 510 flat catchments, these approaches are likely to work well. In larger and more topographically complex mountain  
 511 headwaters catchments such as those under consideration here, it could be instructive to elucidate the impacts of such  
 512 an assumption. Thus, for this scenario, the distributed (25 m resolution) forcing datasets at daily frequency used to  
 513 force the “full complexity” integrated model were averaged across the two sub-catchments at each time-step before  
 514 being applied.

515  
 516 *Scenario D. No permafrost:* Finally, a “no permafrost” simulation was undertaken in which the coupling length  
 517 parameter in permafrost areas was set back from 50 m to the value of 0.1 m assigned elsewhere.

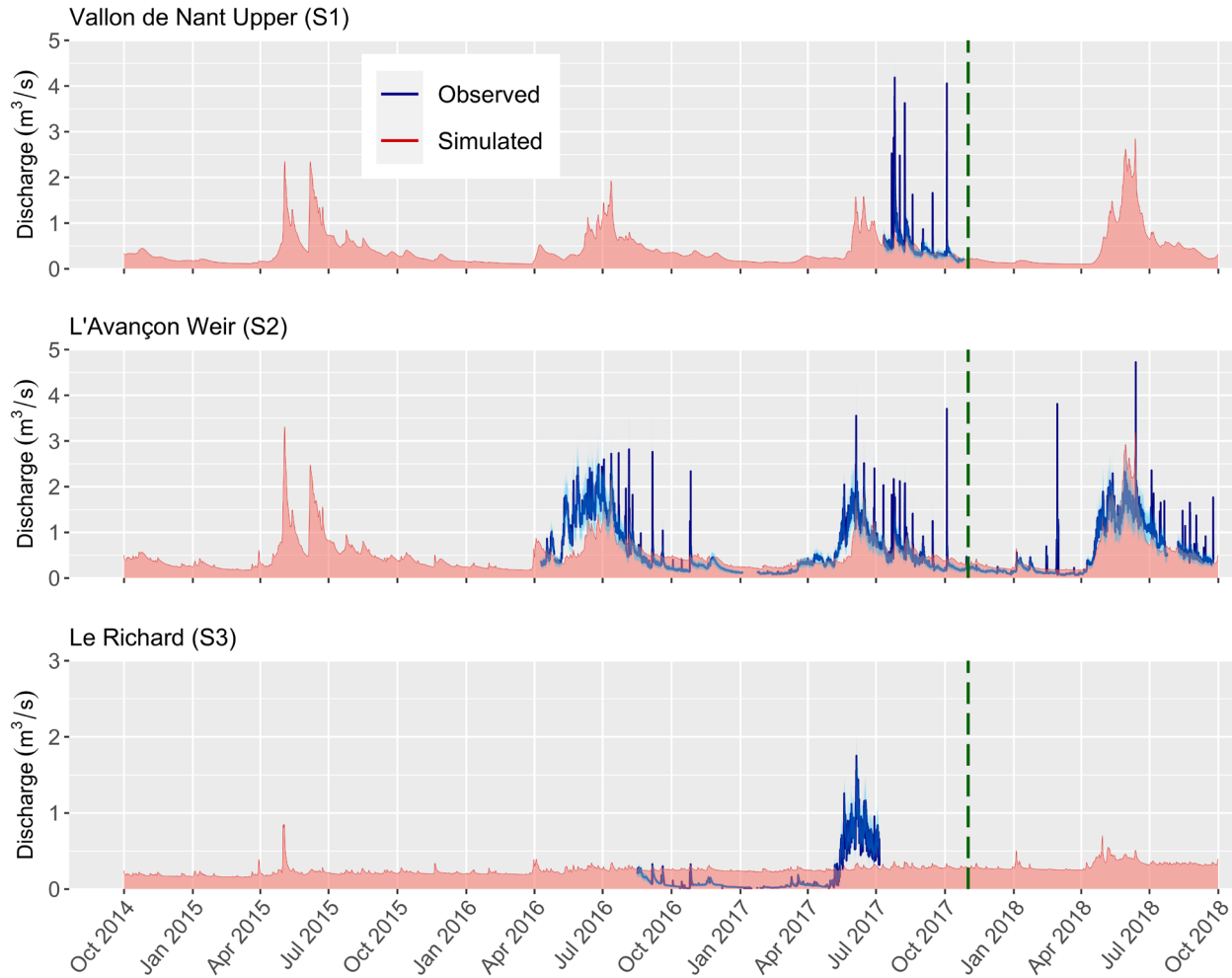
518  
 519 Each of these simplified models were derived from the calibrated “full complexity” version and forced with daily  
 520 frequency data. As such, comparing these outputs with those presented in Section 3.1.1 is apposite.

## 521 3. Results

### 522 3.1. Full complexity integrated model

#### 523 3.1.1. Daily frequency forcing

524 Streamflow and groundwater level time-series simulated by the calibrated, “full complexity” integrated model using  
 525 daily forcing data (as opposed to the monthly data used for calibration) above are plotted against the corresponding  
 526 observations in Figures 3 and 4.



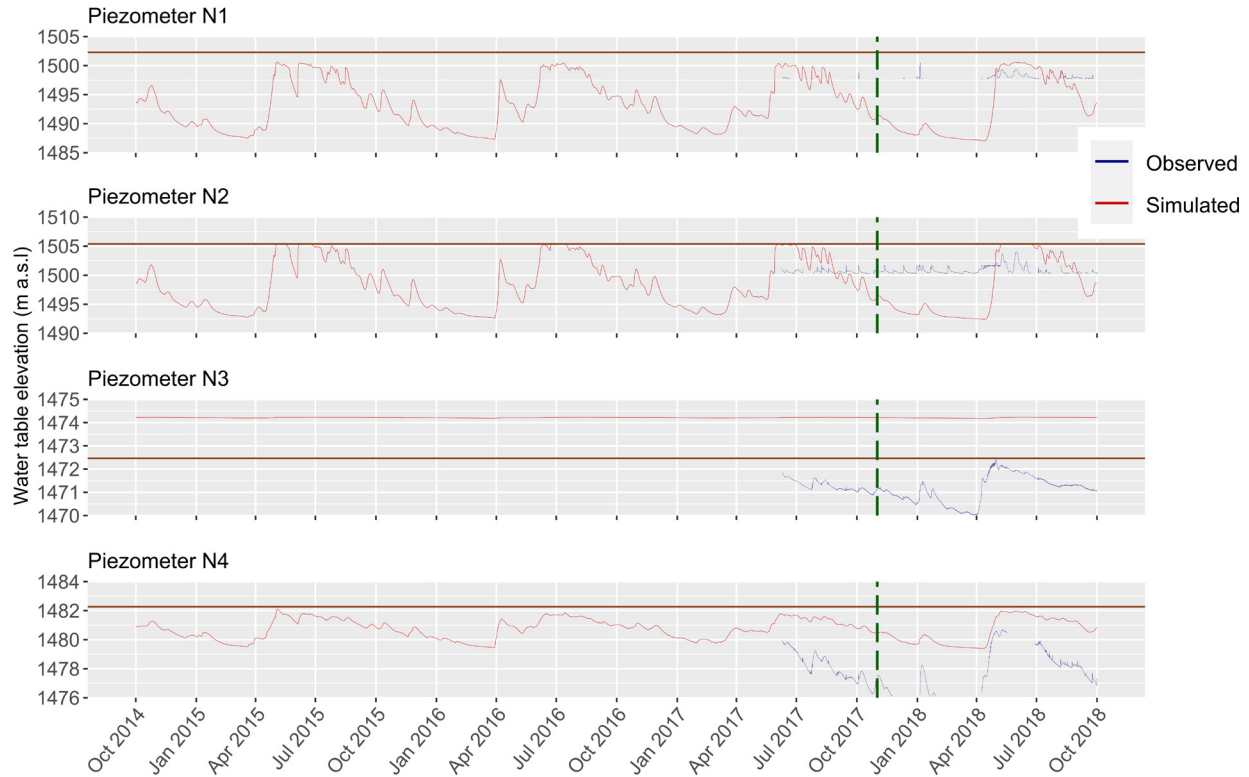
527  
528

**Figure 3.** Streamflows simulated by the fully-integrated model using daily frequency, 25 m resolution forcing data at the three gauging station locations vs. observations over the period 1 October 2014 – 1 October 2018. The dashed green line distinguishes the calibration (left) and evaluation (right) periods. Note: the observed data in this figure retain their original, hourly frequency. Estimated uncertainty in the observed streamflow data is represented by a shaded region (light blue) corresponding to  $\sim\pm 30\%$ .

534

535 The seasonality of streamflow is reproduced reasonably well at S1 and S2. Because daily frequency forcing data were  
536 applied, it is not necessarily unexpected that the sharp observed peaks could not be reproduced (these having been  
537 plotted at their underlying frequency). At S2, which has the most extensive observed record, the general annual water  
538 balance seems to have been well captured, though the onset of high spring flows is delayed in the model with respect  
539 to observations in 2016 and, to a lesser extent, 2017. S2 baseflow also seems slightly overestimated, though uncertainty  
540 in baseflow observations is also a consideration. At S1, the higher station in the Vallon de Nant, any such  
541 underestimation is much less evident (if present at all), at least based on the reduced observations here. For the main  
542 snowmelt-spring driven peak, the fit achieved at S2 over the independent evaluation period (i.e. November 2017 –  
543 September 2018 inclusive; to the right of the green dashed line) is very good, even if the preceding baseflows remain  
544 marginally overestimated. The simulation at S3 is poor, bearing little resemblance to the observations. The simulated  
545 series is too constant in comparison to the more dynamic (if short) observational record. Interestingly, the seemingly  
546 rapid observed streamflow response at S3 occurs despite the bedrock formations in Vallon de La Vare being  
547 considered relatively permeable.

548



549  
 550 **Figure 4.** Groundwater levels simulated by the fully-integrated model using daily frequency, 25 m resolution forcing  
 551 data at the four piezometer locations vs. observations over the period 1 October 2014 – 1 October 2018. The horizontal  
 552 brown line corresponds to the surface elevation. The dashed green line distinguishes the calibration (left) and  
 553 evaluation (right) periods. Note: the observations in this figure retain their original, half-hourly frequency.  
 554

555 Figure 4, which shows groundwater levels, again reveals a strong seasonal signal in the simulations comprised of a  
 556 peak associated with snowmelt followed by a more gradual decline. In this sense, the observed trends at N4, which  
 557 could perhaps be considered the most representative site, if not the precise levels themselves, are generally well  
 558 captured. Again, whilst rainfall-related peaks are superimposed upon the recession in the observations (at N4 in  
 559 particular), one would not necessarily expect these to be reproduced at this stage (i.e. using the daily forcing  
 560 frequency).  
 561

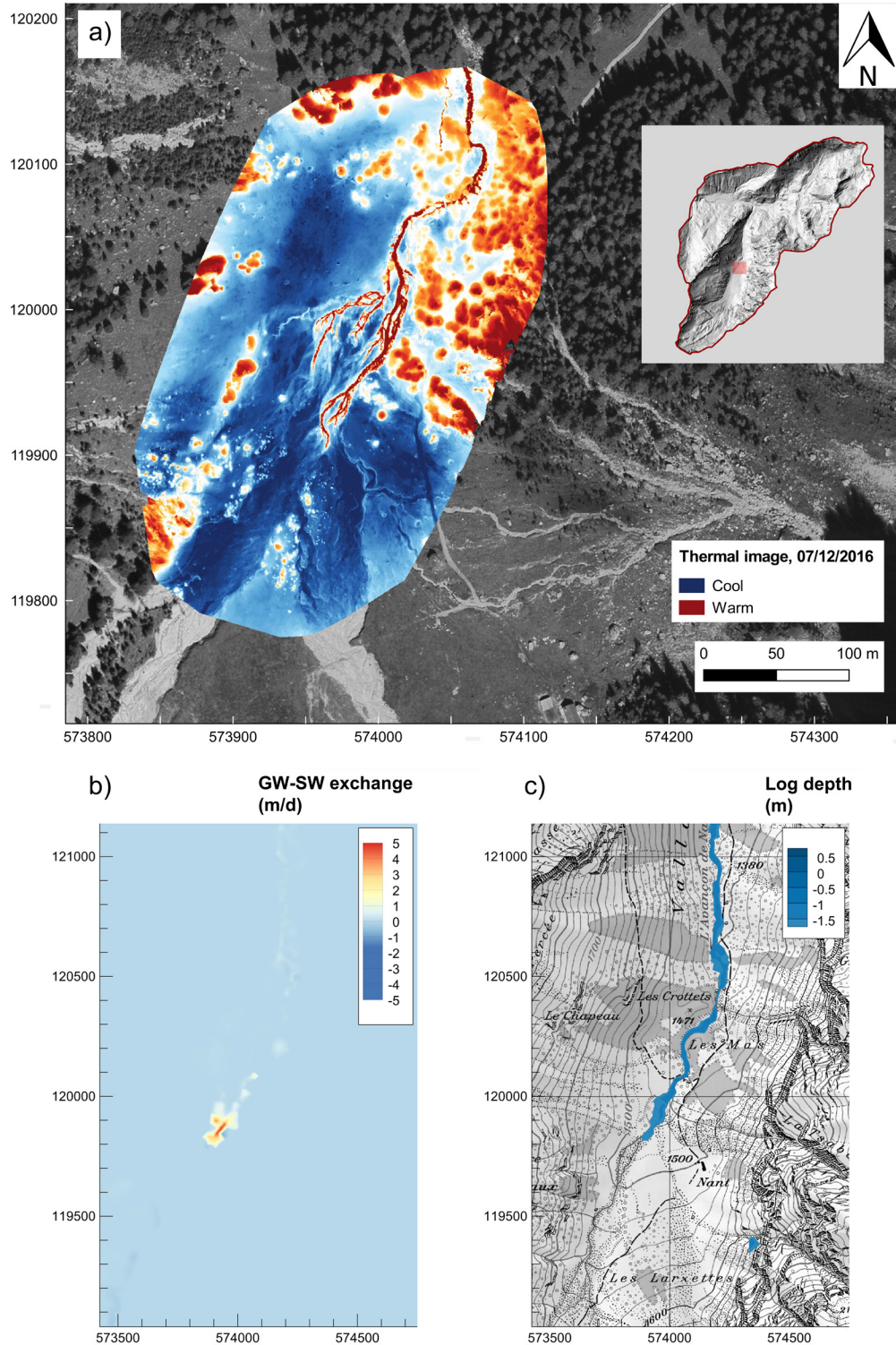
562 These plots show clearly the point raised in Section 2.3; that although the groundwater observation sites are situated  
 563 fairly close to one another within a very small part of the entire domain, the exhibit quite contrasting dynamics. In  
 564 contrast, with the exception of N3, the simulated dynamics are more similar between sites. The simulations at the  
 565 higher elevation sites, N1 and N2, demonstrate slightly more variability. The distinctive signals at N2, and to a lesser  
 566 extent, N1, could not be well reproduced. That said, the pairwise plot presented in Figure S7 suggests that overall  
 567 water table elevations across the alluvial fan zone are reasonably well approximated.  
 568

569 One key benefit of comprehensive integrated models is that comparisons and diagnostics are not limited to time-series  
 570 or scatterplots at observation points. Rather, spatio-temporal patterns in forcing data and numerous simulated internal  
 571 state variables responses (pertaining to the surface, subsurface, and evapotranspiration “domains”) can be visualized  
 572 and/or extracted arbitrarily. This capability conveys the powerful capabilities of such a simulation approach, and  
 573 enables the coherency of the numerical representation to be assessed intuitively. It moreover provides considerable  
 574 scope for a variety of datasets with complementary characteristics (e.g. spatially distributed vs. integrated, quantitative  
 575 vs. “soft”) to be introduced into their calibration and/or evaluation. Here, three examples are provided that illustrate  
 576 some of these possibilities.

577 A thermal image of the central part of the Vallon de Nant captured using a drone early on 7 December 2016 is  
578 considered first. No precipitation had fallen in the preceding 10 days, and – unusually for the time of year – the ground  
579 remained snow free. As such, all water in the channel could be confidently (and exclusively) identified as emergent  
580 groundwater. Because groundwater is several degrees warmer than the dry land surface under these circumstances  
581 (i.e. early morning in winter), the region of groundwater exfiltration from the streambed into the channel can be clearly  
582 identified (Figure 5a). A direct comparison can thus be made with i) the simulated spatial pattern exchange flux, and  
583 ii) the simulated spatial pattern of surface water presence in the same area on the same date (Figures 5b and c). One  
584 observes that groundwater emerges approximately the same location in the model as in reality. Moreover, surface  
585 water is present from this point downstream in the simulation, which is again consistent with the data (since the  
586 discrete “warm” region continues downstream in the thermal image).

587  
588 Secondly, Movie S1 (see Supporting Information) shows the spatio-temporal variability of the model’s meteorological  
589 boundary conditions (i.e. “all liquid water” and potential evapotranspiration) alongside the simulated response of two  
590 important variables – surface water depth and actual evapotranspiration ( $ET_a$ ) – over the hydrological year 2017/2018.  
591 During the first period, dynamics are subdued as the catchment gradually drains. As snowmelt onset occurs at  
592 progressively higher locations, the surface water network begins to expand. A strong elevation (i.e. temperature) effect  
593 is visible in both prescribed  $ET_p$  and simulated  $ET_a$ . Some surface water bodies do still form in areas of the Vallon de  
594 Le Vare, including at the location of a high elevation lake/wetland (578653, 123594).

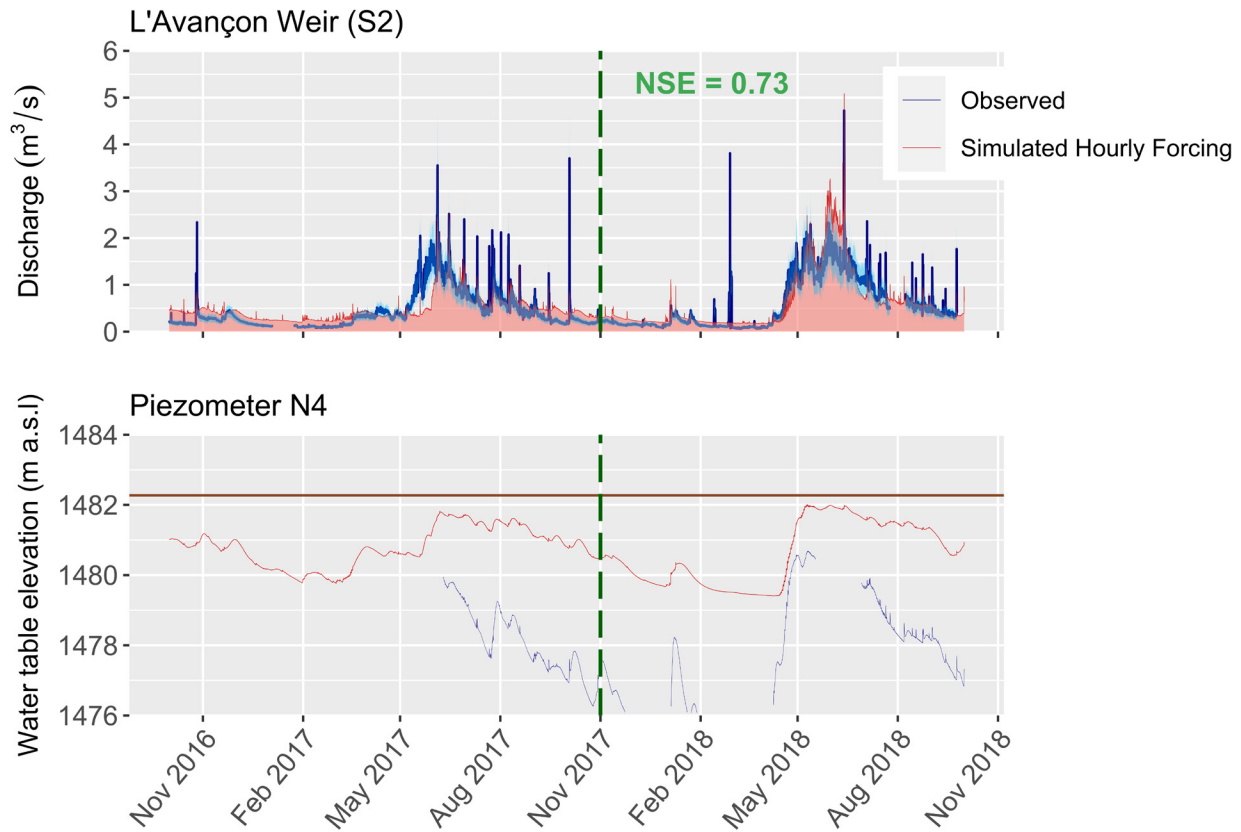
595  
596 Finally, Movie S2 shows the interplay between simulated saturation, both at the surface and (using slices) at depth  
597 and the simulated surface water level response at S2. Throughout the snowmelt period, the near-surface saturation  
598 levels gradually increase, followed by the arrival of the annual peak in simulated water level. This animation also  
599 clearly shows that the water table is generally lower in the Vallon de La Vare than the Vallon de Nant, and so this  
600 could provide an indication of an aspect to focus on in future to improve the time-series fit at S3. Lastly, the shallow  
601 simulated (and indeed observed) surface water depths at S2 highlight that even under the present climate, this system  
602 – presumably like many other small Alpine headwaters – lies fairly close to the “wet-dry limit”.



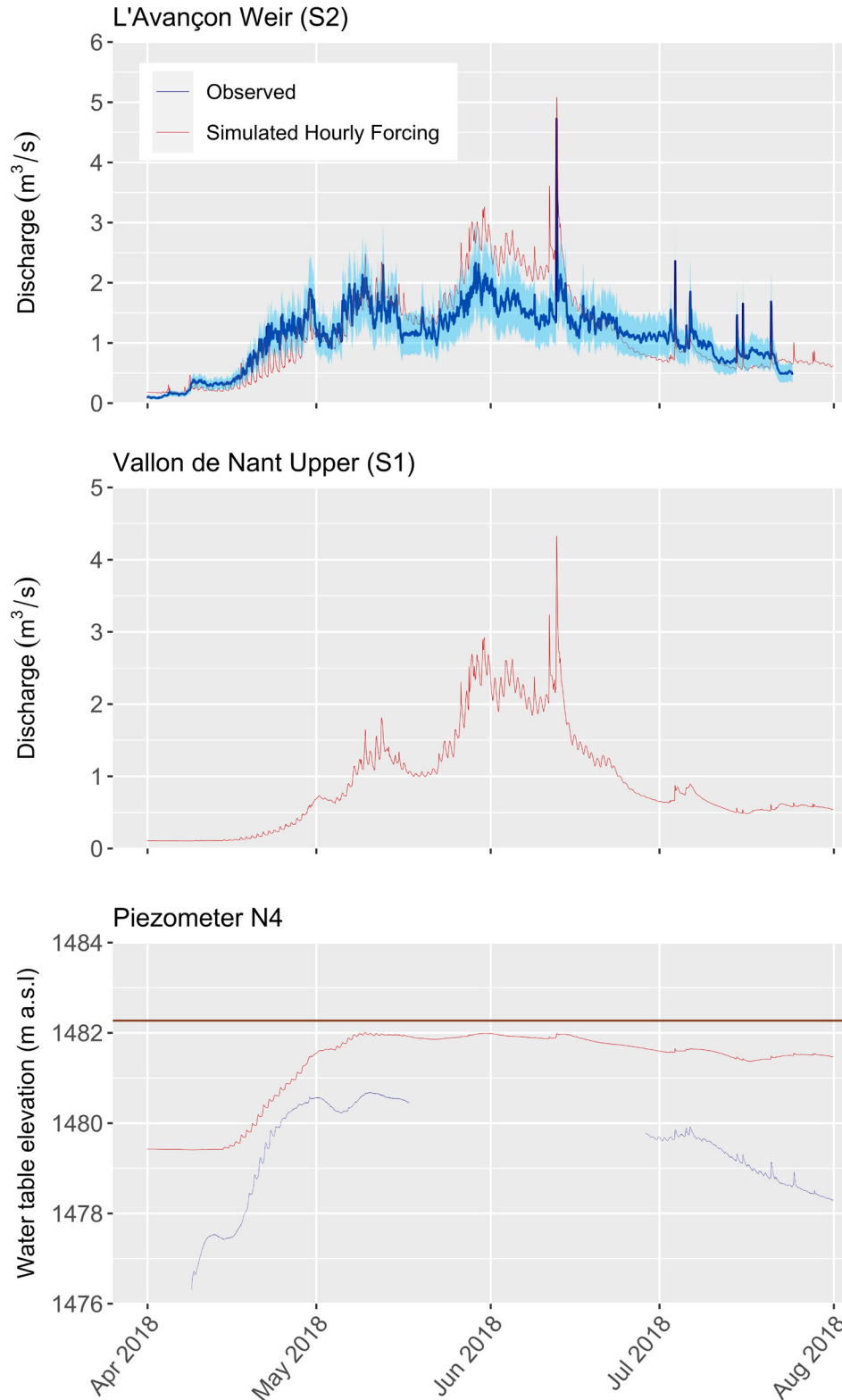
603  
 604 **Figure 5.** Spatial pattern of: a) Relative surface temperature in the distal part of the Nant alluvial fan on 7 December  
 605 2016 from which “observed” subsurface-surface exchange flux and surface water presence were inferred. Note that  
 606 the stream appears warmer than the surroundings. Red circular patterns correspond to trees that appear warmer because  
 607 of solar illumination at this moment. b) Subsurface-surface exchange flux simulated by the model (positive values  
 608 correspond to surface water exfiltration, and c) Simulated surface water presence, indicated by the simulated surface  
 609 water depth (both on the same date). Note that the footprint of map a) is different to that of b) and c).

610 3.1.2. Hourly frequency forcing

611 Figure 6 presents streamflow and groundwater level results simulated by the calibrated integrated model forced with  
 612 hourly frequency data over the period of 1 October 2016 – 1 October 2018 at S2 and N4, respectively. Figure 7,  
 613 meanwhile, focuses more closely on streamflow at S1 and S2 over the shorter period of spring and summer 2018. The  
 614 generally good streamflow correspondence obtained with the daily forcing data is maintained with hourly forcing data.  
 615 Indeed, with the hourly data, a Nash-Sutcliffe Efficiency (NSE) coefficient of 0.73 was attained over the independent  
 616 evaluation period, denoting good performance. Sharp flow peaks associated with convective thunderstorms are  
 617 represented slightly better than in the daily case (in which the quantities are distributed evenly over 24-hour periods).  
 618 That said, they are still generally insufficiently accentuated compared with the observations. Figure 7 also illustrates  
 619 that at this forcing frequency, diurnal variations in both streamflow and groundwater levels associated with spring  
 620 snowmelt (and potentially also ice melt and evapotranspiration) can be reproduced.  
 621



622  
 623  
 624 **Figure 6.** Streamflow and groundwater levels simulated by the fully-integrated model using hourly frequency, 25 m  
 625 resolution forcing at S2 and N4, respectively, vs. observations over the period 1 October 2016 – 1 October 2018. Note  
 626 that the observations retain their original frequency. Again, estimated uncertainty in the observed streamflow data is  
 627 represented by a shaded region (light blue) corresponding to  $\sim\pm 30\%$ , and the dashed green lines separate the calibration  
 628 and evaluation periods.  
 629

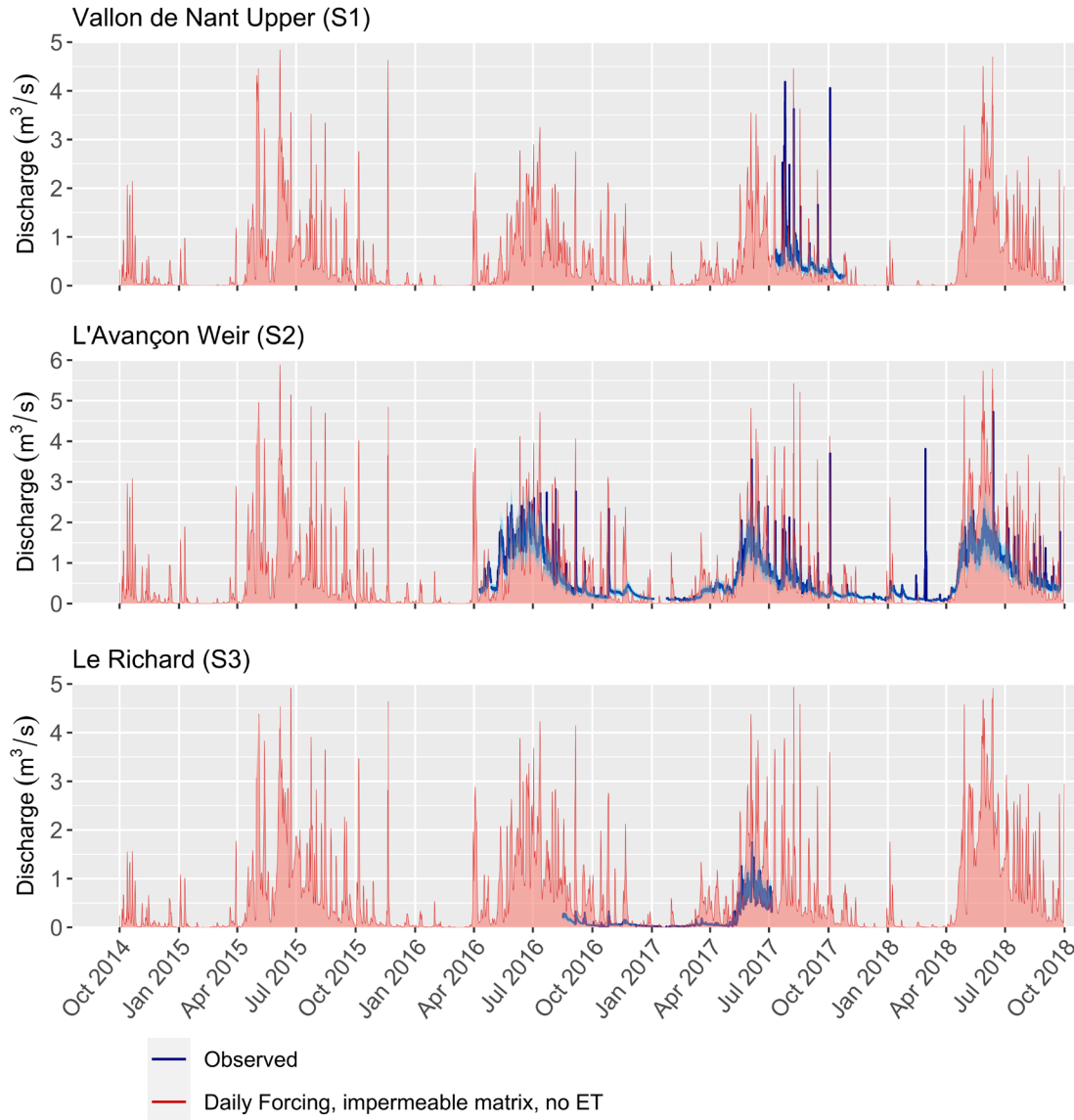


630  
 631 **Figure 7.** Streamflow and groundwater levels simulated by the fully-integrated model using hourly frequency forcing  
 632 at S2, S1, and N4, respectively, vs. observations over the period 1 October 2016 – 1 October 2018. Note that the  
 633 observations retain their original frequency. Estimated uncertainty in the observed streamflow data is represented by  
 634 a shaded region (light blue) corresponding to  $\sim\pm 30\%$ .

635 3.2. Systematically simplified versions

636 3.2.1. Scenario A: Impermeable matrix, no evapotranspiration (daily forcing)

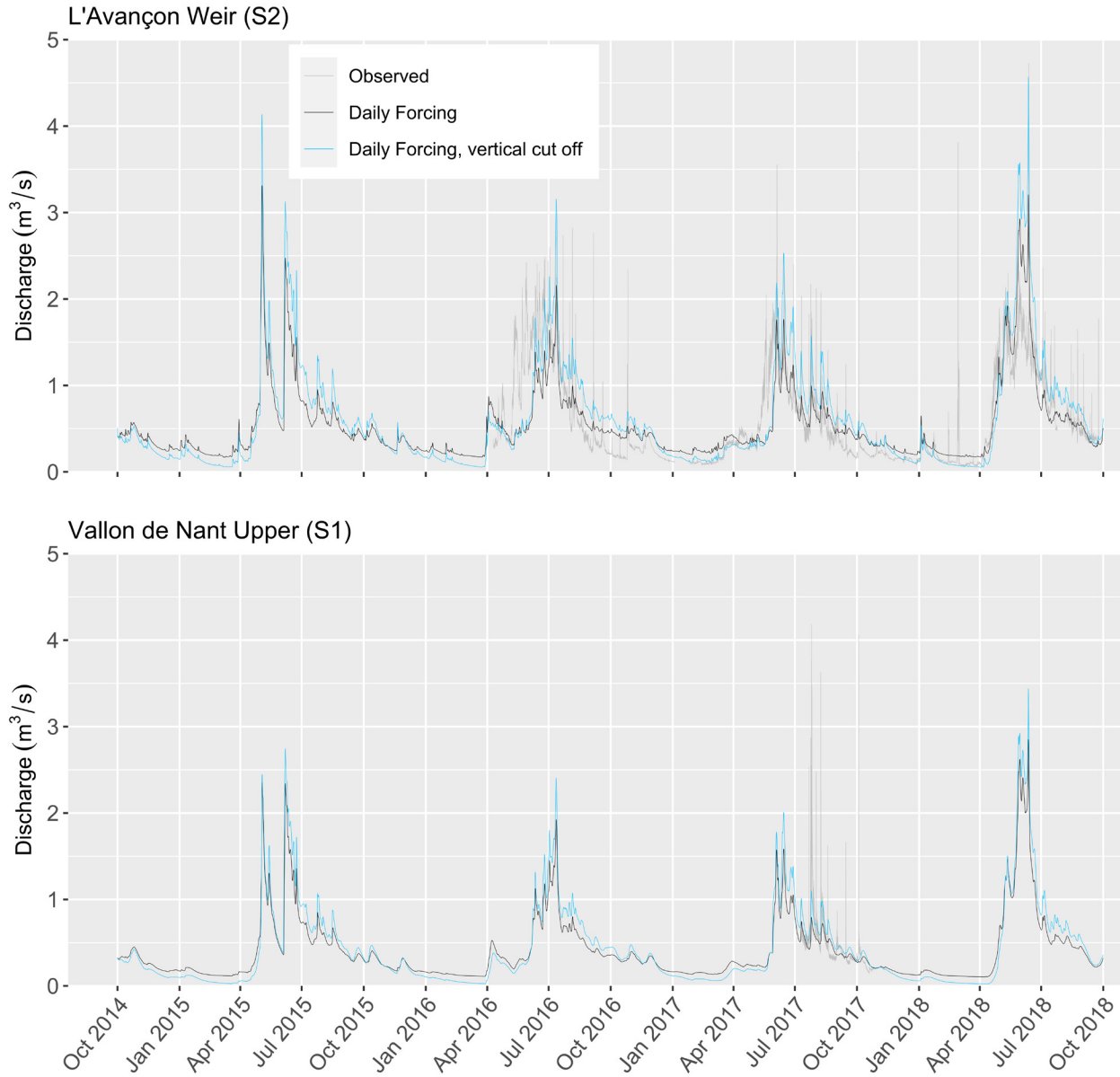
637 Figure 8 presents streamflows simulated under the “impermeable matrix” assumption (with *ET* also deactivated), using  
 638 daily frequency forcing. The correspondence between the simulated and observed peaks – both in terms of timing and  
 639 general flow magnitudes – is good, which provides further reassurance that the previously generated gridded liquid  
 640 water inputs (Thornton et al., under revision) are reasonable. Of course, under this assumption, there is  
 641 under/overestimation with respect to the observations, but the temporal pattern in these deviations agree well with  
 642 expectations. Overall, a degree of “overestimation” these simulated streamflows relative to observations does seem  
 643 apparent, especially at S3. Unsurprisingly, the spatial outputs (not shown) revealed that with this configuration, a  
 644 substantial lake forms in La Varre (~576859,123516).  
 645



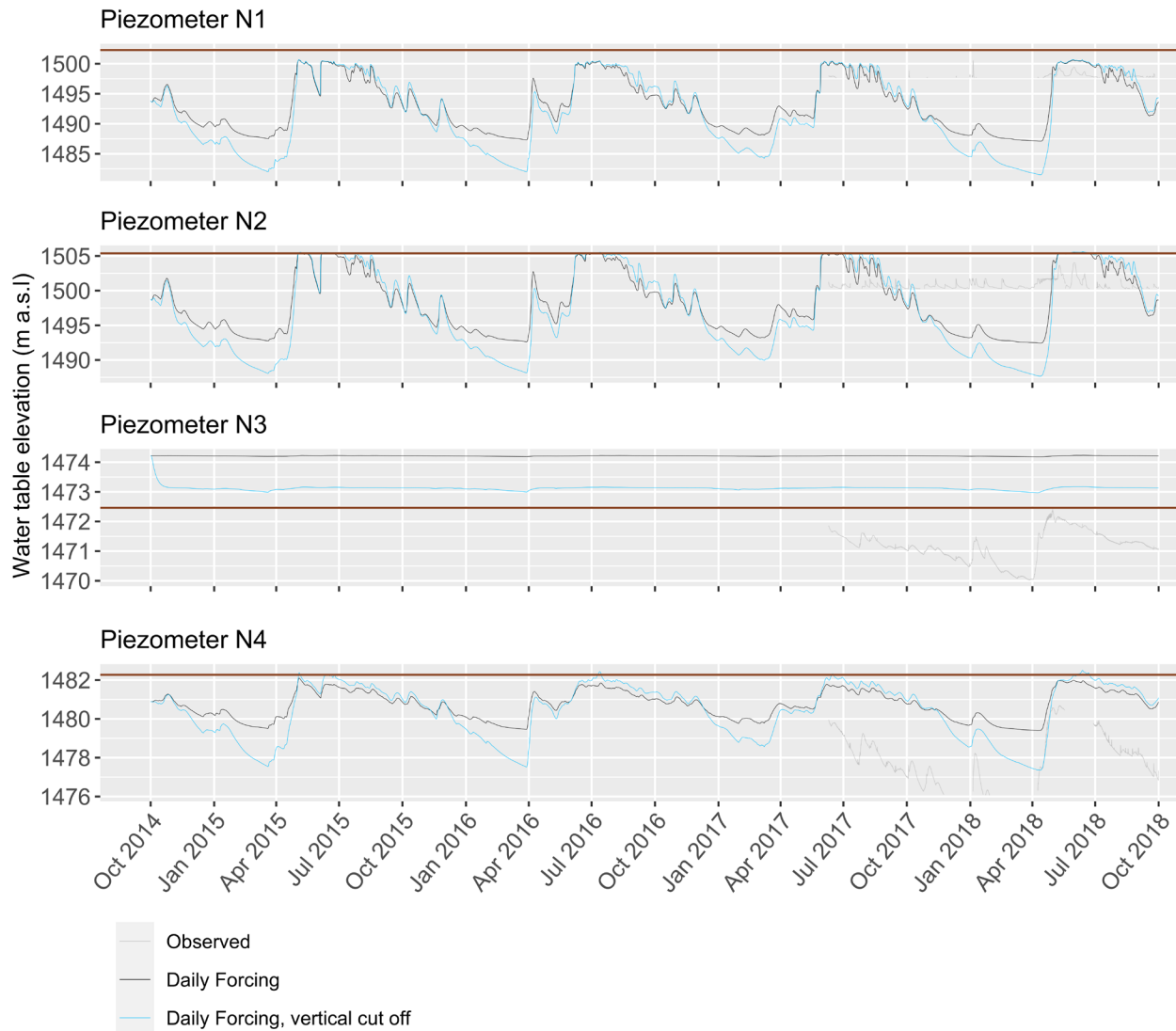
646 **Figure 8.** Simulated streamflow at each of the three gauging stations over the four-year historical period under an  
 647 “impermeable matrix”, i.e. “surface only” assumption, with subsurface flow and evapotranspiration (*ET*) deactivated.  
 648 In this case, the forcing data were applied at daily frequency. Estimated uncertainty in the observed data is represented  
 649 by a shaded region (light blue) corresponding to  $\pm 30\%$ .  
 650

651 3.2.2. Scenario B: Limited (30 m) vertical extent

652 In Figures 9 and 10, the effect of limiting the vertical extent upon predictions of streamflow and groundwater levels,  
 653 respectively, is illustrated. Under this assumption, peak flows are accentuated appreciably while baseflows are reduced  
 654 compared with the baseline simulation with full vertical extent (i.e. the regime becomes “flashier”). Annual peak  
 655 groundwater levels are hardly affected, but recession rates are noticeably more rapid and annual minima are lower.  
 656



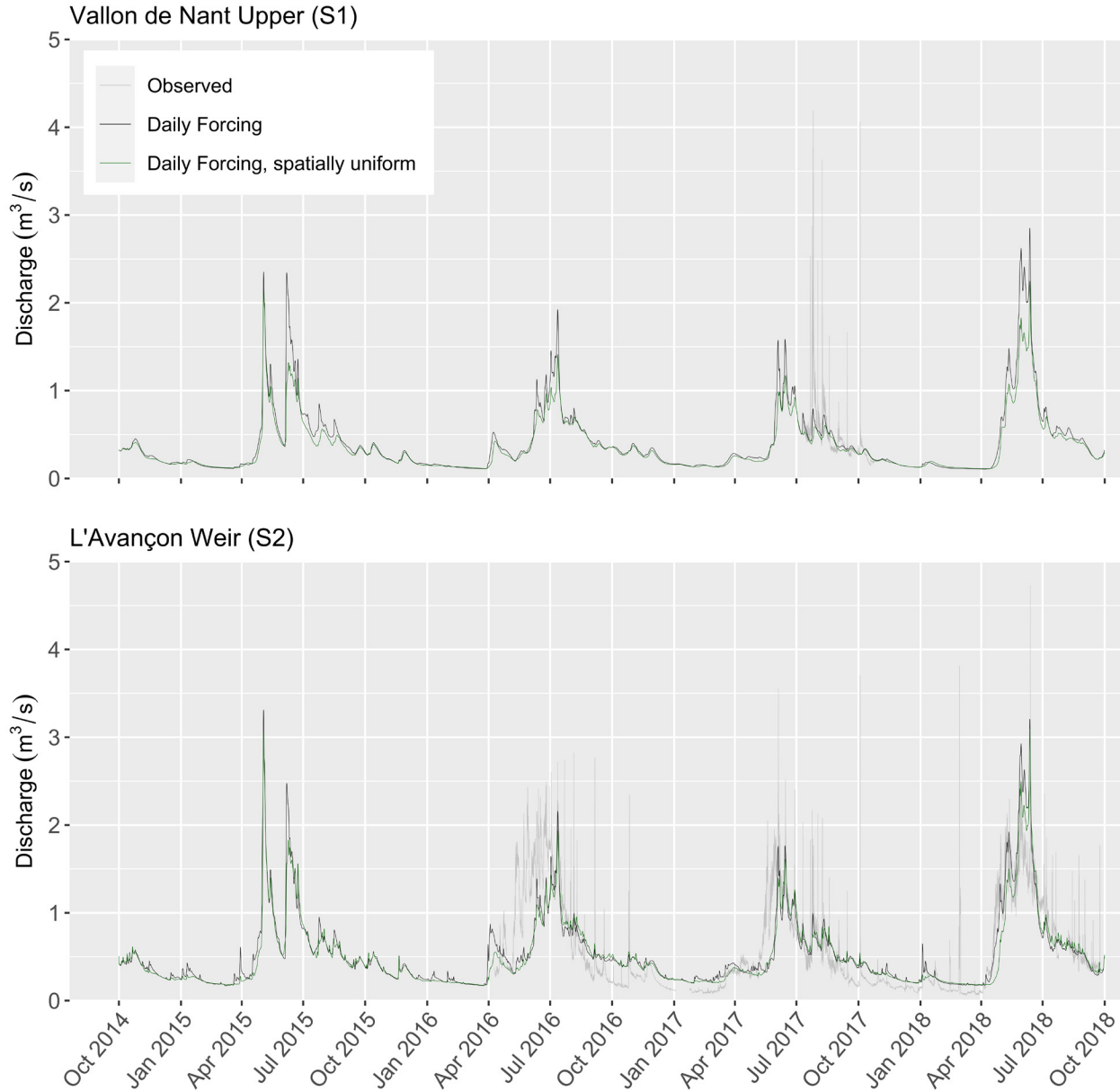
657 **Figure 9.** Streamflows simulated with a version of the fully integrated model whose depth (i.e. vertical extent) is  
 658 limited to a uniform 30 m beneath the surface (elements beneath this were deactivated, which is akin to applying a  
 659 “no flow” boundary condition). In this case, daily frequency, 25 m resolution forcing data were applied.  
 660  
 661  
 662



663  
664 **Figure 10.** Groundwater levels simulated with a version of the fully integrated model whose depth (i.e. vertical extent)  
665 is limited to a uniform 30 m beneath the surface (elements beneath this were deactivated, which is akin to applying a  
666 “no flow” boundary condition). In this case, daily frequency, 25 m resolution forcing data were applied.

667 3.2.3. Scenario C: Spatially-uniform forcing

668 Figure 11 shows the effect of applying spatially uniform forcing data in the Vallon de Nant sub-catchment. This  
 669 produces noticeably lower spring peaks, especially at the higher site (S1). The effect of applying spatially uniform  
 670 catchment-averaged forcing on groundwater levels (not shown) was found to be more modest and less variable over  
 671 the annual cycle.  
 672



673 **Figure 11.** Comparisons between simulated streamflows generated using 25 m resolution spatially distributed forcing  
 674 data and those generated using spatially-uniform (i.e. catchment-averaged) data. In both cases, the forcing data had  
 675 daily frequency.  
 676  
 677

678 3.2.4. Scenario D: No permafrost

680 For the final simplification – “no permafrost” – no discernible differences between the streamflows and groundwater  
 681 levels simulated at the various observation points by the full complexity model were apparent. As such, no plots are

682 presented here. An additional “end member” test (also not shown) in which the coupling length parameter was set to  
683 50 m across the entire catchment revealed only relatively minor differences with the main model results.

## 684 4. Discussion

### 685 4.1. General utility and reproduction of historical time-series using the full complexity model

686 None of the main phases involved – that is, obtaining the extensive data necessary to build this particular model,  
687 ensuring that it ran smoothly in acceptable timeframes, and then calibrating it such that the available observations  
688 could be reproduced with some skill, were straightforward. Mendoza et al. (2015) highlight that the levels of data fit  
689 attainable with such complex, physically-based models are often lower than those possible with simpler, more data-  
690 driven alternatives. As such, it is satisfying that the general dynamics of observed streamflow could be reproduced  
691 with daily forcing at S1 and S2 (Figure 3). The improved correspondence between observations and simulations over  
692 the independent evaluation period compared with the calibration period may seem slightly counterintuitive, but  
693 perhaps the forcing data were better estimated over the evaluation period (in Thornton et al., under revision; e.g. due  
694 to more complete/local input data being available). Provided it is not an artefact associated with an observational bias,  
695 another interesting feature of Figure 3 – that baseflows appear to be overestimated more at S2 than S1 – may enable  
696 potential deficiencies in the model to be attributed spatially, i.e. it could indicate a slight issue in the geometries and/or  
697 parameterizations of those zones (surface or subsurface) that only influence flow downstream of S1.

698  
699 The poor fit at S3 is likely due to the extreme geological complexity of this sub-catchment, on which data remains  
700 lacking, being insufficiently represented in the model. In reality, the high, topographically closed basin of La Varre,  
701 which is naturally dammed to a height of around 20 m, clearly does drain through the subsurface as no lake is present  
702 in the depression; there is merely a wetland at coordinates (576859,123516). It may be that in the initial  
703 parameterization, the unduly high effective hydraulic conductivities that were favored here in order to prevent a deep  
704 lake forming in the simulation, inducing a water table across the entire Vallon de La Vare sub-catchment that was  
705 unduly low. In turn, this may have enabled too much infiltration and recharge, at the expense of more rapid surface  
706 and shallow subsurface runoff, resulting in the overly constant simulated streamflow signal. In fact, La Varre may  
707 drain via a discrete fracture that bypasses several otherwise impermeable formation and potentially also gauging  
708 station S3 (Lugeon & Gagnebin, 1928). A “duality” in the hydrological functioning of this valley could therefore be  
709 posited, whereby snowmelt generated and rainfall incident in the upper part drain directly into the subsurface or else  
710 arrive at La Varre via surface torrents, whence they disappear into the subsurface. Some of this water may ultimately  
711 arrive in Le Richard (S3) via slow pathways, although the proportion (if any) is unknown. Meanwhile, based on the  
712 fairly flashy observed streamflow at S3, snowmelt and rainfall falling in the lower part would seem to be transmitted  
713 much more rapidly (e.g. via surface torrents). Essentially, in its current configuration, it seems that both aspects (i.e.  
714 no deep lake and a flashy streamflow response) cannot be captured in a single simulation. Superimposing discrete  
715 conduits / fractures on the porous media domain may be necessary to address any discrete subsurface flows in karstic  
716 conduits, and whilst this is theoretically possible in HGS, obtaining the information necessary to locate and  
717 parameterize these features in remote Alpine settings would be difficult.

718  
719 Essentially, given the post calibration results at S3, it would appear that the inversion algorithm used in the calibration  
720 and/or its practical implementation are incapable of “overcoming” any deficiencies associated with the model structure  
721 or initial parameterization prescribed in the Vallon de La Vare portion of the domain. If the model could have been  
722 made to run more quickly, (e.g. by developing a more efficient mesh or by some other means), it could have could  
723 have been possible to calibrate the model using daily or even hourly frequency forcing data instead of monthly, which  
724 would have been more satisfactory. It is also possible that the solution to the inverse problem (i.e. the calibration)  
725 reaches a local minimum, and/or that the bounds imposed on the effective parameter values of subsurface formations  
726 in the Vallon de La Vare region were too tight. Finally, it is conceivable that even if improved parameter values were  
727 proposed by PEST (i.e. those which would ordinarily produce to a more rapid streamflow response and hence a better

728 match at S3), the 18-month re-initialization period that was simulated prior to each calibration run may not have been  
729 long enough for the internal storages to re-equilibrate with the adjusted parameters. Ideally, a lengthier re-initialization  
730 period would have followed every change in parameter values, with this strictly continuing until a (close to) perfect  
731 “dynamic steady state” was re-established. However, due to the model’s runtimes (which also depend on the parameter  
732 values), such an approach would have precluded automated calibration altogether and was therefore impractical here.  
733 Interestingly, the interplay between initial conditions, parameter updates, and re-equilibration within automated  
734 optimization frameworks have received very little attention in the integrated modelling literature to date, and should  
735 be investigated more thoroughly.

736  
737 Regarding the groundwater levels (Figure 4), it is satisfying that the simulated dynamics at N4 generally correspond  
738 with the observations well, even if the simulated level is slightly high. This is because, being the nearest site to the  
739 main gravelly part of the alluvial fan, N4 can perhaps be considered to provide the most spatially representative data  
740 of all four piezometers. Besides the general points related to the calibration discussed above, one main reason can be  
741 proposed as to why model performance is generally fairly limited with respect to groundwater levels; namely the  
742 influence of local-scale heterogeneity in hydraulic properties. Specifically, whilst all the piezometers are located fairly  
743 close to one another (and are moreover in only a tiny part of the entire domain), the observed signals at each are rather  
744 distinctive. The flashy response of groundwater at N2, for instance, is understood to be an effect of it being in a former  
745 stream channel, with a relatively impermeable underlying clay-rich layer perhaps responsible for the remarkably  
746 constant lower level. Crucially, since all these sites are situated within a single model zone (the “Nant” alluvial fan  
747 system) to which homogenous material properties were assigned, it is unsurprising that the contrasting responses  
748 observed at each could not be reproduced. Indeed, the groundwater level data (which were relatively few to start with)  
749 were deliberately de-weighted in the calibration to prevent this structural deficiency being compensated for at the  
750 expense of the coherence of the broader numerical representation. To improve these fits, one would have to introduce  
751 sub-zone heterogeneity, but this may not greatly alter the simulation of catchment-scale dynamics. That said, it may  
752 be achievable, for instance, by employing the Iterative Ensemble Smoother (IES) approach of White (2018), which  
753 theoretically enables a very large number of parameters to be estimated (e.g. hydraulic conductivity per element) with  
754 relatively few model runs.

755  
756 Figures 6 and 7, meanwhile, demonstrate that applying forcing data with extremely high (hourly) temporal resolution,  
757 which is rarely done with HGS, brings some benefits in terms of reproducing diurnal fluctuations and sharp streamflow  
758 peaks. At first glance, one could hypothesize that the slight residual underestimation of some peaks could be associated  
759 with the localized convective events which drive them may have been “missed” by the gauge network from which the  
760 forcing datasets were generated, or that some of the many small, steep torrents which transmit snowmelt and rainfall  
761 extremely efficiently to larger channels are not represented explicitly enough in the mesh (cf. Ala-aho et al., 2017).  
762 However, the fact that streamflow peaks are reproduced well under the “impermeable matrix” assumption (Figure 8)  
763 suggests that neither explanation is likely. This provides an example of the insight that simpler model versions can  
764 provide. Rather, it is perhaps more likely that the surface and near-surface permeability may generally remain too high  
765 (leading to insufficient overland flow generation) and/or interception and evaporative losses being overly pronounced.  
766 Whatever the reason, Movie S1 suggests that small torrents do not appear to form extensively enough in the model  
767 compared with field experience compared to reality (field observations) – at least with the daily forcing frequency  
768 used here. Unfortunately, the monthly forcing data used for calibration did not contain information on these high-  
769 frequency dynamics, preventing parameters being adjusted to give better peak matches. Resolving the topography of  
770 small torrents in even more detail also could have helped, but under the established meshing approach would have  
771 resulted in an even larger mesh and hence even longer runtimes. Nevertheless, as it was, parameters from all three  
772 “domains” could be calibrated and initial the multi-component OF specified was reduced somewhat, indicating modest  
773 success.

774  
775 Lastly, the shallow simulated water depths shown in Movie S2 at the gauging station S2 (and indeed the corresponding  
776 observations) reveal that for much of the year in question, and presumably other years also, the stream network lies

777 close to the “wet-dry limit” even under present climatic conditions, and may therefore be highly sensitive to future  
778 change. Reproducing this “borderline” using such a numerical model is arguably much more difficult than replicating  
779 more voluminous flows along larger rivers.

780

#### 781 4.2. Insights from systematically simplified models

782 Only by initially developing complex models as baselines, as we do here, can one assess the impact of subsequent  
783 simplifications and conduct sensitivity analyses (see also Rapp et al., 2020; Schreiner-McGraw & Ajami, 2020). In  
784 Scenario A (Figure 8), the temporal pattern under/overestimation with respect to the observations align well with  
785 expectations; with infiltration and subsurface storage and discharge precluded here, the simulated spring and summer  
786 rainfall peaks are higher than their observed counterparts, whilst baseflows later in the year (which are clearly  
787 sustained by groundwater discharge in reality) are underestimated.

788 The certain degree of overestimation in the simulated streamflows evident at S1 and S2 with respect to the observations  
789 is expected, since in reality (and also in the fully-integrated version of the model presented already), a certain  
790 proportion of incident precipitation will be returned to the atmosphere via  $ET_a$  and hence never becomes streamflow,  
791 but this is not accounted for in this simulation. In fact, the results at the highest gauging station, S1, are particularly  
792 interesting. They definitively demonstrate that even ignoring any evapotranspirative losses, were it not for the  
793 sustaining influence of groundwater discharge, streamflow would frequently become negligible in summers/autumns  
794 following snow-poor winters such as 2016/2017. As such, they confirm the insight into the importance of groundwater  
795 discharge to baseflow that Figure 5(a) revealed.

796

797 That streamflows are most overestimated at S3 under this configuration is likely related to the bedrock geology in the  
798 Vallon de La Vare, which – as explained above and by Thornton et al. (2018) – is understood to be eminently  
799 permeable, unlike the substrate of the Vallon de Nant. Indeed, almost a century ago now, Lugeon and Gagnebin (1928)  
800 proved a hydrogeological connection between the topographically closed basin of La Varre and La Chambrette – a  
801 spring which joins the main channel below S3 – meaning that some water must bypass the station entirely. Hence,  
802 whilst in reality subsurface flow paths (in the upper part especially) should be longer and deeper, when all water is  
803 forced to flow overland (as in this scenario), streamflows are significantly overestimated.

804

805 The findings presented in Figures 9 and 10 (Scenario B) also make good conceptual sense; the imposition of a “no  
806 flow” boundary at 30 m depth forces the water table to be higher and enhances runoff generation during periods of  
807 snowmelt and intense rainfall. Due to reduced overall subsurface storage volumes, recessions are more pronounced  
808 and minimum levels are lower than the baseline case. As it is quite common for vertical domain extents to be limited  
809 when applying computationally intensive integrated hydrological models to real mountainous catchments, this  
810 sensitivity represents an important finding. In some previous studies, manual calibration may have compensated for  
811 this effect, which could partially undermine their subsequent predictions. The sensitivity of outputs to the vertical  
812 extent assumed should therefore be routinely assessed (see also Condon et al., 2020).

813

814 The fairly large differences between the simulations during the spring in Figure 11 (Scenario C) suggest that using  
815 spatially distributed forcing is important to reproduce spring flow peaks, especially at higher points along headwater  
816 stream networks. This is because snowmelt is generated at sequentially higher elevations and on different slope aspects  
817 as the melt season progresses. One would expect the difference seen when using catchment-averaged forcings to be  
818 amplified with increasing catchment area. It should be highlighted that the spatially uniform forcing dataset was  
819 generated by averaging the distributed outputs of Thornton et al. (under revision) at each time-step, meaning the  
820 difference could be even larger if “truly uniform” datasets are used.

821

822 Finally, the results of Scenario D (not shown) suggest that, probably given the presently limited permafrost extent  
823 here, its thaw would not have a major impact on streamflows. However, a full “thermally enabled” simulation that

824 accounts for pore water freeze-thaw and thermally modified hydraulic conductivities, rather than the simple coupling  
825 length approach used here, would probably have enabled greater confidence in this conclusion. Still, had this study  
826 intended to specifically evaluate the influence of permafrost on integrated hydrological processes, an alternative  
827 (higher elevation) study site and more permafrost-focused modelling strategy would certainly have been adopted.

#### 828 4.3. Main novelties

829 This study is associated with several novelties. The first relates to the subsurface structure employed, especially the  
830 incorporation of an accurate, high-resolution 3D model of bedrock geology (Thornton et al., 2018) to represent a  
831 vertically extensive domain with a fairly finely resolved mesh. The second lies in the application of forcing datasets  
832 with high spatial resolution. The snowmelt component in particular, which was generated previously using an energy  
833 balance-based snow model that additionally accounts for gravitational redistribution and was conditioned upon two  
834 complementary types of snow observations (Thornton et al., under revision), extends well beyond the approaches  
835 usually taken in integrated surface-subsurface modelling.

836 The underlying forcing data are highly resolved in both space and time. This enabled the impact of varying the  
837 frequency to be assessed. Prediction sensitivity to a range of other model simplifications was also evaluated. This  
838 study represents the first known attempt to calibrate an integrated hydrological model of a mountainous catchment in  
839 an automated fashion. Furthermore, detailed HGS models of real (as opposed to synthetic) mountainous catchments  
840 have not previously been presented. This is important because in contrast to some other integrated codes, HGS permits  
841 the free evolution of surface water network. It also supports flexible tetrahedral meshes, which can arguably represent  
842 complex topography more efficiently than the regular structured mesh employed by other popular integrated codes  
843 (but see Maxwell, 2013).

844 Finally, in contrast to many related previous studies (e.g. Carroll et al., 2019; Engdahl & Maxwell, 2015; Markovich  
845 et al., 2016; Penn et al., 2016; Pribulick et al., 2016), explicit time-series comparisons between simulations and  
846 historical observations are presented. In those studies, hydrological predictions made under modified conditions were  
847 only compared to simulated historical baselines. Whilst the physical basis of the models involved largely supports  
848 such an approach, actually demonstrating that historical observations can be reproduced (with plausible parameter  
849 values), as is done here, enhances confidence in the robustness of the model and simulated results. Through  
850 visualization of the simulations was also helpful in this regard and should not be overlooked, as tends to be the case  
851 presently.

#### 852 4.4. Fully-integrated hydrological models in complex mountainous settings: potential next steps

853 Based on this work, numerous recommendations for future research can be made (some of which have already been  
854 alluded to). Firstly, the interplay between initial conditions, parameter updates, and the (minimum) length of re-  
855 initialization periods (i.e. the periods that should be simulated with every new set of parameters prior to the  
856 commencement of calibration) when employing integrated models in automated calibration frameworks should be  
857 investigated. Secondly, when applying unstructured mesh-enabled integrated models to such topographically and  
858 geologically complex settings, mesh efficiency should be further improved. The mesh employed here – in which the  
859 same (surface constrained) mesh was replicated in every vertical layer – was a major limiting factor. Ideally, a fully-  
860 unstructured mesh refined according to surface features (streams, topography, etc.) in the upper few meters below the  
861 surface only, but then transitions to a mesh that is concordant only with geological formation interfaces beneath, can  
862 be envisaged. To ensure numerical stability, high quality element shapes must be maintained, however, which is  
863 unlikely to be trivial (depending on the degree of subsurface complexity). Associated improvements in runtimes could  
864 open many possibilities for calibrating such models over longer periods with higher frequency forcing data than those  
865 used here.

866

867 Accurate, spatially continuous (3D) data pertaining to the subsurface (in mountain regions but also elsewhere) also  
868 remains severely lacking, and thus acts as a major impediment to the more widespread uptake of integrated models.  
869 Few catchment or regional scale 3D models of the bedrock with appropriate attributes for groundwater or integrated  
870 hydrological models currently exist in global mountain regions, but can now be developed (Thornton et al., 2018).  
871 Approaches to estimate the geometries properties of numerous unconsolidated sedimentary features (i.e. across entire  
872 rugged, inaccessible headwaters), which are increasingly understood to play an important hydrological role, are also  
873 limited (see Supplementary Text S1). Finally, distributed (or even 3D) data on soil hydraulic properties is also lacking,  
874 even in relatively populated and developed mountain ranges such as the European Alps. As already noted, soils control  
875 water partitioning at the land surface, and so high-quality data are crucial for developing meaningful computational  
876 representations. With continued developments in satellite remote sensing, the already considerable disparity between  
877 the amount and quality of surface vs. subsurface data availability is only widening. Finally, applying integrated models  
878 to mountainous settings such as the Hindu Kush Himalaya or the Andes, where the effects of ongoing climate change  
879 are likely to be even more marked than previously studied settings, could also prove useful.

880  
881 It has hopefully been demonstrated above that, besides offering considerable visualization possibilities, such models  
882 allow one to apply physical reasoning to identify numerical representations that may still be deficient, and therefore  
883 prioritize future improvements and/or conceptual model refinements. Building upon this, there is great potential for  
884 numerous novel, complementary datasets to be combined with integrated models of mountainous catchments more  
885 formally for multi-objective calibration and evaluation (including spatially explicit elements). Such datasets could  
886 include remotely sensed *ET* maps (e.g. Allen et al., 2007), this being a generally uncertain water balance component,  
887 and estimates of seasonal groundwater storage determined via gravimetry (e.g. Arnoux et al., 2020), which would  
888 provide more spatially integrated, representative information than the piezometer measurements used here (see also  
889 Schilling, Cook et al., 2019). Employing the temporal evolution of the observed stream network as it expands and  
890 contracts (e.g. captured using drone photography) as a model constraint could also represent an attractive avenue.  
891 Ultimately, combining integrated models and such diverse datasets could reduce the extent to which equifinality  
892 afflicts such models and finally realize the vision of Grayson & Blöschl (2001). However, what constitutes “good”,  
893 “acceptable”, and “poor” model-data fits for various metric and variable combinations when employing such tools in  
894 complex mountainous systems remains to be established, including for basic time-series (as many similar studies did  
895 not present them).

## 896 **5. Conclusions**

897 This paper has presented a fully-integrated surface-subsurface hydrological model of a steep, snow-dominated  
898 mountainous catchment that incorporates both a dedicated 3D model of bedrock geology and an energy balance-based  
899 representation of snow processes: two structural advancements over previous mountain integrated modelling efforts  
900 that, given the region’s characteristics, were deemed important.

901  
902 In one of the first such attempts, the model was calibrated in an automated fashion with respect to observed  
903 streamflows and groundwater levels. Setting up and running such a model was found to be feasible, and after  
904 calibration the hydrological dynamics of the system could generally be replicated satisfactorily. These results suggest  
905 integrated models do indeed have utility in complex Alpine settings. It was additionally demonstrated that applying  
906 hourly instead of daily frequency forcing data enabled streamflows associated with snowmelt and rainfall, as well as  
907 diurnal fluctuations in streamflow and groundwater levels, to be reproduced.

908  
909 The capacities that integrated codes offer, via spatio-temporal data visualization and/or extraction, to develop  
910 improved understanding of complex hydrological systems – including the possibility to diagnose the aspects in which  
911 a given numerical representation may remain deficient – were also exploited. For example, a “soft evaluation” in  
912 which simulated patterns of surface-subsurface exchange fluxes were compared with those inferred from a thermal

913 drone image was undertaken, and further reinforced our view of the model's coherence in capturing observed surface-  
914 subsurface flow dynamics.

915  
916 Closely replicating observed streamflow at one site and the distinctive signals of groundwater levels observed in very  
917 close proximity to one another at the groundwater observation points was not possible with this model configuration,  
918 presumably due to the sub-catchment's distinctive geology and very local scale heterogeneities in hydraulic properties  
919 not being sufficiently represented, respectively. As such, here, the groundwater level data, which were also limited in  
920 quantity, contributed relatively little to the overall process. A risk of post-calibration non-uniqueness remains. This  
921 issue was not addressed here, with runtimes being the main impediment.

922  
923 Subsequently simplifying the "full complexity" model in a series of sensitivity tests revealed that:

- 924
- 925 • Were it not for the sustaining influence of groundwater discharge, streamflow would frequently become  
926 negligible in summers following snow-poor winters;
  - 927 • Limiting the model's vertical extent significantly affects simulated streamflows and groundwater levels,  
928 meaning care should be taken to ensure that simulation domains are sufficiently deep;
  - 929 • Applying spatially uniform forcing data affects simulated streamflow peaks at higher elevations along the  
930 stream network;
  - 931 • The thawing of all permafrost would have an almost indistinguishable impact on hydrological predictions  
932 (although the fairly simplistic way in which permafrost was represented in the base model somewhat limits  
933 the confidence that can be placed in this assertion).

934 Physically-based, integrated flow models thus provide an excellent basis for exploring the impacts of  
935 simplifications/approaches used across the full spectrum of hydrological model complexities, including those related  
936 to forcing data frequency.

937  
938 Several other recommendations for future research have emerged, such as i) investigating more fully the interplay  
939 between initial conditions and re-initialization simulation times, ii) developing dedicated methods to generate more  
940 efficient, fully-unstructured meshes for surface-subsurface models, ii) developing and applying methods to better  
941 describe the 3D geometries and hydraulic properties of unconsolidated subsurface formations, and iv) routinely testing  
942 the sensitivity of predictions to assumed watershed base depth. Additionally, many possibilities exist to introduce a  
943 range of complementary datasets constraints during multi-objective calibration processes, especially variables (besides  
944 streamflow) that provide spatially integrated information.

945  
946 In summary, this contribution attests to both the great potential and remaining challenges associated with applying  
947 fully-integrated models in very complex mountainous settings. Subsequently, the model will be used in conjunction  
948 with plausible future climate and vegetation scenarios to assess hydrological impacts in a more comprehensive fashion  
949 than has hitherto been possible. As such, this model in particular, and the framework more generally, may enable more  
950 reliable and comprehensive assessments to be made as to the hydrological impacts of future change in the European  
951 Alps and other similar regions globally than have hitherto been possible. That said, given the efforts required and  
952 difficulties associated with developing and calibrating, it is suggested that applications in exceptionally important or  
953 ecologically sensitive catchments, or else where much of the requisite data already exists, are prioritized.

954  
955 **Acknowledgments, Samples, and Data**

956 J.M.T, G.M. and P.B were financed by the Swiss National Science Foundation (IntegrAlp project; CR2312\_162754).  
957 The Authors wish to thank Dr. N. Deluigi for the provision of the permafrost map, R. Vallat for the provision of the  
958 permafrost map and thermal image, Drs. E. Voytek and L. Baron for their assistance with the geophysical survey and  
959 data processing, and the groups of Prof. B. Schaepli and Prof. T. Battin for the streamflow data. The authors declare

960 no conflict of interest. The calibrated model with daily forcing data is provided, along with the animations and  
961 Supplementary Figures, at: <https://doi.org/10.6084/m9.figshare.13332650>. To run the model, a HydroGeoSphere  
962 license would be required (contact [sales@aquanty.com](mailto:sales@aquanty.com)). The other model configurations described are available from  
963 the corresponding author upon request.

## 964 **Author contributions**

965 J.M.T. conducted the vast majority of the work, including making the groundwater measurements, sourcing the inputs  
966 datasets, setting up and calibrating the model, planning and executing the subsequent simulations, preparing the figures  
967 (except Figure S12), and writing the manuscript. R.T. provided advice and technical contributions regarding  
968 HydroGeoSphere. N.L. enabled the geophysics fieldwork and conducted the geophysical inversion. P.B. and G.M.  
969 were responsible for funding acquisition and provided advice and support at all stages. All authors contributed to the  
970 finalization of the manuscript.

## 971 **References**

- 972 Ajami, H., McCabe, M. F., Evans, J. P., & Stisen, S. (2014). Assessing the impact of model spin-up on surface water-  
973 groundwater interactions using an integrated hydrologic model. *Water Resources Research*, *50*(3), 2636–2656.  
974 <https://doi.org/10.1002/2013WR014258>
- 975 Ala-aho, P., Rossi, P. M., Isokangas, E., & Kløve, B. (2015). Fully integrated surface-subsurface flow modelling of  
976 groundwater-lake interaction in an esker aquifer: Model verification with stable isotopes and airborne thermal  
977 imaging. *Journal of Hydrology*, *522*, 391–406. <https://doi.org/10.1016/j.jhydrol.2014.12.054>
- 978 Ala-aho, P., Soulsby, C., Wang, H., & Tetzlaff, D. (2017). Integrated surface-subsurface model to investigate the role  
979 of groundwater in headwater catchment runoff generation: A minimalist approach to parameterisation. *Journal*  
980 *of Hydrology*, *547*, 664–677. <https://doi.org/10.1016/j.jhydrol.2017.02.023>
- 981 Ameli, A. A., Gabrielli, C., Morgenstern, U., & McDonnell, J. J. (2018). Groundwater Subsidy From Headwaters to  
982 Their Parent Water Watershed: A Combined Field-Modeling Approach. *Water Resources Research*, *54*(7),  
983 5110–5125. <https://doi.org/10.1029/2017WR022356>
- 984 Aquanty Inc. (2016). *HydroGeoSphere User Manual*. <https://doi.org/10.1007/s13398-014-0173-7.2>
- 985 Arnoux, M., Halloran, L. J. S., Berdat, E., & Hunkeler, D. (2020). Characterizing seasonal groundwater storage in  
986 alpine catchments using time-lapse gravimetry, water stable isotopes and water balance methods. *Hydrological*  
987 *Processes*, *34*(22), 4319–4333. <https://doi.org/10.1002/hyp.13884>
- 988 Badoux, H. (1971). *Carte et notice explicative, Feuille 1305 - Dt. de Morcles, Atlas géologique de la Suisse (1:25,000)*.
- 989 Beniston, M., Farinotti, D., Stoffel, M., Andreassen, L. M., Coppola, E., Eckert, N., ... Vincent, C. (2018). The  
990 European mountain cryosphere: a review of its current state, trends, and future challenges. *The Cryosphere*,  
991 *12*(2), 759–794. <https://doi.org/10.5194/tc-12-759-2018>
- 992 Beven, K. J., & Kirkby, M. J. (1979). A physically based, variable contributing area model of basin hydrology.  
993 *Hydrological Sciences Bulletin*, *24*(1), 43–69. <https://doi.org/10.1080/02626667909491834>
- 994 Brauchli, T., Trujillo, E., Huwald, H., & Lehning, M. (2017). Influence of slope-scale snowmelt on catchment  
995 response simulated with the Alpine3D model. *Water Resources Research*, *53*(12), 10723–10739.  
996 <https://doi.org/10.1002/2017WR021278>
- 997 Camporese, M., Paniconi, C., Putti, M., & McDonnell, J. J. (2019). Fill and Spill Hillslope Runoff Representation  
998 With a Richards Equation-Based Model. *Water Resources Research*, *55*(11), 8445–8462.  
999 <https://doi.org/10.1029/2019WR025726>

- 1000 Carroll, R. W. H., Deems, J. S., Niswonger, R., Schumer, R., & Williams, K. H. (2019). The importance of interflow  
 1001 to groundwater recharge in a snowmelt-dominated headwater basin. *Geophysical Research Letters*, 46(11),  
 1002 5899–5908. <https://doi.org/10.1029/2019GL082447>
- 1003 Ceperley, N., Michelon, Anthony Escoffier, N., Mayoraz, G., Boix Canadell, M., Horgby, A., Hammer, F., ... Boss,  
 1004 S. (2018). Salt gauging and stage-discharge curve, Avançon de Nant, outlet Vallon de Nant catchment.  
 1005 <https://doi.org/10.5281/zenodo.1154798>
- 1006 Cochand, F., Therrien, R., & Lemieux, J. M. (2019). Integrated Hydrological Modeling of Climate Change Impacts  
 1007 in a Snow-Influenced Catchment. *Groundwater*, 57(1), 3–20. <https://doi.org/10.1111/gwat.12848>
- 1008 Condon, L. E., Markovich, K. H., Kelleher, C. A., McDonnell, J. J., Ferguson, G., & McIntosh, J. C. (2020). Where  
 1009 Is the Bottom of a Watershed? *Water Resources Research*, 56(3). <https://doi.org/10.1029/2019WR026010>
- 1010 Deluigi, N., Lambiel, C., & Kanevski, M. (2017). Data-driven mapping of the potential mountain permafrost  
 1011 distribution. *Science of the Total Environment*, 590–591, 370–380.  
 1012 <https://doi.org/10.1016/j.scitotenv.2017.02.041>
- 1013 Doherty, J. (2020). *PEST\_HP: PEST for Highly Parallelized Computing Environments*. Brisbane, Australia. Retrieved  
 1014 from <http://www.pesthomepage.org/Downloads.php>
- 1015 Duethmann, D., Blöschl, G., & Parajka, J. (2020). Why does a conceptual hydrological model fail to correctly predict  
 1016 discharge changes in response to climate change? *Hydrology and Earth System Sciences*, 24(7), 3493–3511.  
 1017 <https://doi.org/10.5194/hess-24-3493-2020>
- 1018 Durighetto, N., Vingiani, F., Bertassello, L. E., Camporese, M., & Botter, G. (2020). Intraseasonal Drainage Network  
 1019 Dynamics in a Headwater Catchment of the Italian Alps. *Water Resources Research*, 56(4).  
 1020 <https://doi.org/10.1029/2019WR025563>
- 1021 Ebel, B. A., Mirus, B. B., Heppner, C. S., VanderKwaak, J. E., & Loague, K. (2009). First-order exchange coefficient  
 1022 coupling for simulating surface water-groundwater interactions: parameter sensitivity and consistency with a  
 1023 physics-based approach. *Hydrological Processes*, 23(13), 1949–1959. <https://doi.org/10.1002/hyp.7279>
- 1024 Engdahl, N. B., & Maxwell, R. M. (2015). Quantifying changes in age distributions and the hydrologic balance of a  
 1025 high-mountain watershed from climate induced variations in recharge. *Journal of Hydrology*, 522, 152–162.  
 1026 <https://doi.org/10.1016/j.jhydrol.2014.12.032>
- 1027 Evans, S. G., Ge, S., & Liang, S. (2015). Analysis of groundwater flow in mountainous, headwater catchments with  
 1028 permafrost. *Water Resources Research*, 51(12), 9564–9576. <https://doi.org/10.1002/2015WR017732>
- 1029 Fatichi, S., Rimkus, S., Burlando, P., Bordoy, R., & Molnar, P. (2015). High-resolution distributed analysis of climate  
 1030 and anthropogenic changes on the hydrology of an Alpine catchment. *Journal of Hydrology*, 525, 362–382.  
 1031 <https://doi.org/10.1016/j.jhydrol.2015.03.036>
- 1032 Foster, L. M., & Maxwell, R. M. (2019). Sensitivity analysis of hydraulic conductivity and Manning’s n parameters  
 1033 lead to new method to scale effective hydraulic conductivity across model resolutions. *Hydrological Processes*,  
 1034 33(3), 332–349. <https://doi.org/10.1002/hyp.13327>
- 1035 Frisbee, M. D., Tolley, D. G., & Wilson, J. L. (2017). Field estimates of groundwater circulation depths in two  
 1036 mountainous watersheds in the western U.S. and the effect of deep circulation on solute concentrations in  
 1037 streamflow. *Water Resources Research*, 53(4), 2693–2715. <https://doi.org/10.1002/2016WR019553>
- 1038 Giaccone, E., Luoto, M., Vittoz, P., Guisan, A., Mariéthoz, G., & Lambiel, C. (2019). Influence of microclimate and  
 1039 geomorphological factors on alpine vegetation in the Western Swiss Alps. *Earth Surface Processes and  
 1040 Landforms*, 44(15), 3093–3107. <https://doi.org/10.1002/esp.4715>

- 1041 Gleeson, T., & Manning, A. H. (2008). Regional groundwater flow in mountainous terrain: Three-dimensional  
 1042 simulations of topographic and hydrogeologic controls. *Water Resources Research*, 44(10).  
 1043 <https://doi.org/10.1029/2008WR006848>
- 1044 Graham, D. N., & Butts, M. B. (2005). Flexible, integrated watershed modelling with MIKE SHE. In V. P. Singh &  
 1045 D. K. Frevert (Eds.), *Watershed Models* (pp. 245–272). CRC Press.
- 1046 Grayson, R. B., & Blöschl, G. (2001). *Spatial patterns in catchment hydrology: Observations and modelling*.  
 1047 Cambridge: Cambridge University Press.
- 1048 Griessinger, N., Schirmer, M., Helbig, N., Winstral, A., Michel, A., & Jonas, T. (2019). Implications of observation-  
 1049 enhanced energy-balance snowmelt simulations for runoff modeling of Alpine catchments. *Advances in Water*  
 1050 *Resources*, 133, 103410. <https://doi.org/10.1016/j.advwatres.2019.103410>
- 1051 Huntington, J. L., & Niswonger, R. G. (2012). Role of surface-water and groundwater interactions on projected  
 1052 summertime streamflow in snow dominated regions: An integrated modeling approach. *Water Resources*  
 1053 *Research*, 48(11). <https://doi.org/10.1029/2012WR012319>
- 1054 Hwang, H. T., Park, Y. J., Sudicky, E. A., Berg, S. J., McLaughlin, R., & Jones, J. P. (2018). Understanding the water  
 1055 balance paradox in the Athabasca River Basin, Canada. *Hydrological Processes*, 32(6), 729–746.  
 1056 <https://doi.org/10.1002/hyp.11449>
- 1057 HydroAlgorithmics. (2016). AlgoMesh User Guide, 257. Retrieved from  
 1058 [https://static1.squarespace.com/static/569e33fad82d5e0d877c25d7/t/57b28ab6579fb3a225563e6e/147131880](https://static1.squarespace.com/static/569e33fad82d5e0d877c25d7/t/57b28ab6579fb3a225563e6e/1471318805055/AlgoMesh+User+Guide+v1.2.pdf)  
 1059 [5055/AlgoMesh+User+Guide+v1.2.pdf](https://static1.squarespace.com/static/569e33fad82d5e0d877c25d7/t/57b28ab6579fb3a225563e6e/1471318805055/AlgoMesh+User+Guide+v1.2.pdf)
- 1060 Ilja Van Meerveld, H. J., Kirchner, J. W., Vis, M. J. P., Assendelft, R. S., & Seibert, J. (2019). Expansion and  
 1061 contraction of the flowing stream network alter hillslope flowpath lengths and the shape of the travel time  
 1062 distribution. *Hydrology and Earth System Sciences*, 23(11), 4825–4834. [https://doi.org/10.5194/hess-23-4825-](https://doi.org/10.5194/hess-23-4825-2019)  
 1063 [2019](https://doi.org/10.5194/hess-23-4825-2019)
- 1064 Immerzeel, W. W., Lutz, A. F., Andrade, M., Bahl, A., Biemans, H., Bolch, T., ... Baillie, J. E. M. (2020). Importance  
 1065 and vulnerability of the world's water towers. *Nature*, 577(7790), 364–369. [https://doi.org/10.1038/s41586-019-](https://doi.org/10.1038/s41586-019-1822-y)  
 1066 [1822-y](https://doi.org/10.1038/s41586-019-1822-y)
- 1067 Jaros, A., Rossi, P. M., Ronkanen, A. K., & Kløve, B. (2019). Parameterisation of an integrated groundwater-surface  
 1068 water model for hydrological analysis of boreal aapa mire wetlands. *Journal of Hydrology*, 575(November  
 1069 2018), 175–191. <https://doi.org/10.1016/j.jhydrol.2019.04.094>
- 1070 Jenicek, M., Seibert, J., & Staudinger, M. (2018). Modeling of Future Changes in Seasonal Snowpack and Impacts on  
 1071 Summer Low Flows in Alpine Catchments. *Water Resources Research*, 54(1), 538–556.  
 1072 <https://doi.org/10.1002/2017WR021648>
- 1073 Käser, D., Graf, T., Cochand, F., McLaren, R., Therrien, R., & Brunner, P. (2014). Channel Representation in  
 1074 Physically Based Models Coupling Groundwater and Surface Water: Pitfalls and How to Avoid Them.  
 1075 *Groundwater*, 52(6), 827–836. <https://doi.org/10.1111/gwat.12143>
- 1076 Klemeš, V. (1990). The modelling of mountain hydrology: the ultimate challenge. *Hydrology of Mountainous Areas*  
 1077 *(Proceedings of the Strbské Pleso Workshop, Czechoslovakia, June 1988)*, (190), 29–44.  
 1078 [https://doi.org/10.1641/0006-3568\(2001\)051\[0227:HIOEPA\]2.0.CO;2](https://doi.org/10.1641/0006-3568(2001)051[0227:HIOEPA]2.0.CO;2)
- 1079 Kristensen, K. J., & Jensen, S. E. (1975). A model for estimating actual evapotranspiration from potential  
 1080 evapotranspiration. *Hydrology Research*, 6(3), 170–188. <https://doi.org/10.2166/nh.1975.0012>
- 1081 Lehning, M., Völksch Ingo, I., Gustafsson, D., Nguyen, T. A., Stähli, M., & Zappa, M. (2006). ALPINE3D: A detailed

- 1082 model of mountain surface processes and its application to snow hydrology. In *Hydrological Processes* (Vol.  
1083 20, pp. 2111–2128). <https://doi.org/10.1002/hyp.6204>
- 1084 Liggett, J. E., Werner, A. D., & Simmons, C. T. (2012). Influence of the first-order exchange coefficient on simulation  
1085 of coupled surface-subsurface flow. *Journal of Hydrology*, 414–415, 503–515.  
1086 <https://doi.org/10.1016/j.jhydrol.2011.11.028>
- 1087 Lugeon, M., & Gagnebin, E. (1928). L'origine des sources de la Chambrette aux Plans sur Bex (Alpes Vaudoises).  
1088 *Bulletin de La Société Vaudoise Des Sciences*, 56.
- 1089 Maina, F. Z., & Siirila-Woodburn, E. R. (2020). Watersheds dynamics following wildfires: Nonlinear feedbacks and  
1090 implications on hydrologic responses. *Hydrological Processes*, 34(1), 33–50. <https://doi.org/10.1002/hyp.13568>
- 1091 Markovich, K. H., Maxwell, R. M., & Fogg, G. E. (2016). Hydrogeological response to climate change in alpine  
1092 hillslopes. *Hydrological Processes*, 30(18), 3126–3138. <https://doi.org/10.1002/hyp.10851>
- 1093 Markstrom, S. L., Niswonger, R. G., Regan, R. S., Prudic, D. E., & Barlow, P. M. (2008). GSFLOW—Coupled  
1094 Ground-Water and Surface-Water Flow Model Based on the Integration of the Precipitation-Runoff Modeling  
1095 System (PRMS) and the Modular Ground-Water Flow Model (MODFLOW-2005). *U.S. Geological Survey*,  
1096 (Techniques and Methods 6-D1), 240. Retrieved from <http://pubs.er.usgs.gov/publication/tm6D1>
- 1097 Maxwell, R M, Condon, L. E., & Kollet, S. J. (2015). A high-resolution simulation of groundwater and surface water  
1098 over most of the continental US with the integrated hydrologic model ParFlow v3. *Geoscientific Model*  
1099 *Development*, 8(3), 923–937. <https://doi.org/10.5194/gmd-8-923-2015>
- 1100 Maxwell, Reed M. (2013). A terrain-following grid transform and preconditioner for parallel, large-scale, integrated  
1101 hydrologic modeling. *Advances in Water Resources*, 53, 109–117.  
1102 <https://doi.org/10.1016/j.advwatres.2012.10.001>
- 1103 Maxwell, Reed M., Putti, M., Meyerhoff, S., Delfs, J.-O., Ferguson, I. M., Ivanov, V., ... Sulis, M. (2014). Surface-  
1104 subsurface model intercomparison: A first set of benchmark results to diagnose integrated hydrology and  
1105 feedbacks. *Water Resources Research*, 50(2), 1531–1549. <https://doi.org/10.1002/2013WR013725>
- 1106 Miller, K. L., Berg, S. J., Davison, J. H., Sudicky, E. A., & Forsyth, P. A. (2018). Efficient uncertainty quantification  
1107 in fully-integrated surface and subsurface hydrologic simulations. *Advances in Water Resources*, 111(June  
1108 2017), 381–394. <https://doi.org/10.1016/j.advwatres.2017.10.023>
- 1109 OFAG. (1980). Carte des aptitudes des sols de la Suisse. Retrieved from  
1110 [https://files.be.ch/bve/agi/geoportail/geo/lpi/BEK\\_2000\\_02\\_LANG\\_FR.PDF](https://files.be.ch/bve/agi/geoportail/geo/lpi/BEK_2000_02_LANG_FR.PDF)
- 1111 Paniconi, C., & Putti, M. (2015). Physically based modeling in catchment hydrology at 50: Survey and outlook. *Water*  
1112 *Resources Research*, 51(9), 7090–7129. <https://doi.org/10.1002/2015WR017780>
- 1113 Penn, C. A., Bearup, L. A., Maxwell, R. M., & Clow, D. W. (2016). Numerical experiments to explain multiscale  
1114 hydrological responses to mountain pine beetle tree mortality in a headwater watershed. *Water Resources*  
1115 *Research*, 52(4), 3143–3161. <https://doi.org/10.1002/2015WR018300>
- 1116 Ragetti, S., Cortés, G., Mcphee, J., & Pellicciotti, F. (2014). An evaluation of approaches for modelling hydrological  
1117 processes in high-elevation, glacierized Andean watersheds. *Hydrological Processes*, 28(23), 5674–5695.  
1118 <https://doi.org/10.1002/hyp.10055>
- 1119 Rapp, G. A., Condon, L. E., & Markovich, K. H. (2020). Sensitivity of Simulated Mountain-Block Hydrology to  
1120 Subsurface Conceptualization. *Water Resources Research*. <https://doi.org/10.1029/2020wr027714>
- 1121 Schattan, P., Schwaizer, G., Schöber, J., & Achleitner, S. (2020). The complementary value of cosmic-ray neutron

- 1122 sensing and snow covered area products for snow hydrological modelling. *Remote Sensing of Environment*,  
1123 239(December 2019), 111603. <https://doi.org/10.1016/j.rse.2019.111603>
- 1124 Schilling, O. S., Cook, P. G., & Brunner, P. (2019). Beyond Classical Observations in Hydrogeology: The Advantages  
1125 of Including Exchange Flux, Temperature, Tracer Concentration, Residence Time, and Soil Moisture  
1126 Observations in Groundwater Model Calibration. *Reviews of Geophysics*, 57(1), 146–182.  
1127 <https://doi.org/10.1029/2018RG000619>
- 1128 Schilling, O. S., Park, Y. J., Therrien, R., & Nagare, R. M. (2019). Integrated Surface and Subsurface Hydrological  
1129 Modeling with Snowmelt and Pore Water Freeze--Thaw. *Groundwater*, 57(1), 63–74.  
1130 <https://doi.org/10.1111/gwat.12841>
- 1131 Schreiner-McGraw, A. P., & Ajami, H. (2020). Impact of uncertainty in precipitation forcing datasets on the  
1132 hydrologic budget of an integrated hydrologic model in mountainous terrain. *Water Resources Research*, (541),  
1133 0–3. <https://doi.org/10.1029/2020WR027639>
- 1134 Schulla, J. (2017). *WaSiM (Water balance Simulation Model) Model Description*. Zürich. Retrieved from  
1135 [http://www.wasim.ch/downloads/doku/wasim/wasim\\_2015\\_en.pdf](http://www.wasim.ch/downloads/doku/wasim/wasim_2015_en.pdf)
- 1136 Seck, A., Welty, C., & Maxwell, R. M. (2015). Spin-up behavior and effects of initial conditions for an integrated  
1137 hydrologic model. *Water Resources Research*, 51(4), 2188–2210. <https://doi.org/10.1002/2014WR016371>
- 1138 Shrestha, M., Koike, T., Hirabayashi, Y., Xue, Y., Wang, L., Rasul, G., & Ahmad, B. (2015). Integrated simulation  
1139 of snow and glacier melt in water and energy balance-based, distributed hydrological modeling framework at  
1140 Hunza River Basin of Pakistan Karakoram region. *Journal of Geophysical Research: Atmospheres*, 120(10),  
1141 4889–4919. <https://doi.org/10.1002/2014JD022666>
- 1142 Smerdon, B. D., Mendoza, C. A., & Devito, K. J. (2007). Simulations of fully coupled lake-groundwater exchange in  
1143 a subhumid climate with an integrated hydrologic model. *Water Resources Research*, 43(1), 1416.  
1144 <https://doi.org/10.1029/2006WR005137>
- 1145 Speich, M. J. R., Zappa, M., Scherstjanoi, M., & Lischke, H. (2020). FORests and HYdrology under Climate Change  
1146 in Switzerland v1.0: a spatially distributed model combining hydrology and forest dynamics. *Geoscientific  
1147 Model Development*, 13(2), 537–564. <https://doi.org/10.5194/gmd-13-537-2020>
- 1148 Sulis, M., Paniconi, C., & Camporese, M. (2011). Impact of grid resolution on the integrated and distributed response  
1149 of a coupled surface-subsurface hydrological model for the des Anglais catchment, Quebec. *Hydrological  
1150 Processes*, 25(12), 1853–1865. <https://doi.org/10.1002/hyp.7941>
- 1151 Thornton, J. M., Mariethoz, G., Brauchli, T. J., & Brunner, P. (n.d.). Efficient multi-objective calibration and  
1152 uncertainty analysis of distributed snow simulations in rugged alpine terrain. *Journal of Hydrology*. Under  
1153 revision.
- 1154 Thornton, J. M., Mariethoz, G., & Brunner, P. (2018). A 3D geological model of a structurally complex alpine region  
1155 as a basis for interdisciplinary research. *Scientific Data*, 5, 1–20. <https://doi.org/10.1038/sdata.2018.238>
- 1156 Tolley, D., Foglia, L., & Harter, T. (2019). Sensitivity Analysis and Calibration of an Integrated Hydrologic Model in  
1157 an Irrigated Agricultural Basin With a Groundwater-Dependent Ecosystem. *Water Resources Research*, 55(9),  
1158 7876–7901. <https://doi.org/10.1029/2018WR024209>
- 1159 van Genuchten, M. T. (1980). A closed-form equation for predicting the hydraulic conductivity of unsaturated soils.  
1160 *Soil Science Society of America Journal*, 44, 892–898. Retrieved from <https://hwbdocuments.env.nm.gov/Los>  
1161 Alamos National Labs/TA 54/11569.pdf
- 1162 Viviroli, D., Kummu, M., Meybeck, M., Kallio, M., & Wada, Y. (2020). Increasing dependence of lowland

- 1163 populations on mountain water resources. *Nature Sustainability*. <https://doi.org/10.1038/s41893-020-0559-9>
- 1164 Voeckler, H. M., Allen, D. M., & Alila, Y. (2014). Modeling coupled surface water – Groundwater processes in a  
1165 small mountainous headwater catchment. *Journal of Hydrology*, 517, 1089–1106.  
1166 <https://doi.org/10.1016/j.jhydrol.2014.06.015>
- 1167 von Gunten, D., Wöhling, T., Haslauer, C., Merchán, D., Causapé, J., & Cirpka, O. A. (2014). Efficient calibration of  
1168 a distributed pde-based hydrological model using grid coarsening. *Journal of Hydrology*, 519(PD), 3290–3304.  
1169 <https://doi.org/10.1016/j.jhydrol.2014.10.025>
- 1170 Wagner, T., Themeßl, M., Schüppel, A., Gobiet, A., Stigler, H., & Birk, S. (2017). Impacts of climate change on  
1171 stream flow and hydro power generation in the Alpine region. *Environmental Earth Sciences*, 76(1), 4.  
1172 <https://doi.org/10.1007/s12665-016-6318-6>
- 1173 Wang, C., Gomez-Velez, J. D., & Wilson, J. L. (2018). The Importance of Capturing Topographic Features for  
1174 Modeling Groundwater Flow and Transport in Mountainous Watersheds. *Water Resources Research*, 54(12),  
1175 10,313-10,338. <https://doi.org/10.1029/2018WR023863>
- 1176 Warscher, M., Strasser, U., Kraller, G., Marke, T., Franz, H., & Kunstmann, H. (2013). Performance of complex snow  
1177 cover descriptions in a distributed hydrological model system: A case study for the high Alpine terrain of the  
1178 Berchtesgaden Alps. *Water Resources Research*, 49(5), 2619–2637. <https://doi.org/10.1002/wrcr.20219>
- 1179 Welch, L. A., & Allen, D. M. (2014). Hydraulic conductivity characteristics in mountains and implications for  
1180 conceptualizing bedrock groundwater flow. *Hydrogeology Journal*, 22(5), 1003–1026.  
1181 <https://doi.org/10.1007/s10040-014-1121-5>
- 1182 White, J. T. (2018). A model-independent iterative ensemble smoother for efficient history-matching and uncertainty  
1183 quantification in very high dimensions. *Environmental Modelling and Software*, 109(March), 191–201.  
1184 <https://doi.org/10.1016/j.envsoft.2018.06.009>
- 1185

Supporting Information for

**Simulating fully-integrated hydrological dynamics in complex Alpine headwaters**

Thornton, J.M.<sup>1</sup>, Therrien, R.<sup>2</sup>, Mariéthoz, G.<sup>3</sup>, Linde, N.<sup>4</sup> and Brunner, P.<sup>1</sup>

<sup>1</sup>Centre for Hydrogeology and Geothermics, University of Neuchâtel, Switzerland

<sup>2</sup>Department of Geology and Geological Engineering, University of Laval, Canada

<sup>3</sup>Institute of Earth Surface Dynamics, University of Lausanne, Switzerland

<sup>4</sup>Institute of Earth Sciences, University of Lausanne, Switzerland

**Contents of this file**

Figures S1 to S15

Text S1

**Additional Supporting Information (Files uploaded separately)**

Captions for Tables S1 to S3

Captions for Movies S1 to S3

**Introduction**

This file contains supplementary figures, describes the methods taken to estimate unconsolidated sedimentary formation geometries, and provides captions for supplementary tables and animations.



**Figure S1.** Photographs showing a) the concrete weir gauging station S2, and b) the installation of piezometer N4.

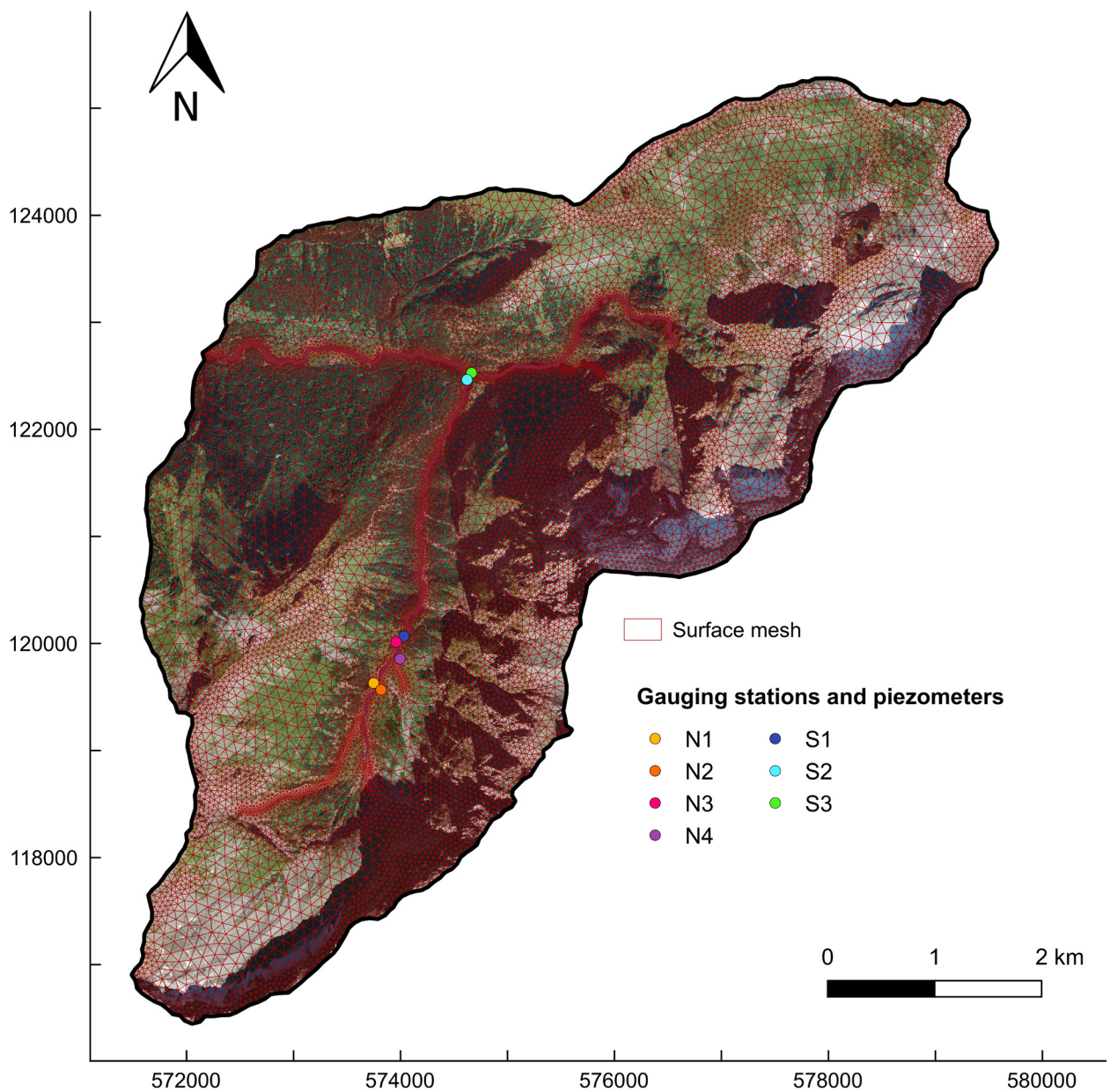


**Figure S2.** The 2D surface triangular mesh, underlain by a high resolution aerial photograph (Source: ©swisstopo). Refinement is highest in the riparian zone and in steep areas. Care was also taken to ensure that nodes were placed at the precise coordinates of the observation points (piezometers, denoted by N, and streamflow gauging stations, denoted by S).

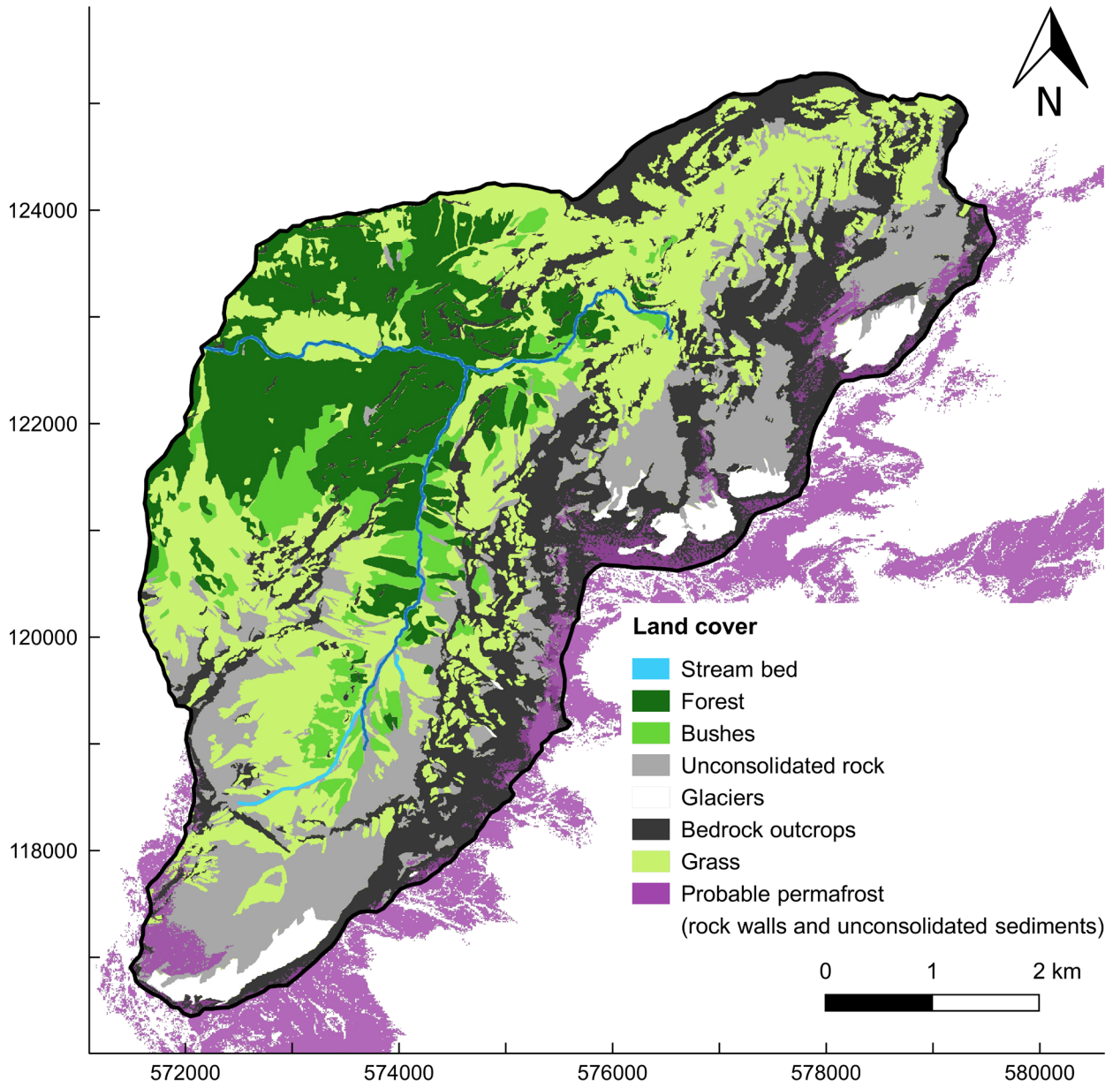


**Figure S3.** Land cover map of the study area, including estimated (present) permafrost distribution, that was used to define surface and evapotranspiration zones in the integrated model.

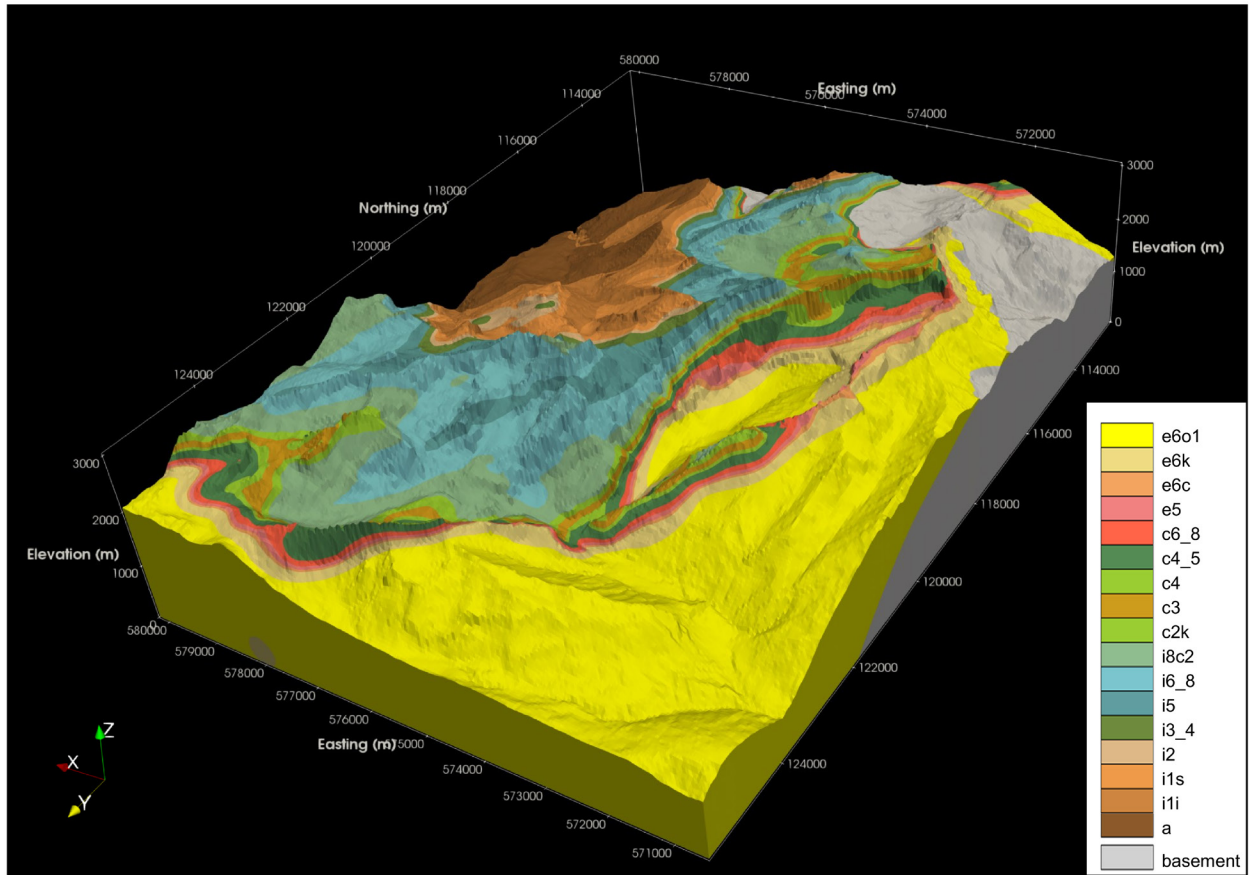


**Figure S4.** Illustration of the 3D bedrock geological model that contributed to the definition of subsurface zones in the integrated flow model. Source: Thornton et al. (2018).

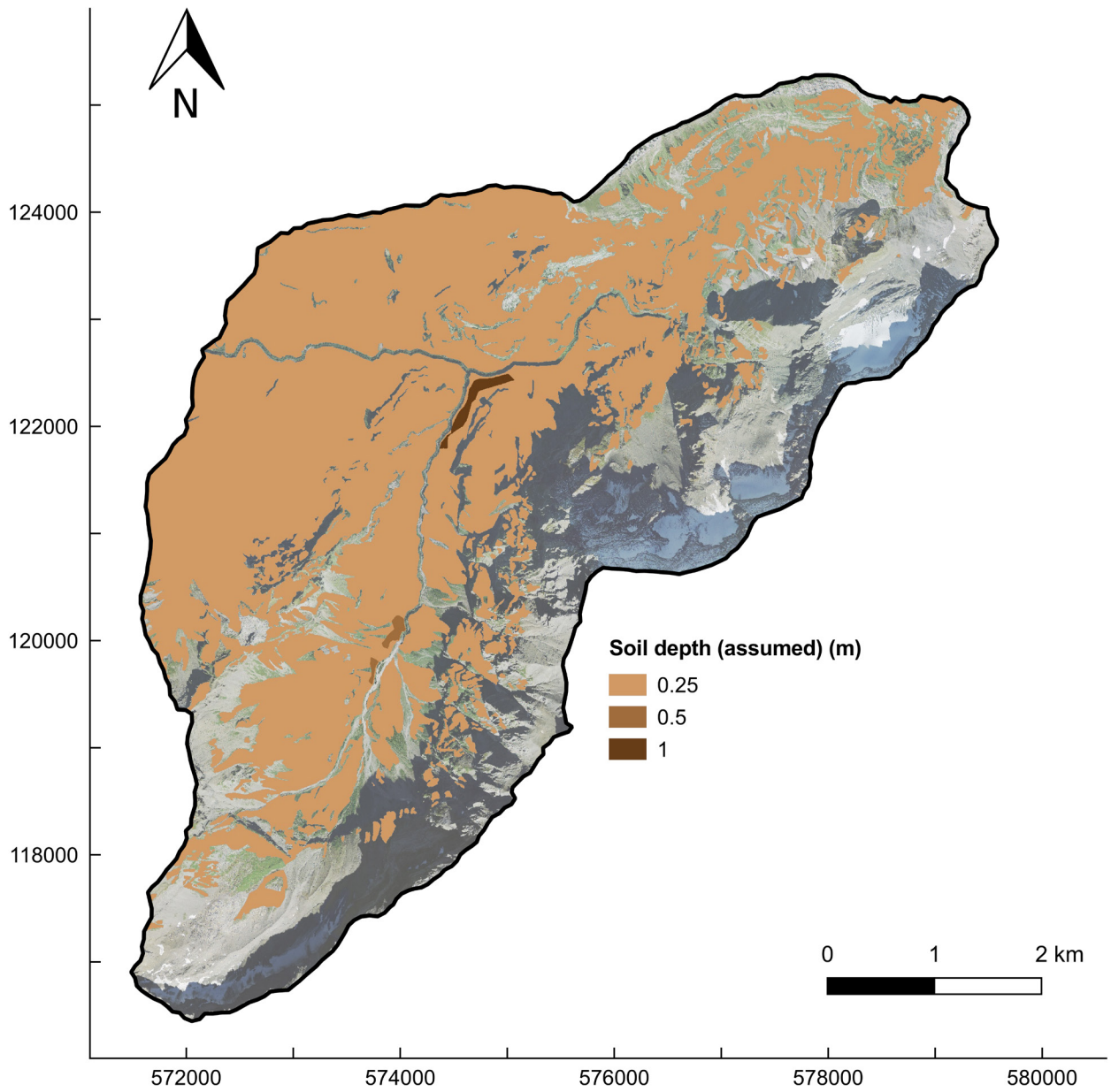


**Figure S5.** The spatial distribution of soil depth that was assumed in the integrated model in the absence of any detailed, high-resolution spatial information on soil depths and properties. Where the underlying aerial imagery is visible, no soil layer is represented.

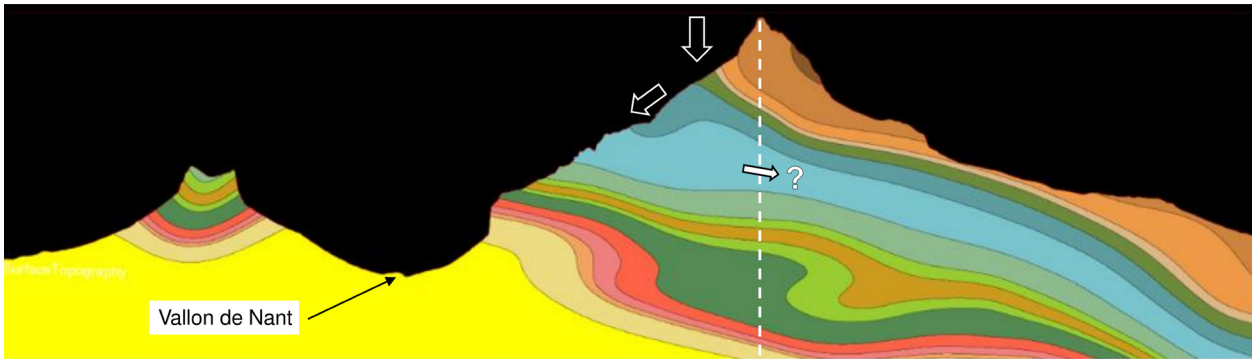


**Figure S6.** Cross-section through the 3D bedrock geological model showing the possibility for groundwater exportation across the topographic divide on the eastern flank of the Vallon de Nant, which is illustrated using the dashed white line (i.e. across the no-flow boundary in the model).

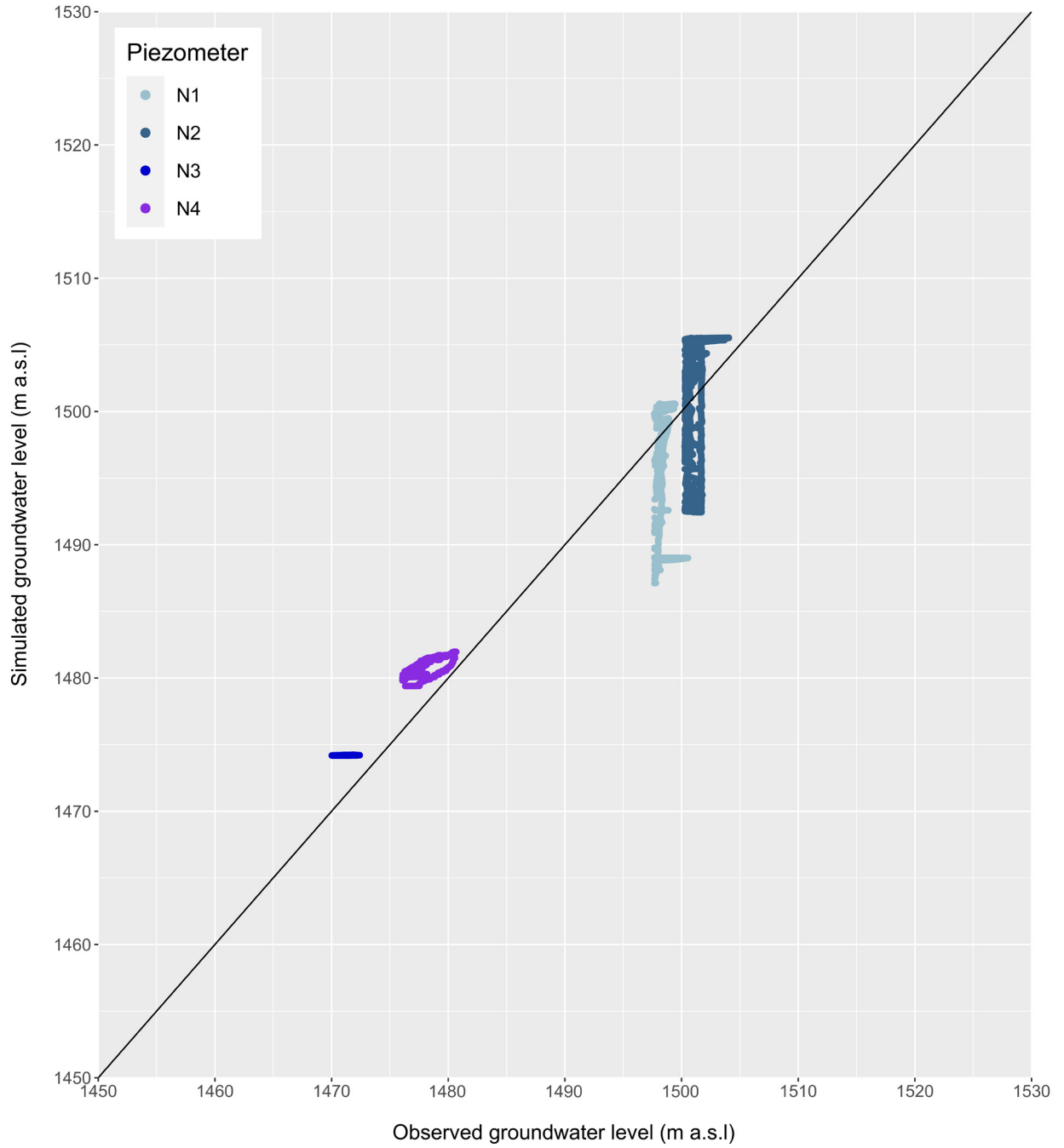


**Figure S7.** Pairwise plot of observed and simulated groundwater levels. The simulated levels were generated using the version of the model forced by daily frequency data. Model outputs were interpolated in time onto the half-hourly observation time-step to facilitate the plot.

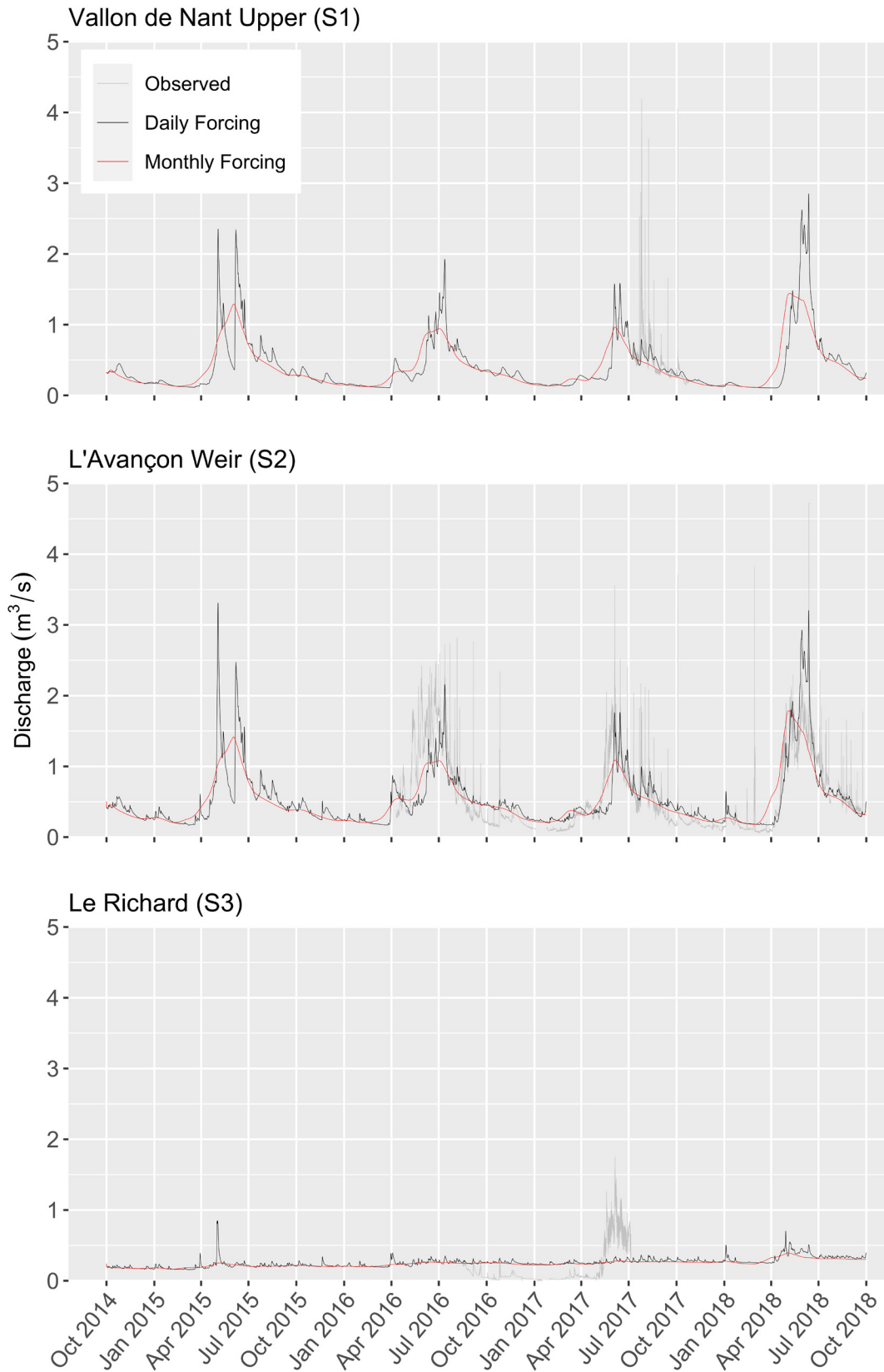


**Figure S8.** The impact of moving from monthly to daily frequency forcing on streamflow predictions generated by the fully-integrated model.

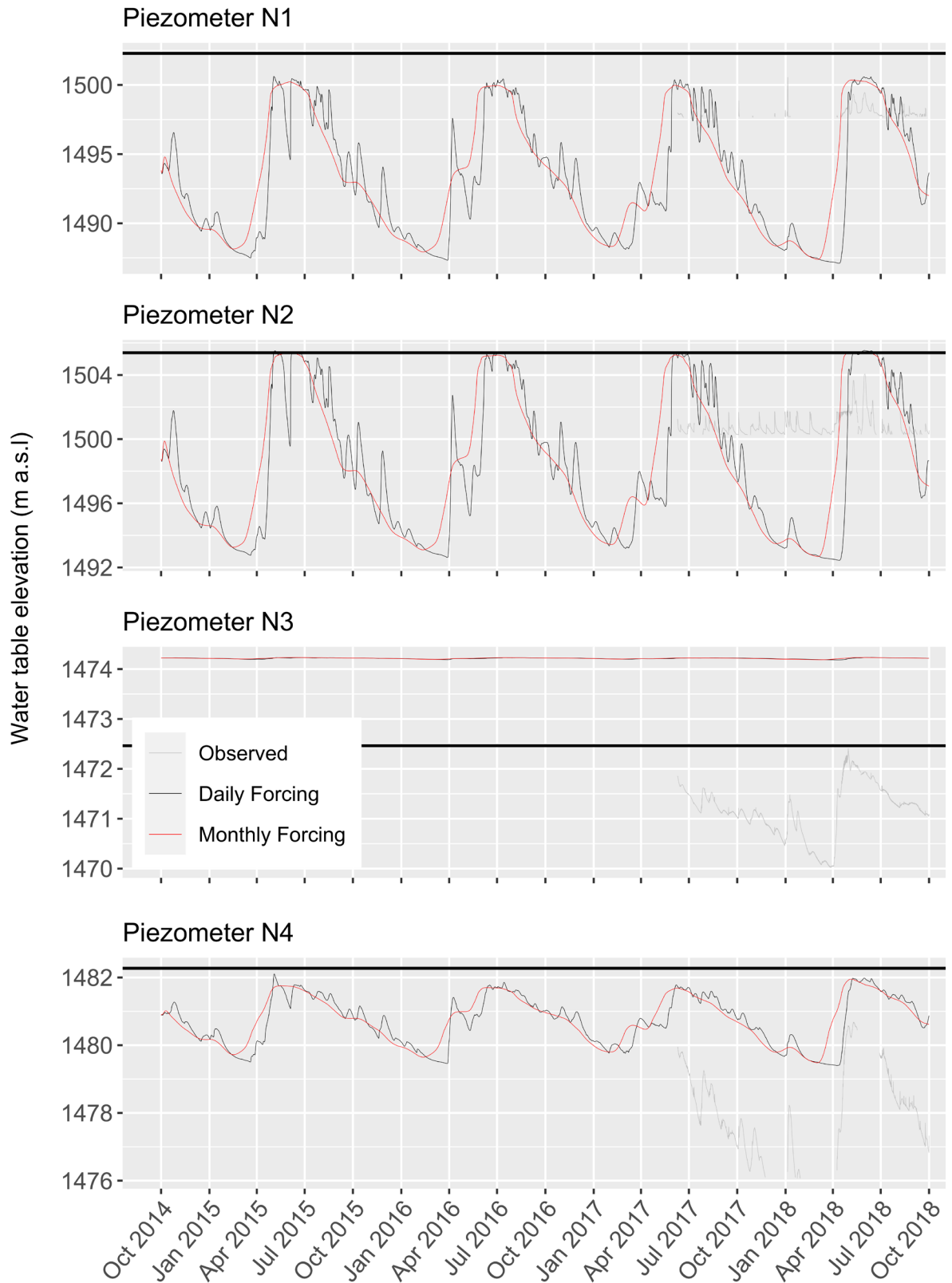


**Figure S9.** The impact of moving from monthly to daily frequency forcing on groundwater level predictions generated by the fully-integrated model.

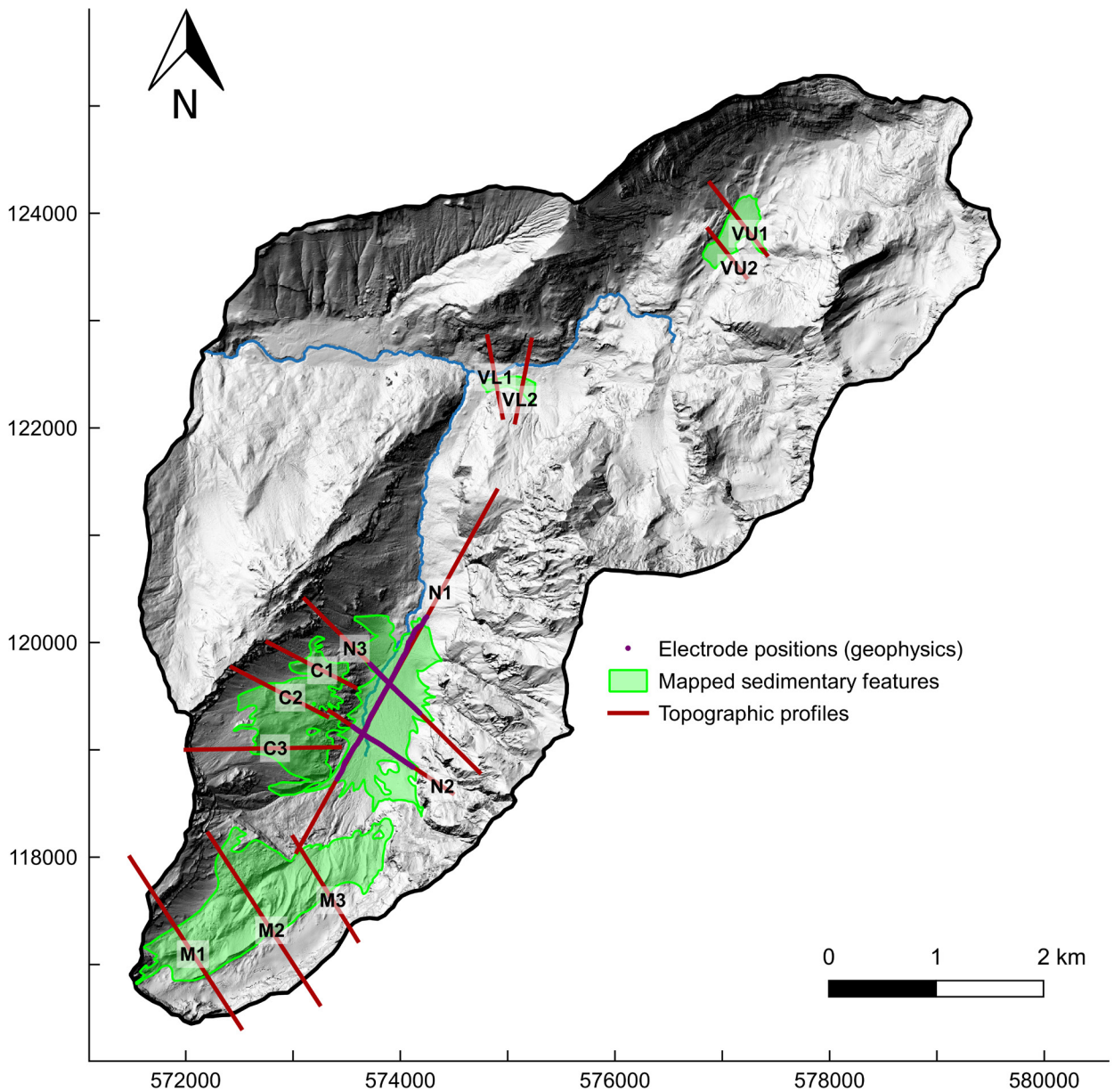


**Figure S10.** The major unconsolidated sedimentary feature extents considered in this study. The locations of electrodes that were placed during the geophysics campaign and the topographical cross-sections that were established as a basis for interpolating the bedrock interfaces are also shown. N denotes *Nant*, M *Martinets*, C *La Chaux*, and VU *Vare Upper*, and VL *Vare Lower*. The underlying hillshade map was generated from the swissALTI<sup>3D</sup> digital terrain model © swisstopo).

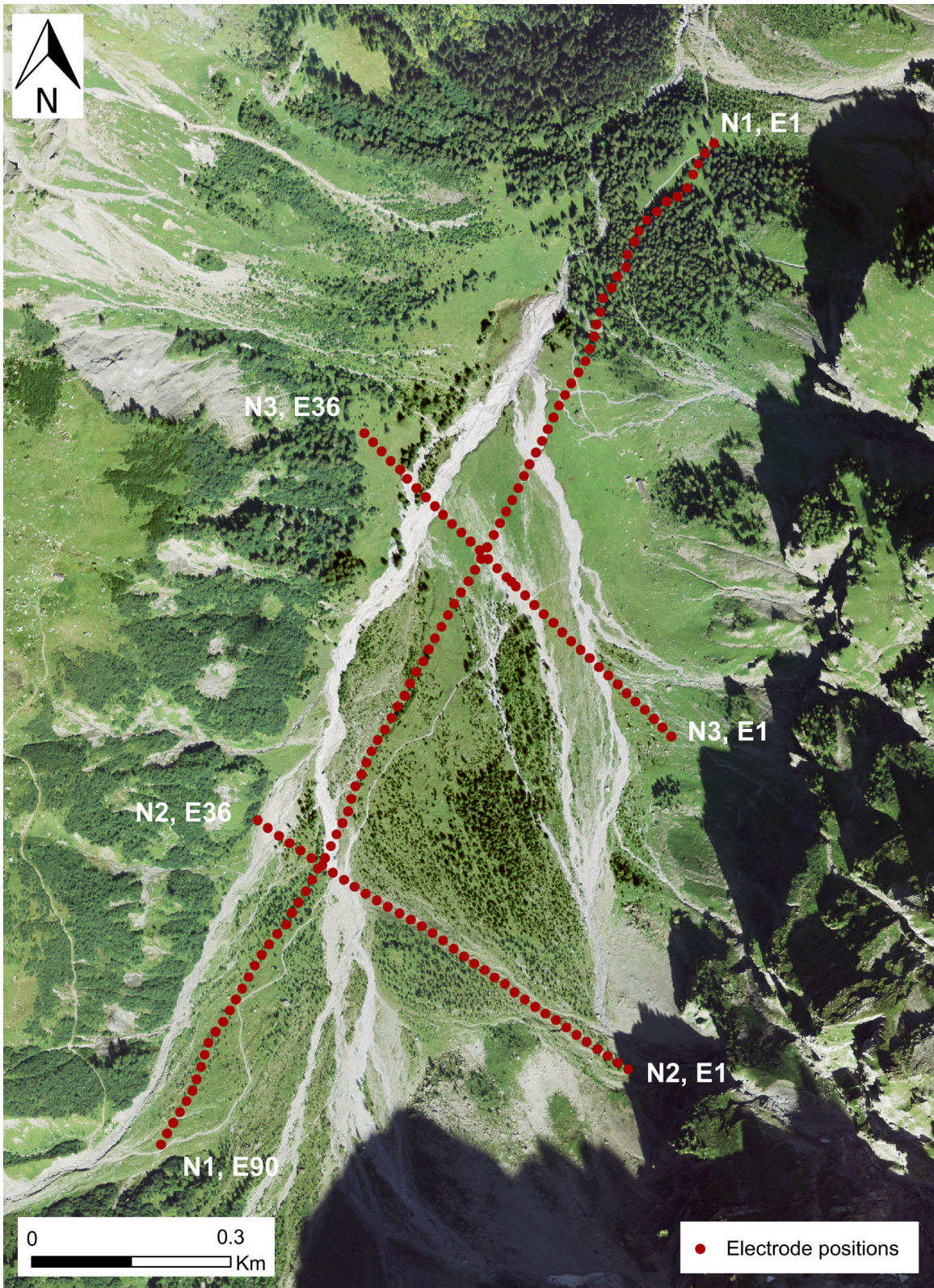


**Figure S11.** The arrangement of electrodes along the three transects in the Nant alluvial fan that were surveyed using electrical resistivity tomography (ERT). The profiles were named N1, N2, and N3, and the electrodes were numbered sequentially along each profile.

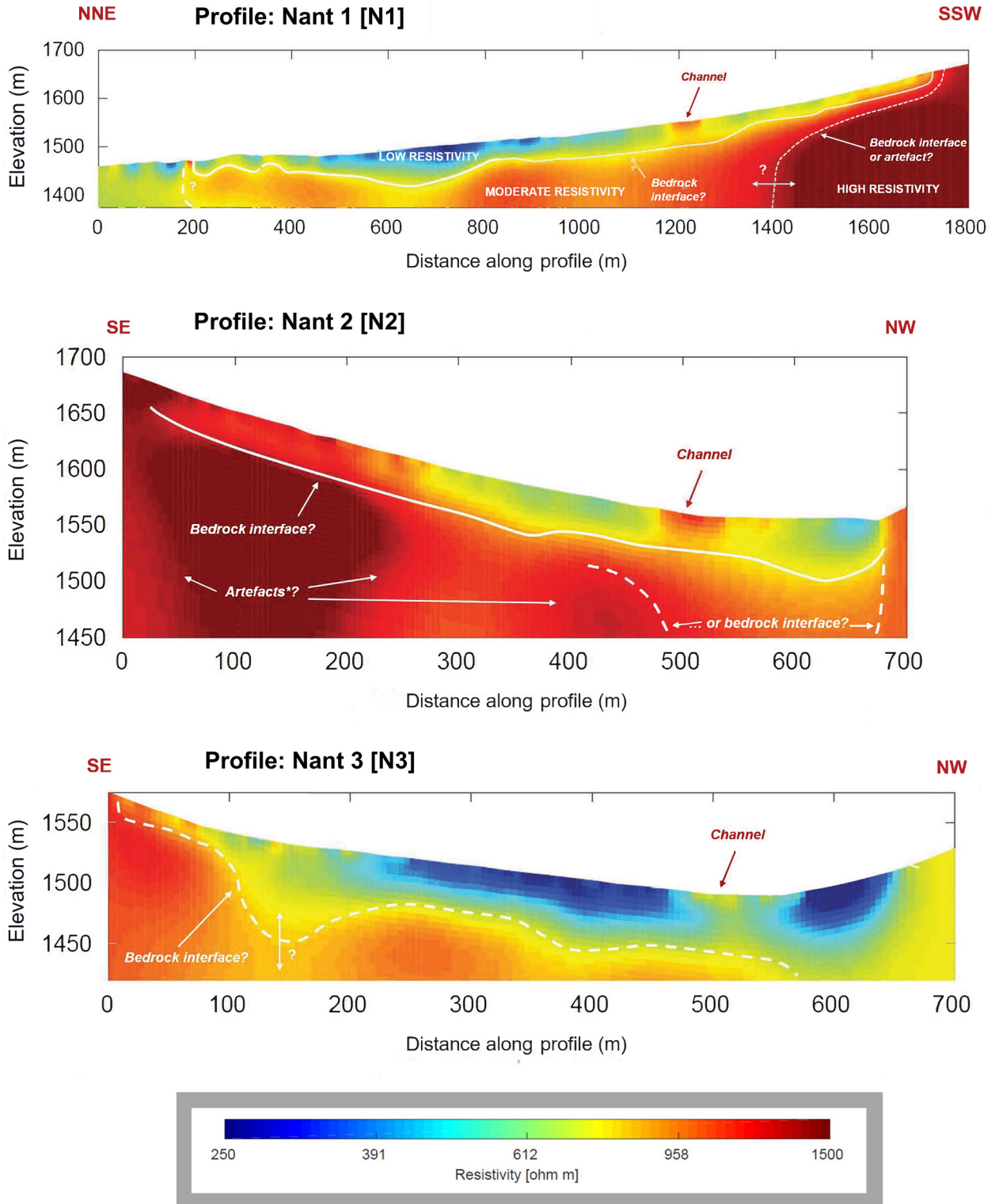
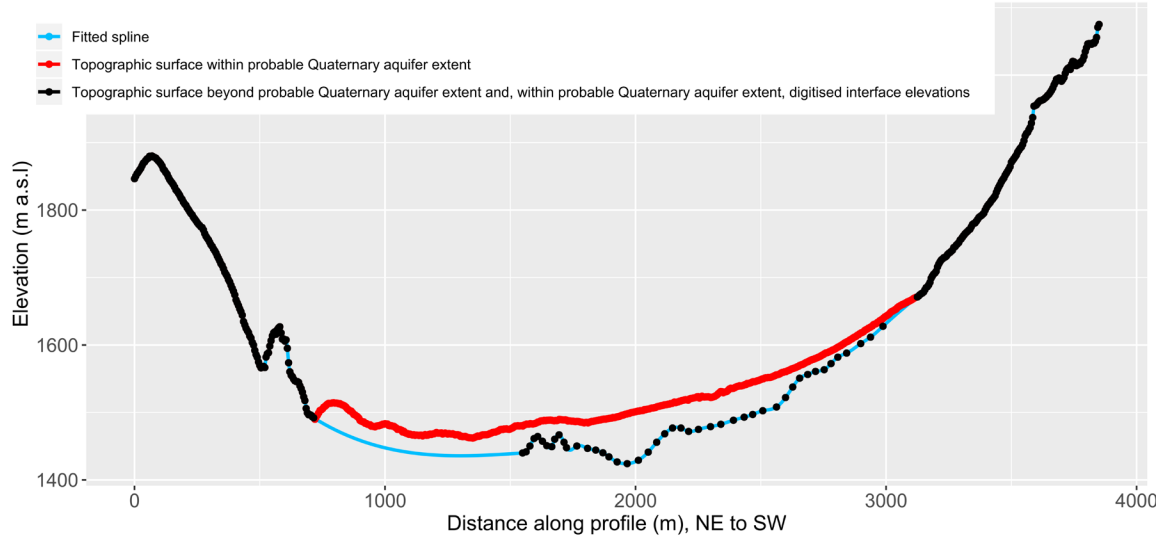
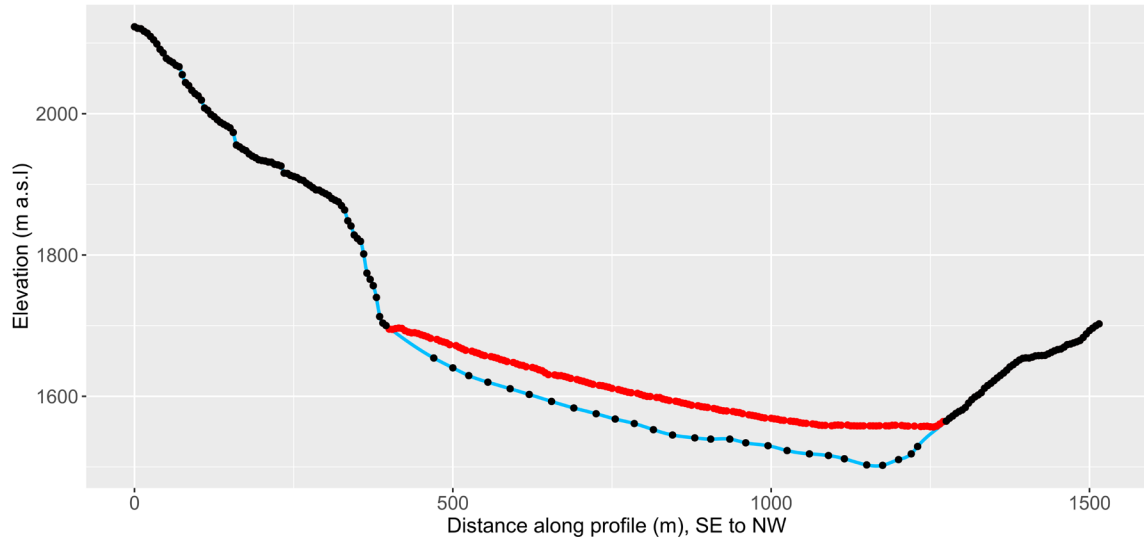


**Figure S12.** Inverted electrical resistivity fields for each of the three surveyed profiles in the Nant alluvial fan. A common resistivity scale is used. Annotations indicate the inferred bedrock interface and other interpretations, which in some cases are only tentative.

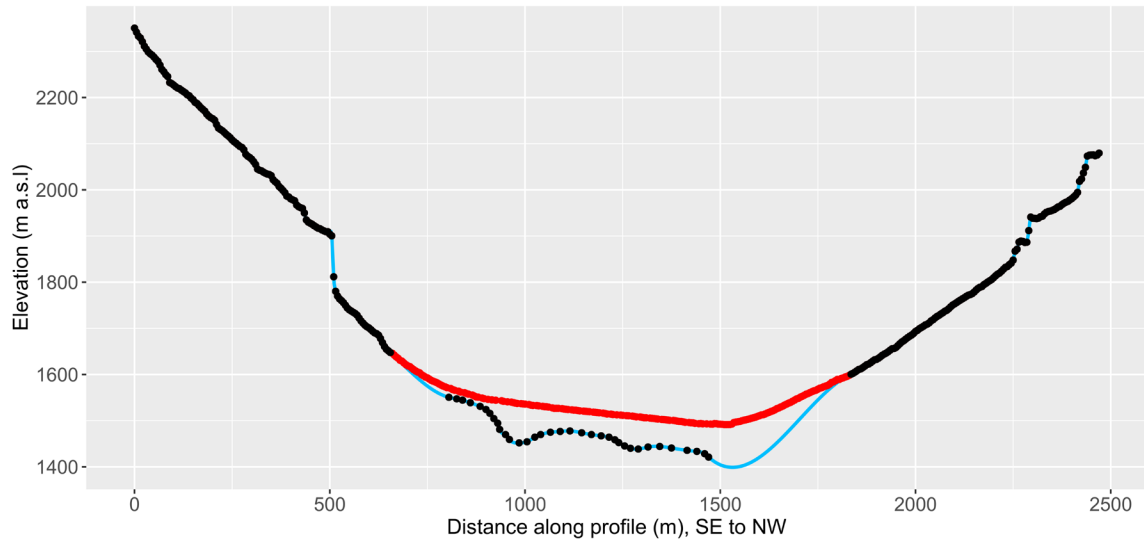
Profile: Nant 1 (GEOelectric) [N1]

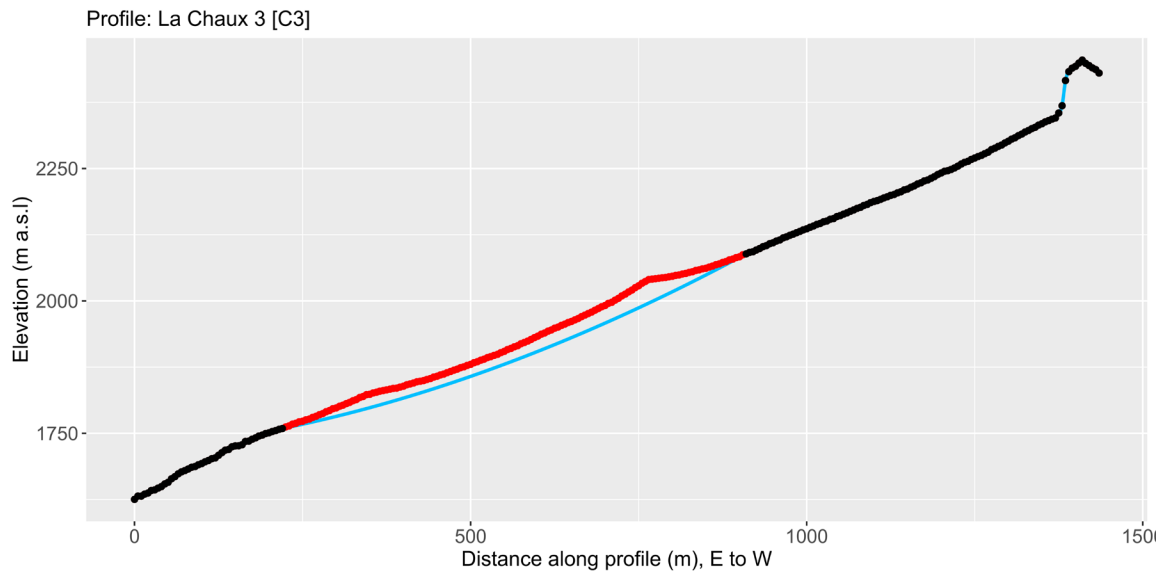
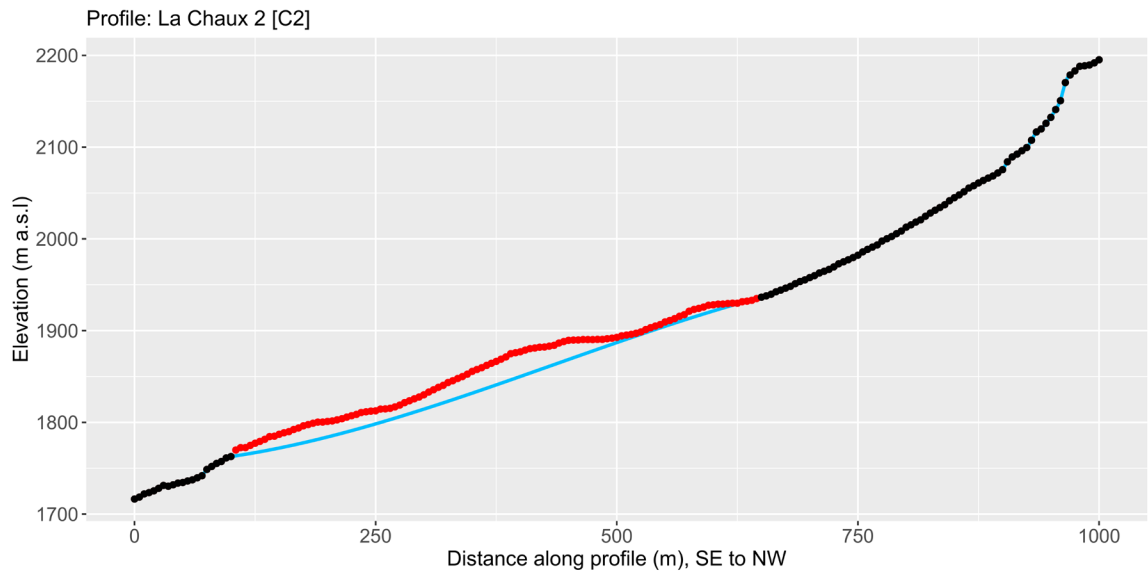
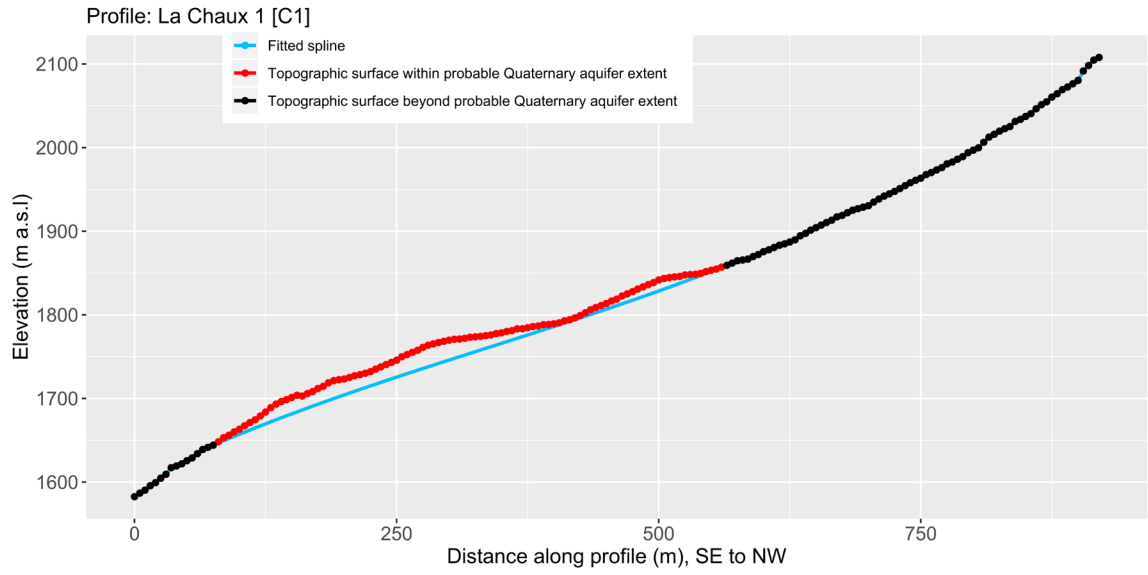


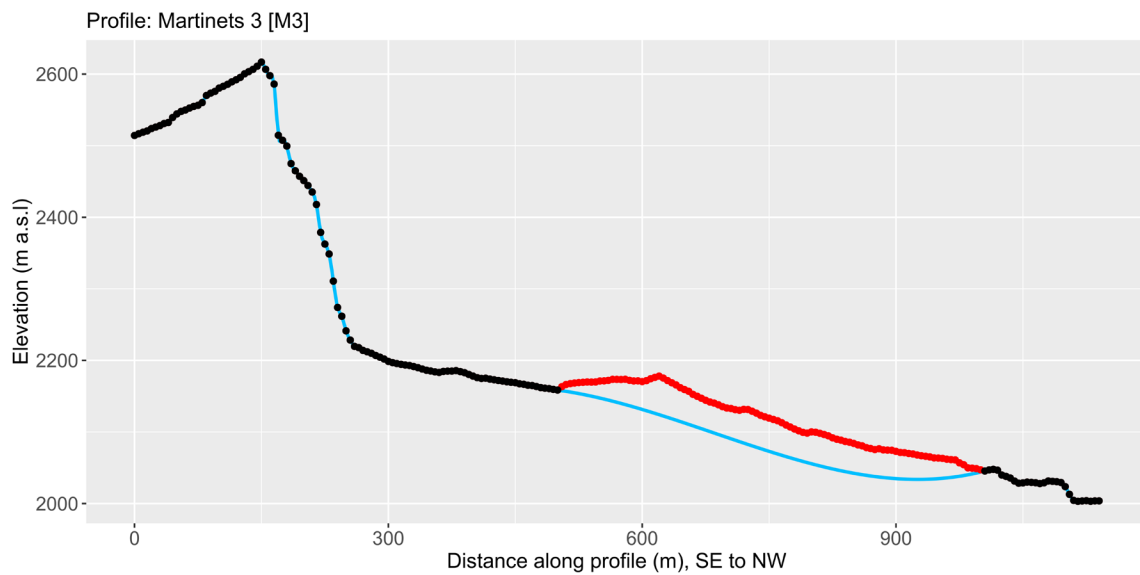
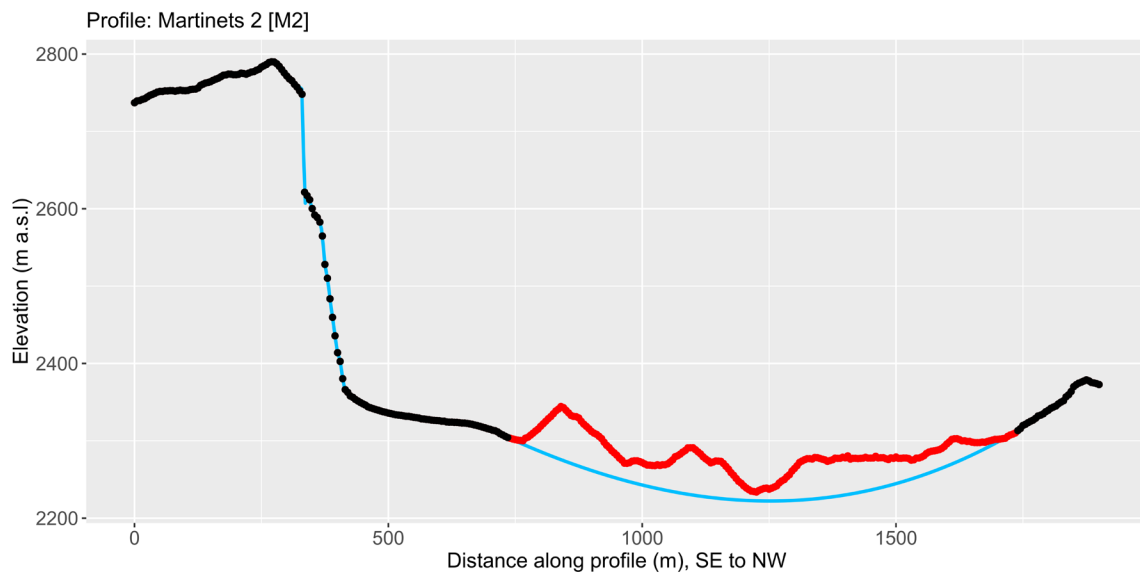
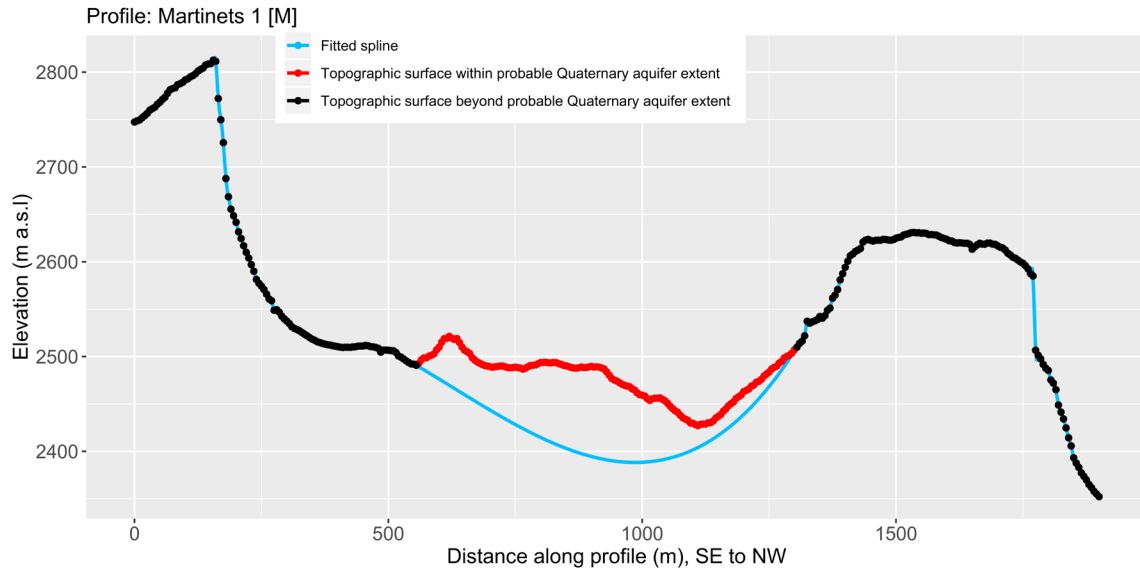
Profile: Nant 2 (GEOelectric) [N2]

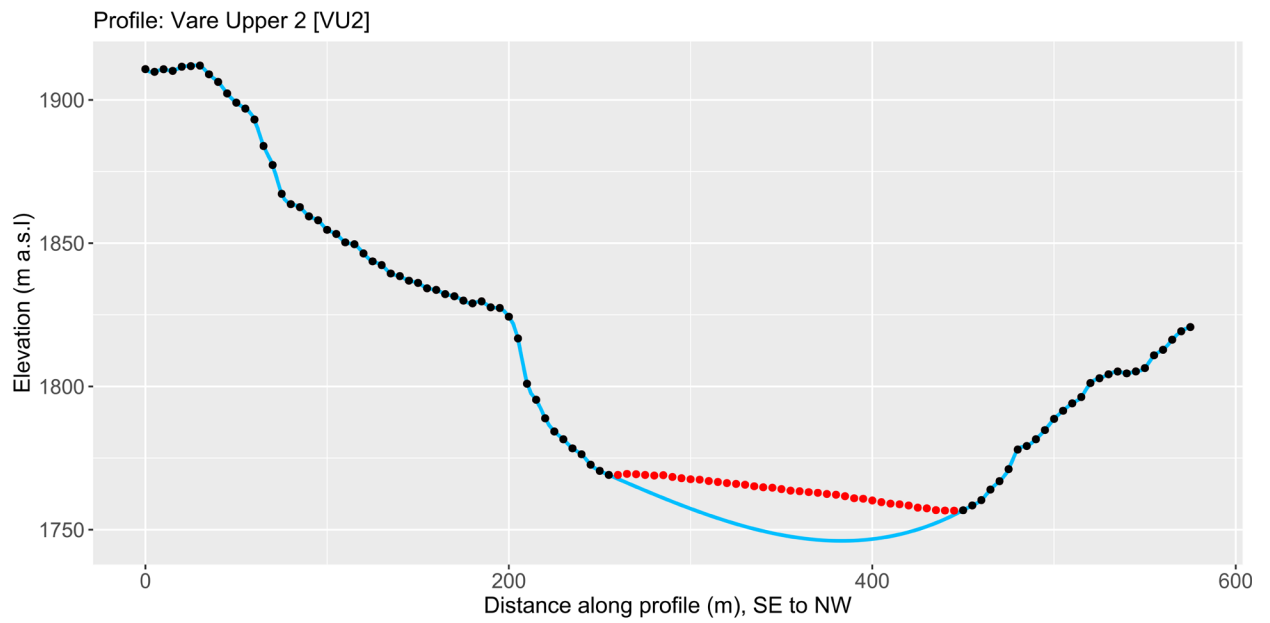
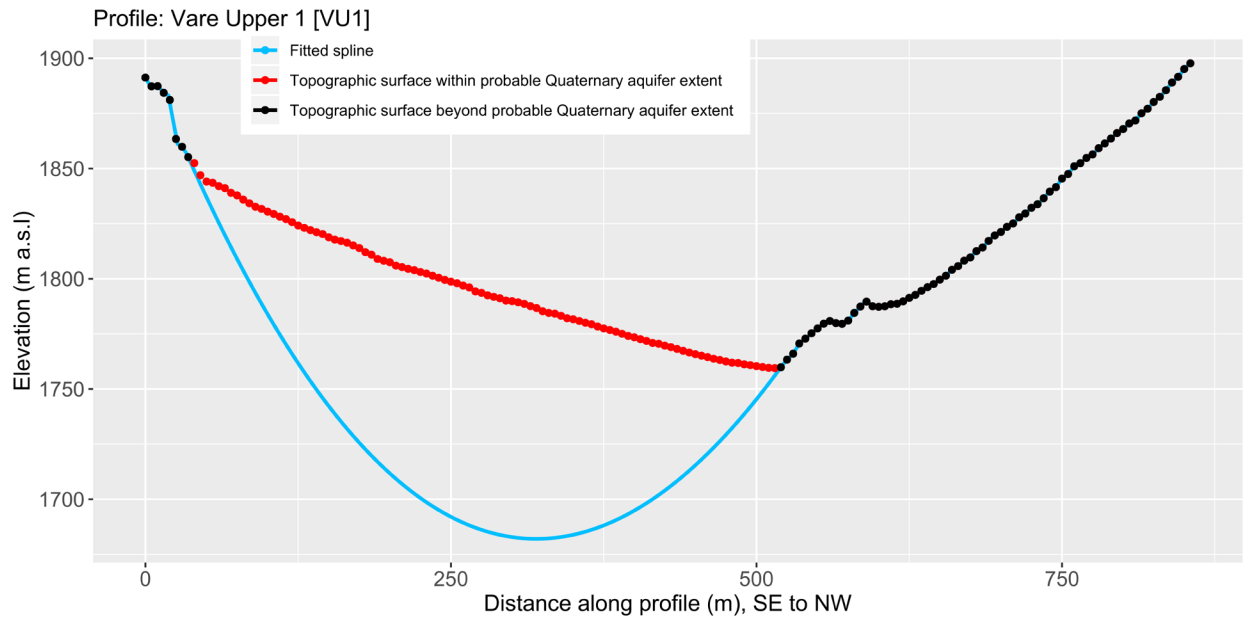


Profile: Nant 3 (GEOelectric) [N3]









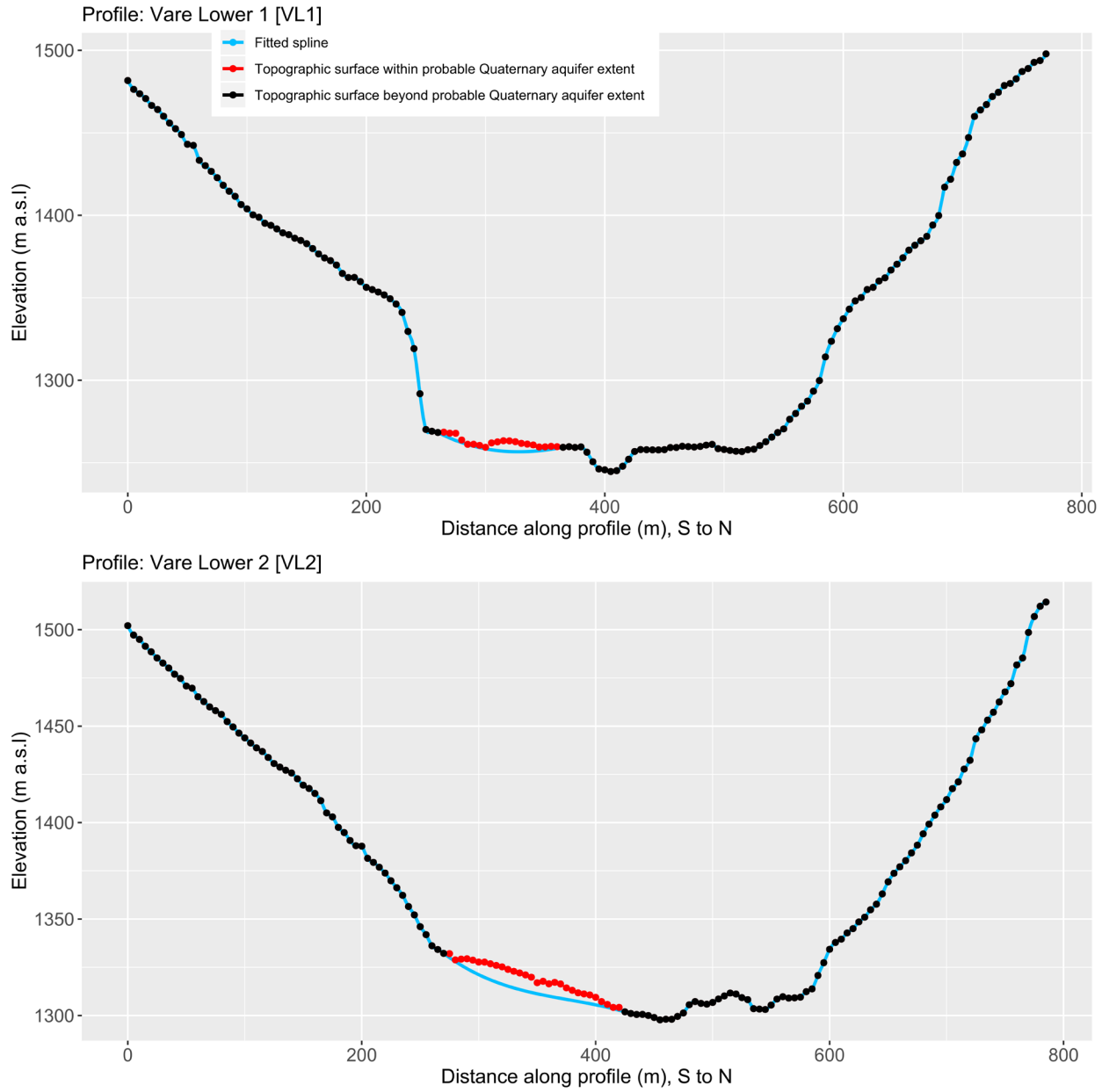


**Figure S13.** Interpolated 2D cross-sections for each of the 13 topographical transects. For the three profiles pertaining to Nant, interfaces derived from the geophysical surveys were included in addition to the topographic points immediately outside the sedimentary features in order to constrain the estimated 2D bedrock interface. Elsewhere, the 2D interpolations were informed solely by the bedrock gradients immediately beyond the sedimentary feature in question.

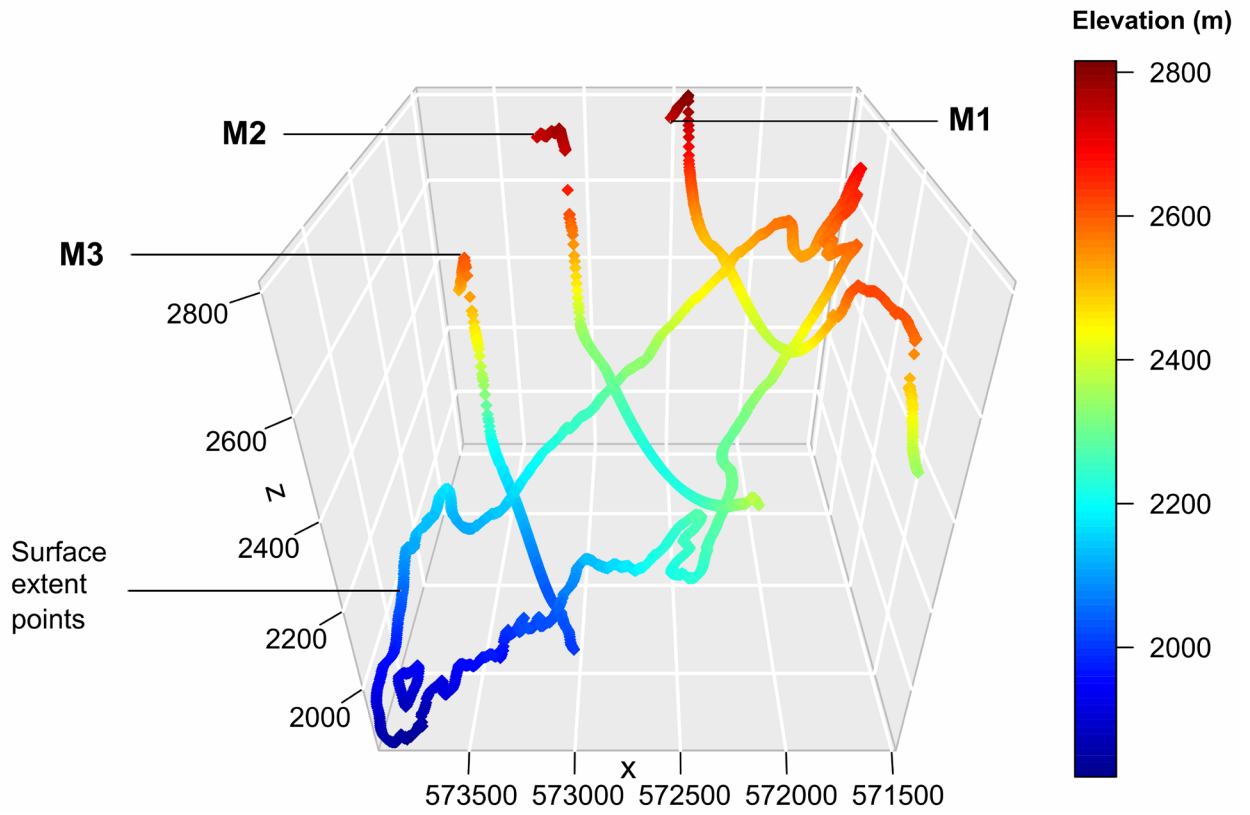


**Figure S14.** 3D points forming the input to the Thin Plate Spline (TPS) interpolation of the bedrock interface beneath the moraines of Les Martinets, looking due south.

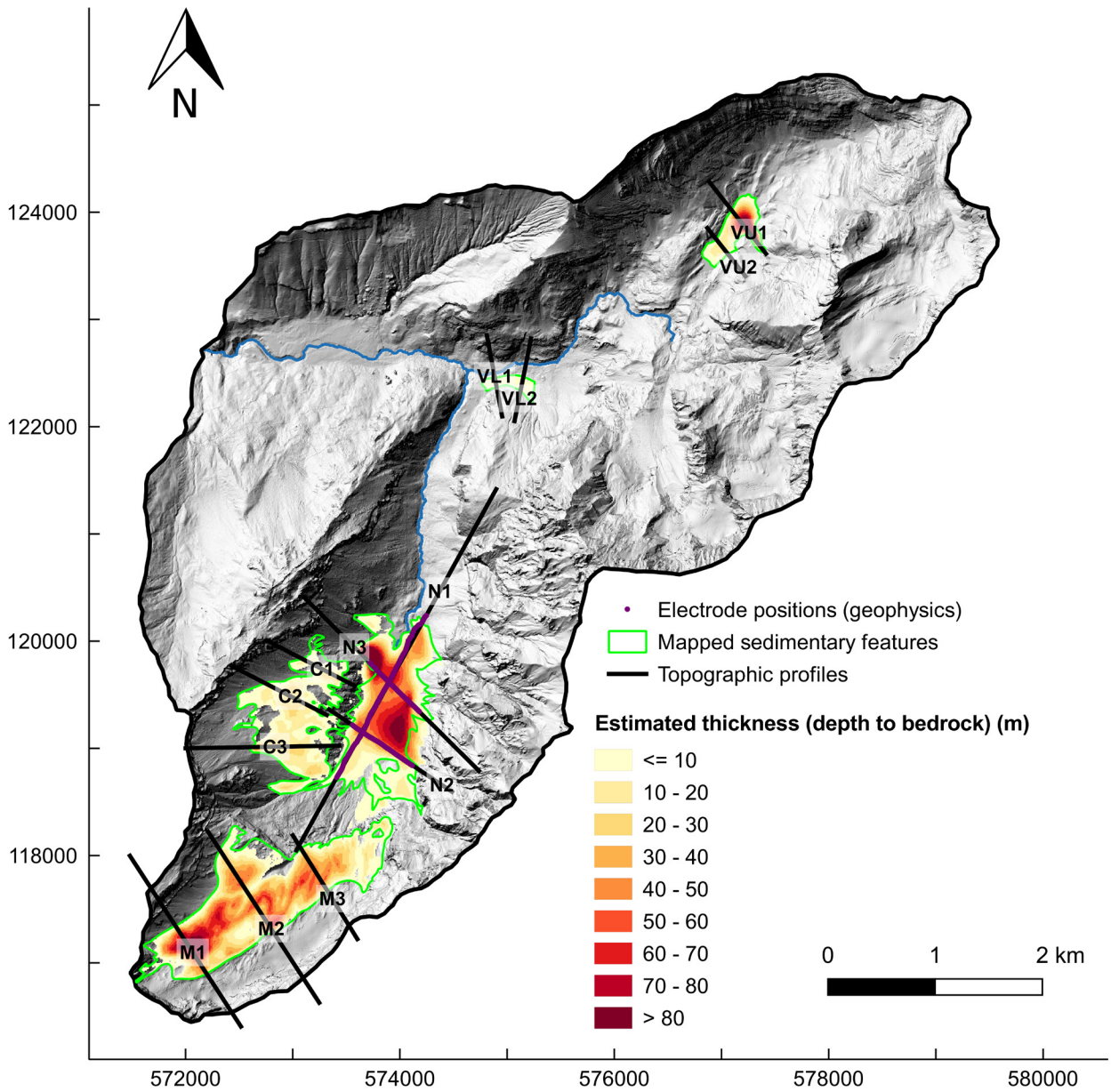


**Figure S15.** Estimated depth to bedrock within unconsolidated sedimentary features that were identified as potentially to host important aquifers. In the case of Nant, the result was generated by combining bedrock interfaces inferred from electrical resistivity images along the three profiles and the results from the geomorphometric method. The remaining features could not be practically surveyed with geophysics, and so the purely desk-based geomorphometric method was used here.

## **Text S1. Estimating geometries of potential unconsolidated Quaternary aquifers**

Recent dedicated field campaigns have elucidated the hydrological importance – in the sense of having the capacity to store and then subsequently release substantial quantities of groundwater – of various individual unconsolidated Quaternary sedimentary features, such as talus slopes, moraines, alluvial fans, and rock glaciers, that are commonly encountered in alpine settings (Hayashi, 2019; Somers & McKenzie, 2020). However, researchers have few practical, cost-effective methods at their disposal to accurately estimate the 3D geometries of several such features across entire rugged, largely inaccessible mountainous headwater catchments. This is problematic because model structures should ideally be constrained as tightly as possible initially in order to limit the potential for parameter values to take on values that compensate for poor structures to reproduce the “right answers”, but for the “wrong reasons” (which could have severe implications for subsequent predictions).

In absence of borehole information, geophysical methods (e.g. Sass, 2006; McClymont et al., 2011, 2012) generally yield the strongest geometrical constraints. Whilst therefore recommendable in principle, they are also very labour intensive. Given this and the fact that the routinely generated resultant data 2D, it is generally not possible to survey more than perhaps one or two such features with sufficient density to provide meaningful 3D insights. In addition, environmental protection measures in sensitive mountain regions may preclude the use of certain geophysical techniques (e.g. seismic methods).

Traditional desk-based geomorphometrical methods, meanwhile, are certainly more efficient across larger areas, but the accuracy of the resultant estimate may be compromised, especially in light of the distinctive characteristics of alpine terrain. Several geomorphometrical approaches to estimating the sediment/bedrock interface along 2D cross-sections perpendicular to the main valley axis have been considered. Perhaps the most straightforward approach involves simply projecting hillslope gradients into the subsurface (Hinderer, 2001). The fitting of power laws (Svensson, 1959) and quadratic functions (Wheeler, 1984) to empirical cross-section data have also proved rather popular (James, 1996; Li et al., 2001), even if much of this work was undertaken in attempts to try to better understand valley formation processes, whereby the fitted parameter values are interpreted (e.g. a power law exponent,  $b$ , approaching two is taken to be indicative of parabolic “U-shaped” glacial valleys, whilst values closer to one are considered to signify fluvially-incised “V-shaped” valleys), rather than current geometries.

Nevertheless, if elevation points along the profiles corresponding to the sedimentary fill are removed prior to curve fitting, erosional upper bedrock surfaces can be reconstructed (Harbor & Wheeler, 1992). A fairly dense array of cross-sections must usually be considered to capture any longitudinal variability in the 2D profiles, and a final interpolation undertaken to produce a 3D result. Schrott et al. (2003), for instance, took such an approach in a small catchment in the Bavarian Alps, Germany, but found that the surfaces produced by polynomial fitting overestimated sediment thicknesses compared to coincident seismic refraction surveys. Not dissimilarly, Rogger et al. (2017) used a geomorphometrical approach to augment geophysical insights; sediment thicknesses were estimated at many different cross-sections by “extending the bare rock surface below the sediment deposit through a parabola fitted to the bedrock slopes at the outcrop boundaries”.

Major drawbacks have been identified with both the power law and quadratic methods, however (Harbor & Wheeler, 1992; Pattyn & Van Huelé, 1998). Specifically, power law functions must be fitted to both sides of a given valley cross-section independently, since the variable representing horizontal distance cannot take negative values. Additionally, power law functions must pass through the origin of the coordinate system used, yet where this location should be is generally unknown at the outset – above all when the very aim is to interpolate the bedrock surface beneath sedimentary fill deposits. This issue renders the results sensitive

to the choice of origin. The logarithmic transformation that is typically applied to solve for the constants of power law equations compounds the problem, since it causes more weight to be placed upon those points located near the origin than those towards the profile's extremities. Quadratic functions, meanwhile, assume that the cross-sectional form is parabolic and symmetrical, and are hence poorly suited to representing any form of asymmetry in such profiles.

A more modern but related approach to the estimation of glacial valley bedrock forms is the Sloping Local Base Level (LSBL) method (Jaboyedoff & Derron, 2005). This technique requires a digital terrain model (DTM) as input. Via the iterative calculation of quadratic parabolas, the topographic surface within the region of sedimentary fill is then progressively "excavated", leaving a curved 3D bedrock surface. A crucial impediment to the wider implementation of this technique is that the maximum expected depth to bedrock, must be specified *a priori* (Otto et al., 2009), yet this is typically a key unknown to be determined. More recently, Mey et al. (2015) presented an approach to the estimation of valley fill thickness/bedrock surface topography that revolves around training a machine learning algorithm using geometrical landscape data – specifically, the sectoral distance to the nearest bedrock hillslope, with the training data being generated by artificially filling DTMs. The approach hinges on the morphological similarity of the hillslope above the valley fill and the bedrock interface beneath it. Whilst results were promising with respect to estimating the thicknesses of sediments stored in the floor of large, almost horizontal intermontane valleys, the method would appear to be less immediately applicable to smaller alpine headwater catchments with their steeper sloping deposits.

As this last point alludes to, a further limitation of all the aforementioned geomorphometrical methods – and one which is particularly important given the complex nature of the bedrock geology at the present study site – is that geometric similarity above and below the fill level is assumed. In other words, no account is taken of lithological contrasts which, where present, bring about discontinuities in the cross-sectional profiles and terrain morphology more generally. The geostatistical approach developed by Castilla-Rho et al. (2014) used splines – a geomorphometrical technique that is better able to account for cross-sectional variability – in conjunction with various other datasets to estimate the bedrock interfaces of fluvial valleys.

As a consequence of these issues, it remains challenging to establish the extent to which the combination of these unconsolidated features contributes to the hydrological functioning of the broader catchment systems within which they are embedded, including their contributions to streamflow. Indeed, in integrated and other similar numerical model applications in mountainous areas, it remains common to rely on extremely simplified representations of potential unconsolidated aquifers (e.g. spatially uniform thicknesses) to be applied (Florincic et al., 2018; Smoorenburg, 2015).

From this brief review, it seems unlikely that any ideal solution to this challenge presently exists, and that a combination of a geomorphological approach with constraints from geophysics might therefore represent a pragmatic compromise. As such, with a view to informing development of the integrated model described in the main paper, a simple 2D and 3D spline-based geomorphometrical approach involving the targeted extraction of digital terrain and geological map data is presented. This is fairly similar to the approach of Castilla-Rho et al. (2014), but without stochastic quantification of uncertainty (which fell beyond our scope). It is shown that, where available, bedrock interface constraints inferred from geophysics – in the case of an electrical resistivity tomography (ERT) survey – can easily be incorporated. Ultimately, it is hoped that the approach provides a means by which catchment-scale groundwater and integrated surface-subsurface model structures can be refined compared to present practices.

The first step of the methodology involved identifying any major sedimentary features with the potential to act as aquifers (i.e. can store and subsequently release meaningful quantities of water) and establishing their

surficial extents. This step required some general understanding of the hydrogeological system – especially qualitative knowledge of where the major aquifers are located. This understanding was developed by basic field measurements and reviewing various existing datasets.

More specifically, feature identification placed reliance on existing detailed (pre-digitised) surface geological maps (the swisstopo GeoCover25 dataset; [https://shop.swisstopo.admin.ch/en/products/maps/geology/GC\\_VECTOR](https://shop.swisstopo.admin.ch/en/products/maps/geology/GC_VECTOR)) and a high (2 m) resolution terrain “hillshade” map which was developed from the swissALTI<sup>3D</sup> dataset ([https://shop.swisstopo.admin.ch/en/products/height\\_models/alti3D](https://shop.swisstopo.admin.ch/en/products/height_models/alti3D)). Unconsolidated sedimentary deposits were marked on the geological maps, and are furthermore clearly discernible in the “hillshade” map. Previous studies pertaining to the hydrogeological function of certain types of features (e.g. proglacial moraines) were also consulted as necessary. In this way, the following five principal features were identified:

- A large alluvial fan system, referred to henceforth as *Nant*;
- High proglacial moraine sediments of the Glacier des Martinets – *Les Martinets*;
- Glacial drift sediments – *La Chaux*;
- Generic unconsolidated fill sediments in a karstic, topographically closed depression (i.e. a doline) – *Vare Upper*, and;
- Generic unconsolidated fill sediments – *Vare Lower*.

These five features were treated as distinct zones so that in the subsequent integrated model, different hydraulic properties reflecting their specific histories and constituent materials could be assigned to each in the integrated flow model. The spatial extents of these features were extracted as shapefiles from the GeoCover25 maps and verified with reference to the hillshade map. The resultant areas are presented in Figure S10. In a final preliminary step, the  $x, y$ , and surface elevation,  $z$ , attributes of points spaced at 5 m intervals along the feature boundaries (i.e. where sediment thickness = 0) were extracted from the DTM, and the resultant coordinate triplets recorded along with an identifier of the feature to which they correspond.

As previously discussed, in seeking to estimate Quaternary aquifer geometries, as much geophysics as possible should ideally be conducted. That said, the practical and monetary constraints to such approaches are elevated in rugged alpine terrain. With such considerations in mind, and within the very broad scope of this study, only one geophysical technique could be deployed here, and only a single unconsolidated formation surveyed. Since the main alluvial fan in the central part of the Vallon de Nant (i.e. Nant) was believed to constitute the most important unconsolidated formation in hydrological terms, attention was focussed here. This feature also happened to be comparatively accessible; having obtained the necessary special permissions, off-road vehicular access was possible as far as Chalet Nant – a now uninhabited farm building in the alpine pasture.

The survey’s primary objective was to determine the spatial distribution of depth to bedrock; any potential insights that could be gleaned with regards to internal structure would be considered a bonus. Seismic methods (used by Schrott et al., 2003, amongst many others) were discounted due to the Natural Reserve’s regulations, whilst the depth of information provided by ground-penetrating radar is too limited. Finally, we decided to rely on ERT, which we expected could provide information about the lithological structure down to depths ~100-200 m. A four-day long field campaign was conducted in favourable meteorological (dry and sunny conditions) in September 2018 – the first attempt to image the subsurface of this pristine Alpine valley.

With the objectives in mind, the intended profile layouts and electrode spacings were planned in advance. Three separate profiles were identified; one long one of 1,780 m running approximately parallel to the main valley axis (N1), and two shorter perpendicular profiles of 700 m each (N2 and N3) (Figure S11). The former

sought to capture any longitudinal variability in the bedrock interface (i.e. along the valley axis), for instance due to glacial over-deepening, which is common in such settings. The two intersecting transverse profiles sought to provide some 3D constraints on the morphology of the upper bedrock surface (and hence the unconsolidated sediment thickness); the ultimate goal being to develop a 3D flow model after all. In order to image comparatively deep, a 20-m electrode spacing was chosen.

Once in the field, where conditions allowed, the stainless-steel electrodes were hammered in to a depth of 10-20 cm. The length of N1 necessitated a “roll-along” technique. At locations without soil cover (see e.g. Figure 4.8b), electrodes were positioned firmly in the silty sediments between larger boulders and pebbles, and sponges dampened with salt water were applied to decrease the contact resistance. Typically, contact resistances between electrodes of less than 5 kOhm were achieved. The electrode positions were measured accurately using a Leica Differential GPS device; these are plotted in Figure S11. Relatively straight profiles could be maintained, and so any corresponding 3D distortive effects in the results should be minimal.

The apparent resistivity measurements were acquired in both dipole-dipole and Wenner-Schlumberger configurations using an IRIS Syscal Pro instrument. The current injection cycles (500 ms) were repeated four times and the measurements were stacked in order to improve the signal-to-noise ratios. Prior to inversion, the data from the Wenner-Schlumberger and dipole-dipole surveys were combined, giving a total of 3,353 measurements for N1, and 793 measurements for N2 and N3, before any measurements whose standard deviation exceed 3% were removed. The inversions were performed in a fairly standard fashion using the code BERT (Günther, Rücker and Spitzer, 2006). Robust data reweighting and compact inversion using iteratively-reweighted least-squares were employed to reduce the influence of outliers and to image sharper interfaces, respectively. The inversion process converged in 10 iterations, with a final relative root-mean square error of <5%.

The three resultant resistivity images (Figure S12) were interpreted both independently and in combination. To facilitate the latter, they were georeferenced and visualised in conjunction with the surface topography within a virtual environment (Movie 3). This step also enabled the coherence of the inversion results near the profiles’ intersection points to be verified. Next, a plausible bedrock interface was tentatively identified and annotated on the images (along with other possible interpretations). Finally, the spatial coordinates ( $x,y,z$ ) of points placed at regular intervals along the identified subsurface interface were extracted.

The next phase of the methodology was to make a series of 2D interpolations at the various cross-sections. To achieve this, the geophysical transects and other topographical profiles were first extended, points were generated at 5 m intervals along the full profiles, the surface elevation ( $z$ ) extracted from the DTM, and the horizontal distance from the respective profile start points calculated. Then, for each feature independently, the surface elevation points were plotted against the horizontal distances, and any points falling within the unconsolidated sediment extents (identified via spatial intersection with the feature shapefiles) were removed. These points are represented in red in Figure S13.

Following that, cubic splines were fitted to interpolate between the remaining points. As a class of functions, splines are local interpolators which seek to fit the empirical data points exactly (or extremely closely, by minimising the sum of the squared residuals) whilst simultaneously maximising smoothness, by penalising roughness (Mitas and Mitasova, 1999). They are generally favoured over high-order polynomials because the latter can result in strong oscillations. The specific technique of cubic spline fitting involves establishing piecewise third-order polynomials that pass through all of the control points. In this way, the upper bedrock surfaces along each transect were estimated. For the three profiles in the *Nant* feature, the additional subsurface interface derived from the geophysics results were included in the 2D interpolations in the same fashion as the topographic points beyond feature extents.

The smoothness of the resultant interpolations makes splines well-suited to the task of reconstructing “U-shaped” glacial valleys; the smooth interfaces they propose beneath the sediment-obscured regions correspond to the simplest possible models. Simultaneously, in being able to follow sharp elevation discontinuities in the bedrock outcrops, which arise here due to lithological contrasts, these points do not influence the reconstructed interfaces. In other words, the upper bedrock surface estimates along each transect were consistent with the bedrock gradients immediately beyond the feature extents. It follows that should any lithological “steps” occur beneath the zones of sediment fill, these would not be captured. Such “steps” are generally not too problematic in this case, however.

In certain instances, the interpolated interfaces did demonstrate a fairly high degree of sensitivity to the elevation gradients immediately beyond the sedimentary feature extents, and hence to the inclusion/exclusion of sampled points near the sediment/bedrock interfaces. This is similar to the finding of Mey et al. (2015), who also noted a certain sensitivity to the accuracy of the mapped feature “mask”. In fact, here, there was no hard condition to stipulate that the resultant interpolated surface should remain beneath the topographic surface. That said, the original surficial extent mapping (and hence the distinction between which points lay within the unconsolidated region and which lay beyond it) was certainly not perfect. This observation justified the manual additional removal of a few points in certain cases in these boundary regions, leading to interface profiles that were i) more consistent with prior expectations, and ii) were sufficiently coherent with others in the same feature. The final resultant splines are shown as the light blue lines in Figure S13.

The surface coordinates (i.e.  $x,y$ ) of regular points along the interpolated spline function beneath the sedimentary fill were calculated using trigonometry and recorded along with the elevation estimates ( $z$ ). Finally, the triplets ( $x,y,z$ ) were grouped by feature, and pooled with the corresponding surficial extent triplets (i.e. where thickness = 0) that had been generated already. For illustration, Figure S11 shows all points prior to 3D interpolation for the *Les Martinets* feature.

Finally, the 3D interpolations could be undertaken. For each feature independently, all 3D (i.e.  $x,y,z$ ) points which corresponded to an observed or estimated sediment thickness of zero (i.e. the bedrock interface) were interpolated using Thin Plate Spline (TPS) functions – which imitate thin steel sheets forced to pass through the points – to give a spatially continuous 3D surface (with 10 m horizontal resolution). The smoothing parameter was identified automatically by generalised cross-validation. Where necessary, the resultant raster dataset was clipped to the feature boundaries. The final estimated unconsolidated sediment thickness distribution is shown in Figure S12.

Given the relative ambiguity of the bedrock interface from the geophysical results (essentially due to their being no strong contrasts in resistivity – the clay rich Flysch bedrock apparently having fairly similar properties to the unconsolidated materials), as well as the potential for the internal structure, which could not be determined using the large electrode-spacing used here, having potentially high hydrological importance (for instance, a very shallow clay layer could be observed in the field in regions of the main alluvial fan aquifer at *Nant* after an erosive flow event), the entire depth to bedrock beneath the alluvial fan was not defined as being eminently permeable for the purposes of the subsequent numerical modelling. Instead, only the upper third of the total thickness was considered as such, with the lower permeability till/clay assumed to comprise the remaining volume. This is essentially akin to defining the alluvial fan base according to a lower resistivity isosurface than the bedrock interface in S12; somewhere in the light blue region. Such an approach is justified by the fact the ERT appears to be mapping the fan and the till as a common low-resistivity feature above the bedrock interface. The technique is also known to have a tendency to somewhat overestimate the size of conductive anomalies – in this case the coarse gravel region of the fan. Since the

geomorphometrical method provided no insight whatsoever in the other formations, they were assumed “hydrologically active” to their full depth.

For an extended description of the method and results, readers are directed to Chapter 4 of Thornton (2020). This doctoral thesis is currently under embargo but can be provided confidentially by the corresponding author upon written request.

### References

- Castilla-Rho, J. C., Mariethoz, G., Kelly, B. F. J., & Andersen, M. S. (2014). Stochastic reconstruction of paleovalley bedrock morphology from sparse datasets. *Environmental Modelling and Software*, *53*, 35–52. <https://doi.org/10.1016/j.envsoft.2013.10.025>
- Floriantic, M. G., van Meerveld, I., Smoorenburg, M., Margreth, M., Naef, F., Kirchner, J. W., & Molnar, P. (2018). Spatio-temporal variability in contributions to low flows in the high Alpine Poschiavino catchment. *Hydrological Processes*, *32*(26), 3938–3953. <https://doi.org/10.1002/hyp.13302>
- Günther, T., Rücker, C., & Spitzer, K. (2006). Three-dimensional modelling and inversion of dc resistivity data incorporating topography - II. Inversion. *Geophysical Journal International*, *166*(2), 506–517. <https://doi.org/10.1111/j.1365-246X.2006.03011.x>
- Harbor, J. M., & Wheeler, D. A. (1992). On the mathematical description of glaciated valley cross sections. *Earth Surface Processes and Landforms*, *17*(5), 477–485. <https://doi.org/10.1002/esp.3290170507>
- Hayashi, M. (2019). Alpine Hydrogeology: The Critical Role of Groundwater in Sourcing the Headwaters of the World. *Groundwater*, gwat.12965. <https://doi.org/10.1111/gwat.12965>
- Hinderer, M. (2001). Late quaternary denudation of the alps, valley and lake fillings and modern river loads. *Geodinamica Acta*, *14*(4), 231–263. <https://doi.org/10.1080/09853111.2001.11432446>
- Jaboyedoff, M. I., & Derron, M. . (2005). A new method to estimate the infilling of alluvial sediment of glacial valleys using a sloping local base level. *Geografia Fisica e Dinamica Quaternaria*, *28*, 37–4.
- James, A. L. (1996). Polynomial and power functions for glacial valley cross-section morphology. *Earth Surface Processes and Landforms*, *21*(5), 413–432. [https://doi.org/10.1002/\(SICI\)1096-9837\(199605\)21:5<413::AID-ESP570>3.0.CO;2-S](https://doi.org/10.1002/(SICI)1096-9837(199605)21:5<413::AID-ESP570>3.0.CO;2-S)
- Li, Y., Liu, G., & Cui, Z. (2001). Glacial valley cross-profile morphology, Tian Shan Mountains China. *Geomorphology*, *38*(1–2), 153–166. [https://doi.org/10.1016/S0169-555X\(00\)00078-7](https://doi.org/10.1016/S0169-555X(00)00078-7)
- McClymont, A. F., Hayashi, M., Bentley, L. R., & Liard, J. (2012). Locating and characterising groundwater storage areas within an alpine watershed using time-lapse gravity, GPR and seismic refraction methods. *Hydrological Processes*, *26*(12), 1792–1804. <https://doi.org/10.1002/hyp.9316>
- McClymont, Alastair F., Roy, J. W., Hayashi, M., Bentley, L. R., Maurer, H., & Langston, G. (2011). Investigating groundwater flow paths within proglacial moraine using multiple geophysical methods. *Journal of Hydrology*, *399*(1–2), 57–69. <https://doi.org/10.1016/j.jhydrol.2010.12.036>
- Mey, J., Scherler, D., Zeilinger, G., & Strecker, M. R. (2015). Estimating the fill thickness and bedrock topography in intermontane valleys using artificial neural networks. *Journal of Geophysical Research: Earth Surface*, *120*(7), 1301–1320. <https://doi.org/10.1002/2014JF003270>
- Otto, J.-C., Schrott, L., Jaboyedoff, M., & Dikau, R. (2009). Quantifying sediment storage in a high alpine valley (Turtmanntal, Switzerland). *Earth Surface Processes and Landforms*, *34*(13), 1726–1742.

<https://doi.org/10.1002/esp.1856>

- Pattyn, F., & Van Huele, W. (1998). Power law or power flow? *Earth Surface Processes and Landforms*, 23(8), 761–767. [https://doi.org/10.1002/\(SICI\)1096-9837\(199808\)23:8<761::AID-ESP892>3.0.CO;2-K](https://doi.org/10.1002/(SICI)1096-9837(199808)23:8<761::AID-ESP892>3.0.CO;2-K)
- Rogger, M., Chirico, G. B., Hausmann, H., Krainer, K., Brückl, E., Stadler, P., & Blöschl, G. (2017). Impact of mountain permafrost on flow path and runoff response in a high alpine catchment. *Water Resources Research*, 53(2), 1288–1308. <https://doi.org/10.1002/2016WR019341>
- Sass, O. (2006). Determination of the internal structure of alpine talus deposits using different geophysical methods (Lechtaler Alps, Austria). *Geomorphology*, 80(1–2), 45–58. <https://doi.org/10.1016/j.geomorph.2005.09.006>
- Schrott, L., Hufschmidt, G., Hankammer, M., Hoffmann, T., & Dikau, R. (2003). Spatial distribution of sediment storage types and quantification of valley fill deposits in an alpine basin, Reintal, Bavarian Alps, Germany. *Geomorphology*, 55(1–4), 45–63. [https://doi.org/10.1016/S0169-555X\(03\)00131-4](https://doi.org/10.1016/S0169-555X(03)00131-4)
- Smooenburg, M. (2015). *Flood behavior in alpine catchments examined and predicted from dominant runoff processes*. ETH Zürich.
- Somers, L. D., & McKenzie, J. M. (2020). A review of groundwater in high mountain environments. *WIREs Water*, December 2019, 1–27. <https://doi.org/10.1002/wat2.1475>
- Svensson, H. (1959). Is the cross-section of a glacial valley a parabola? *Journal of Glaciology*, 3, 362–363.
- Thornton, J. M. (2020). *Fully-integrated hydrological modelling in steep, snow-dominated, geologically complex Alpine terrain*. Doctoral Thesis. University of Neuchâtel.
- Wheeler, D. A. (1984). Using parabolas to describe the cross-sections of glaciated valleys. *Earth Surface Processes and Landforms*, 9(4), 391–394. <https://doi.org/10.1002/esp.3290090412>

**Table S1.** Evapotranspiration parameter values in the integrated model, rounded to two significant figures.  $d_e$  is evaporation depth,  $d_r$  root depth, LIA range gives the annual minimum and maximum Leaf Area Index (with monthly variability between these values), C1, C2, and C3 are transpiration fitting parameters, and  $H_{vp}$ ,  $H_{fc}$ ,  $H_{ol}$ , and  $H_{al}$  are the pressure heads at the wilting point, field capacity, oxic limit, and anoxic limits, respectively.  $H_{et1}$  is the pressure head below which evaporation is zero, and  $H_{et2}$  the pressure head above which full evaporation can occur.  $c_{int}$  is the canopy storage parameter. For parameters that were subjected to calibration, the initial values, lower and upper bounds permitted, and the final value obtained are specified. Evaporation from the bedrock, glaciers, unconsolidated rock, and streambed zones was deactivated in the model. All free parameters were log-transformed to improve the numerical robustness of the process.

**Table S2.** Surface parameter values in the integrated model, rounded to two significant figures.  $n_{xy}$  is the Manning's roughness coefficient,  $h_{ds}$  is the depression (or rill) storage height,  $h_o$  is the obstruction storage height,  $l_{exch}$  is the surface-subsurface coupling length. For parameters that were subjected to calibration, the initial values, lower and upper bounds permitted, and the final value obtained are specified. \*Except where permafrost, in which case  $l_{exch}$  was assigned a value of 50 m. All free parameters were log-transformed to improve the numerical robustness of the process.

**Table S3.** Subsurface parameter values in the hydrological model, rounded to an appropriate degree of precision.  $k_{xy}$  is horizontal saturated hydraulic conductivity,  $k_z$  is vertical saturated hydraulic conductivity,  $q$  is effective porosity,  $S_s$  is specific storage, and  $\alpha$  and  $\beta$  are parameters of the Van Genuchten unsaturated retention functions. These functions were simplified for all subsurface formations except soils. For parameters that were subjected to calibration, the initial values, lower and upper bounds permitted, and the final value obtained are specified. The “subsurface.mprops” file in the Supplementary Materials details the simplified unsaturated parameterization applied in non-soil zones.  $k_z = k_{xy}$ , except where indicated. All free parameters were log-transformed to improve the numerical robustness of the process.

**Movie S1.** Upper: The evolution the daily frequency forcing data prescribed to the fully-integrated model (left: all liquid water inputs, i.e. rain + snowmelt + icemelt, and right: potential evapotranspiration). Lower: actual evapotranspiration (right) and surface water depth (left) simulated using the fully integrated model with daily frequency forcing data. The period shown is the 2017/2018 hydrological year, and the time-step of the animation is half-daily. The “days” are days from 1 October 2014. Note that the  $ET_p$  and  $ET_a$  scales are inverted because HGS writes the latter as a negative flux by default.

**Movie S2.** The evolution of catchment (surface) saturation (left) and the response of water level at gauging station S2 (right) over the course of the 2017/2018 hydrological year simulated using the fully-integrated model with daily frequency forcing. The time-step of the animation is half-daily (the “days” are days from 1 October 2014).

**Movie S3.** Animation illustrating the three electrical resistivity profiles that were obtained for the Nant feature. To provide additional context to the georeferenced profiles, the surface topography according to the Alti<sup>3D</sup> digital terrain model is also represented. The bedrock interface was interpreted to be located around the transition from an upper region of lower resistivity to a lower region of higher resistivity (see the annotations on the profiles). This interface, which appears to be consistent between the profiles, was digitized (pink dots).